

Recommendations for Integrated Reservoir Management

CHPM2030 Deliverable D2.1

Version: December 2017



CHPM2030



This project has received funding from the European Union's Horizon 2020 research and innovation programme under grant agreement n° 654100.



Author contact

*János Szanyi
University of Szeged
13 Dugonics Square, H 6720 Szeged
Hungary
Email: szanyi@iif.u-szeged.hu*

Published by the CHPM2030 project, 2017

*University of Miskolc
H-3515 Miskolc-Egyetemváros
Hungary
Email: foldshe@uni-miskolc.hu*



CHPM2030 DELIVERABLE D2.1

RECOMMENDATIONS FOR INTEGRATED RESERVOIR MANAGEMENT

Summary:

In this report CHPM related practical laboratory work, computer modeling and rock measurements are described, organised and concluded. The main focus was to provide practical recommendations for integrated reservoir management based on laboratory experiments.

Authors:

János Szanyi, Máté Osvald, Tamás Medgyes, Balázs Kóbor, Tivadar M. Tóth (University of Szeged), Tamás Madarász, Andrea Kolencsinké Tóth, Ákos Debreczeni, Balázs Kovács (University of Miskolc), Balázs Vásárhelyi, Nikoletta Rozgonyi-Boissinot (Budapest University of Technology and Economics)



Table of contents

Table of contents	2
List of figures	4
List of tables	8
1. Executive summary	9
2. Introduction	10
2.1. Objectives and role of the CHPM2030 project	10
2.2. Scope and role of Task 2.1	10
3. Laboratory measurements to determine heat conductivity	12
3.1. Introducing the Thermal Conductivity Meter	12
3.2. Specification of the measurements	13
3.3. Samples	13
3.4. Results	15
3.5. Heat conductivity measurements by laser	16
3.6. Results	17
4. Stress field determination of different metallic rocks by rock mechanics	20
4.1. Rock strength measurements	20
4.2. Uniaxial compressive tests – execution and interpretation	21
4.3. Conclusions	39
5. Fracture enhancement in structures using a variety of laboratory experiments	40
5.1. Introduction	40
5.2. Experimental laser set	40
5.3. Indirect (Brazilian) tests - execution and interpretation	43
5.4. Results of andesite tests	45
5.5. Results of uniaxial compressive strength tests on andesite without laser	46
5.6. Results of the indirect tensile strength test on andesite with laser radiation	47
5.7. Results of the uniaxial compressive strength tests on andesite with laser radiation	51
5.8. Results of granite tests	60
5.9. Results of uniaxial compressive strength tests on granite with laser	60
5.10. Results of the indirect tensile strength test on granite with laser radiation	63
5.11. Conclusions	66
6. Fluid flow experiments with different levels of artificial enhancement in pressure chamber	67
6.1. Aim	67
6.2. Methodology – device built – explanation	67
6.3. Samples	68
6.4. Results	72
6.5. Discussion	75
6.6. Conclusion	75
7. Three-dimensional stochastic fracture model	76
7.1. Introduction	76
7.2. Geological background	76
7.3. Samples	78
7.4. Methods	78
7.5. Geometric parameters of fractures	79
7.6. Fracture network modelling	80
7.7. Fracture network of the underground site	82
7.8. Effect of enhancing	84
8. Three-dimensional fluid, heat- and mass-transport model to define the extractable amount of heat and metallic minerals regarding different scenarios	88
8.1. Model domain	88

8.2.	Scenarios	91
8.3.	Results of water and heat flow simulation.....	92
8.4.	Mass transport calculation	92
8.5.	Conclusions	98
9.	Conclusions.....	99
10.	References.....	100
11.	Appendices.....	104
11.1.	Summary table of SAM (Special Approximation Method) data.....	104
11.2.	Data recordings of TC measurements.....	110
11.3.	Detailed chemical composition of each fluid sample	117

List of figures

Figure 1: Schematic representation of the CHPM concept. The information presented in this report relates to the release of metals from the ‘ultra-deep orebody’ and into the recirculating geothermal fluid	11
Figure 2: Thermal Conductivity Meter TK04 with HLQ probe	12
Figure 3: A photograph of the measured samples.....	14
Figure 4: Comparison of literature data (Pethő-Vass, 2011; Egerer-Kertész, 1993) and own measurements of heat conductivity for various samples.....	16
Figure 5: Heat conductivity measurement of andesite sample	17
Figure 6: Heat conductivity measurement of granite sample	18
Figure 7: Heat conductivity measurement of sandstone sample	19
Figure 8: Stress-strain diagram of a rock showing the stages of crack development (Cai, 2010)	22
Figure 9: Appearance of the rupture for an average rigid rock.....	23
Figure 10: Uniaxial compressive strength and Young's modulus of CHPM4 sample	26
Figure 11: Uniaxial compressive strength and Young's modulus of CHPM5 sample	26
Figure 12: Uniaxial compressive strength and Young's modulus of CHPM6 sample	27
Figure 13: Uniaxial compressive strength and Young's modulus of CHPM7 sample	27
Figure 14: Uniaxial compressive strength and Young's modulus of CHPM11 sample	28
Figure 15: Uniaxial compressive strength and Young's modulus of CHPM13/a sample.....	28
Figure 16: Uniaxial compressive strength and Young's modulus of CHPM13/b sample.....	29
Figure 17: Uniaxial compressive strength and Young's modulus of CHPM14 sample	29
Figure 18: Uniaxial compressive strength and Young's modulus of CHPM18 sample	30
Figure 19: Uniaxial compressive strength and Young's modulus of CHPM22 sample	30
Figure 20: Uniaxial compressive strength and Young's modulus of CHPM36 sample	31
Figure 21: Uniaxial compressive strength and Young's modulus of CHPM38 sample	31
Figure 22: Uniaxial compressive strength and Young's modulus of CHPM41 sample	32
Figure 23: Uniaxial compressive strength and Young's modulus of CHPM44 sample	32
Figure 24: Uniaxial compressive strength and Young's modulus of CHPM45 sample	33
Figure 25: Uniaxial compressive strength and Young's modulus of CHPM47 sample	33
Figure 26: Uniaxial compressive strength and Young's modulus of CHPM48 sample	34
Figure 27: Hyperbolic failure curve and cohesion value of CHPM4 sample	35
Figure 28: Hyperbolic failure curve and cohesion value of CHPM5 sample	35
Figure 29: Hyperbolic failure curve and cohesion value of CHPM6 sample	36
Figure 30: Hyperbolic failure curve and cohesion value of CHPM11 sample	36
Figure 31: Hyperbolic failure curve and cohesion value of CHPM14 sample	37
Figure 32: Hyperbolic failure curve and cohesion value of CHPM22 sample	37

Figure 33: Hyperbolic failure curve and cohesion value of CHPM38 sample	38
Figure 34: Hyperbolic failure curve and cohesion value of CHPM45 sample	38
Figure 35: High power laser devices set by ZERLUX Ltd.....	40
Figure 36: Hypothetical stress–strain curves (Ramamurthy et al. 2017)	41
Figure 37: Relationship between modulus ratio (MR) and maximum axial strain ($\varepsilon_{a,max}$) using different carbonate rocks (Palchik, 2011)	42
Figure 38: Relationship between modulus ratio (MR) and maximum axial strain on Hungarian granitic rocks	43
Figure 39: Experimental setup before laser treatment.....	43
Figure 40: Brazilian (indirect) tensile test – before and after the failure	44
Figure 41: Experimental setup during laser treatment.....	44
Figure 42: Failure of the rock sample.....	45
Figure 43: Relationship between tensile stress and lateral strain on andesite without laser	46
Figure 44: Relationship between uniaxial compressive stress and axial strain on andesite without laser	47
Figure 45: Relationship between tensile stress and lateral strain on andesite under laser radiation	48
Figure 46: Relationship between tensile stress and time as well as lateral strain and time on andesite under laser radiation on the mantle of the sample	49
Figure 47: Relationship between tensile stress and time as well as lateral strain and time on andesite under laser radiation on the mantle of the sample	49
Figure 48: Relationship between tensile stress and time as well as lateral strain and time on andesite under laser radiation on the mantle of the sample	50
Figure 49: Relationship between tensile stress and time as well as lateral strain and time on andesite under laser radiation on the base surface of the sample	50
Figure 50: Relationship between tensile stress and time as well as lateral strain and time on andesite under laser radiation on the base surface of the sample	51
Figure 51: Experimental setup during laser treatment.....	51
Figure 52: Failure of the rock sample over time	52
Figure 53: Relationship between uniaxial compressive stress and axial strain on andesite under laser radiation on the mantle of the sample	53
Figure 54: Relationship between uniaxial compressive stress and axial strain on andesite under laser radiation on the mantle of the sample	54
Figure 55: Relationship between uniaxial compressive stress and time as well as axial strain and time on andesite under laser radiation on the mantle of the sample	54
Figure 56: Relationship between uniaxial compressive stress and time as well as axial strain and time on andesite under laser radiation on the mantle of the sample	55
Figure 57: Relationship between uniaxial compressive stress and time as well as axial strain and time on andesite under laser radiation on the mantle of the sample	55
Figure 58: Relationship between uniaxial compressive stress and time as well as axial strain and time on andesite under laser radiation on the mantle of the sample	56

Figure 59: Relationship between uniaxial compressive stress and time as well as axial strain and time on andesite under laser radiation on the mantle of the sample	56
Figure 60: Relationship between uniaxial compressive stress and time as well as axial strain and time on andesite under laser radiation on the mantle of the sample	57
Figure 61: Relationship between uniaxial compressive stress and time as well as axial strain and time on andesite under laser radiation on the mantle of the sample	57
Figure 62: Relationship between uniaxial compressive stress and time as well as axial strain and time on andesite under laser radiation on the mantle of the sample	58
Figure 63: Relationship between uniaxial compressive stress and time as well as axial strain and time on andesite under laser radiation on the mantle of the sample	58
Figure 64: Relationship between uniaxial compressive stress and time as well as axial strain and time on andesite under laser radiation on the mantle of the sample	59
Figure 65: Relationship between uniaxial compressive stress and axial strain on granite	60
Figure 66: Relationship between uniaxial compressive stress and axial strain on granite	61
Figure 67: Relationship between uniaxial compressive stress and time as well as axial strain and time on granite under laser radiation on the mantle of the sample	62
Figure 68: Relationship between uniaxial compressive stress and axial strain on granite	62
Figure 69: Relationship between uniaxial compressive stress and time as well as axial strain and time on granite under laser radiation on the mantle of the sample	63
Figure 70: Relationship between tensile stress and lateral strain on granite under laser radiation.....	64
Figure 71: Relationship between tensile stress and time as well as lateral strain and time on granite under laser radiation on the base surface of the sample	64
Figure 72: Relationship between tensile stress and time as well as lateral strain and time on granite under laser radiation on the base surface of the sample	65
Figure 73: Relationship between tensile stress and time as well as lateral strain and time on granite under laser radiation on the base surface of the sample	65
Figure 74: The experimental setup for flow-through leaching tests.....	67
Figure 75: Cross-section of CTO8001 drilling, on the figure blue arrow heads mark the original location of the samples which were used in the laboratory (Courtesy of LNEG)	69
Figure 76: Chemical composition (ICP-MS) of samples CHPM3.1 and CHPM4.1	72
Figure 77: Chemical composition (ICP-MS) of samples CHPM4.2 and CHPM4.4	73
Figure 78: Chemical composition (ICP-MS) of samples CHPM5.1 and CHPM6.1	73
Figure 79: Chemical composition (ICP-MS) of samples CHPM12.1 and CHPM14.1.....	73
Figure 80: Chemical composition (ICP-MS) of samples CHPM29.1 and CHPM32.1.....	74
Figure 81: Chemical composition (ICP-MS) of samples CHPM39.1 and CHPM40.1.....	74
Figure 82: Chemical composition (ICP-MS) of samples CHPM42.1 and CHPM43.1.....	74
Figure 83: XRD diagram of CHPM3 sample	75

Figure 84: Simplified geological map of the study area (after Balla, 2004). Pink: monzogranite-dominated realm, green: monzonite-dominated realm. Bold lines denote proven major shear zones. Inset: sketch map of the underground site	77
Figure 85: Alternative fracture network models simulated for the underground site. Figures show results of different runs. Colours denote interconnected subsystems. a) Total fracture network of a selected run. b) Communicating subsystems of the same run. c-f) Communicating subsystems resulting from different runs.....	83
Figure 86: Horizontal sections of fracture network models from $E = -1.64$ up to -1.14	85
Figure 87: Change of the size of the largest connected fracture system when increasing E between -1.64 and -1.14 . For each case 5 independent models were computed.....	86
Figure 88: Calculated effective fracture porosities. (Range shows $\pm 1\sigma$).....	86
Figure 89: Calculated permeabilities when increasing E from -1.64 up to -1.14 . Data are given as the average of the diagonal of the intrinsic permeability tensor (16 independent calculations).....	87
Figure 90: Hull of model domain.....	89
Figure 91: Target layer of EGS with elevation isolines (flag symbolises the centre of enhanced zone).....	89
Figure 92: Distribution of porosity along the SW-NE section in different layers	91
Figure 93: Location of planned EGS system's wells (Distance between the wells is 605 m along mesh edges; blue flag: production well, red flag: injection well)	93
Figure 94: Modelled steady state temperature distribution ($^{\circ}\text{C}$) in a cross section after 200000 years model run	93
Figure 95: Hydraulic head (m) after 100 years operation (yield is $3500 \text{ m}^3/\text{day}$) in case of enhanced granite (the initial head was around 80 m)	94
Figure 96: Hydraulic head (m) after 100 years operation (yield is $300 \text{ m}^3/\text{day}$) in case of intact granite (the initial head was around 80 m)	94
Figure 97: Modelled temperature-time graph in production well ($3500 \text{ m}^3/\text{day}$) during 100 years operation in case of enhanced granite	95
Figure 98: Modelled temperature-time graph in production well ($300 \text{ m}^3/\text{day}$) during 100 years operation in case of intact granite.....	95
Figure 99: Temperature distribution after 5 years injection in case of enhanced granite	96
Figure 100: Temperature distribution after 20 years injection in case of enhanced granite	96
Figure 101: Temperature distribution after 50 years injection in case of enhanced granite	97
Figure 102: Temperature distribution after 70 years injection in case of enhanced granite	97
Figure 103: Temperature distribution after 100 years injection in case of enhanced granite	98

List of tables

Table 1: Fixed parameters for thermal conductivity measurements.....	13
Table 2: Summarizing table of heat conductivity measurement samples.....	13
Table 3: Summarizing table of the results in heat conductivity measurements.....	15
Table 4: Data for calculating the heat conductivity of andesite sample	17
Table 5: Data for calculating the heat conductivity of granite sample	18
Table 6: Data for calculating the heat conductivity of sandstone sample	19
Table 7: Summarizing table of heat conductivity measurements by laser	19
Table 8: Results of rock stress measurements.....	24
Table 9: Results of the indirect tensile strength tests on andesite without laser	45
Table 10: Results of uniaxial compressive strength tests on andesite without laser	46
Table 11: Results of the indirect tensile strength test on andesite with laser	48
Table 12: Results of the uniaxial compressive strength test on andesite with laser	53
Table 13: Results of uniaxial compressive strength tests on granite without laser	60
Table 14: Results of uniaxial compressive strength tests on granite under laser radiation.....	61
Table 15: Results of indirect tensile strength tests on granite under laser radiation.....	63
Table 16: Samples investigated in leaching measurements.....	68
Table 17: A summarizing table of circumstances during each measurement.....	70
Table 18: Abbreviations used in fracture network modelling.....	78
Table 19: Characteristic data of the model	90
Table 20: Hydrodynamic parameters in the model domain	90
Table 21: Heat transport parameters in the model domain.....	90
Table 22: Hydraulic parameters of enhanced granitic layers.....	92

1. Executive summary

In the provisioned CHPM technology an enhanced geothermal system would be established on a deep metal-bearing geological formation, which would be conducted in a way that the co-production of energy and metals could be possible.

In the present study heat conductivity measurements were carried out on rocks with high potentiality to form a basis of an orebody-EGS system. The same samples were investigated in a pressure chamber to determine which metals and minerals can be mobilized in such a system and at what fluid flow levels. Results from stress field determination of various metallic rocks by rock mechanics and fracture enhancement were used to build 3-dimensional stochastic fracture, fluid flow, heat and mass transport models. These models aimed to define the extractable amount of heat and metallic minerals in different scenarios. During these investigations, a novel laser-technology was introduced and thoroughly tested to enhance permeability and fractures in rocks of interest on a laboratory scale.

Rock mechanical studies point at granitoid formations as the prime candidate to host an enhanced communicating fracture network. Mineralisations from granitoid rocks were put to high pressure and high temperature tests and results indicate enhanced release in Pb, Zn and Li. 3D stochastic fracture network modelling (RepSim) and finite element flow and transport modelling (FeFlow) determined that fluid production at 3.500 m³/day (40 l/s) is a sustainable possibility. Projecting these parameters to a pilot site metal production may reach magnitudes in the order of kg/day.

Our studies indicate that the proposed orebody-EGS system may be a feasible solution to the coproduction of electricity, heat and metal on granite based reservoirs. The conclusions presented in this report are based on laboratory measurements and numerical simulations; upscaling them to pilot plant proportions will be informed by data obtained from WP5.

2. Introduction

2.1. Objectives and role of the CHPM2030 project

The strategic objective of the CHPM2030 project is to develop a novel technological solution (Combined Heat, Power and Metal extraction from ultra-deep ore bodies), which will help increase the attractiveness of renewable geothermal energy and reducing Europe's dependency on the import of metals and fossil fuels¹.

In the envisioned technology, an Enhanced Geothermal System (EGS) is established within a metal-bearing geological formation at depths of 4 km or more (Figure 1), which will be manipulated in a way that the co-production of energy and metals will be possible. The project, at a laboratory scale, intends to prove the concept that the composition and structure of ore bodies have certain characteristics that could be used as an advantage when developing an EGS.

CHPM2030 is organised into several Work Packages, and the results presented in this report fall within Work Package 2. The overall objective of this Work Package is to understand the natural networks of hydraulically-conductive mineral veins that could function as heat-exchange surfaces, and sources of metals. Specific objectives are to: i) develop the tools and methods for orebody EGS reservoir management, and ii) test and validate the methods using simulations and laboratory experiments reaching and exceeding TRL-4.

To achieve these objectives, we will test three hypotheses in this Work Package:

- 1 That the composition and structure of orebodies have certain advantages that could be used to our advantage when developing an EGS.
- 2 Metals can be leached from the orebodies in high concentrations over a prolonged period and may substantially influence the economics of EGS.
- 3 That continuous leaching of metals will increase system performance over time in a controlled way and without having to use high-pressure reservoir stimulation, minimizing potential detrimental impacts of both heat and metal extraction.

Many of the technical activities within Work Package 2 are related to laboratory-scale testing and measurement, and these are implemented through several inter-related Tasks, each with a specific deliverable:

Task 2.1: Concepts and simulations for integrated reservoir management.

Task 2.2: Metal content mobilization using mild leaching.

Task 2.3: Metal content mobilization with nanoparticles.

Task 2.4: Overall systems dynamics and data for environmental assessment.

2.2. Scope and role of Task 2.1

Task 2.1 provides an overall framework for the implementation of the Work Package. The foreseen tasks are similar to implementing research investigations for a petrothermal EGS but with the additional challenge of metal mobilisation and transport. The concepts developed for orebody manipulation were

¹ <http://www.chpm2030.eu/introduction/>

tested and implemented in a modelling environment, using simulations that were built up using a combination of samples from the case study areas (WP1), literature, laboratory measurements and auxiliary data that is available from conducted measurements and previous studies. Recent experience gained with the geo-engineering of shale oil and gas reservoirs, as well as CO₂ storage were considered and evaluated during the execution of the work.

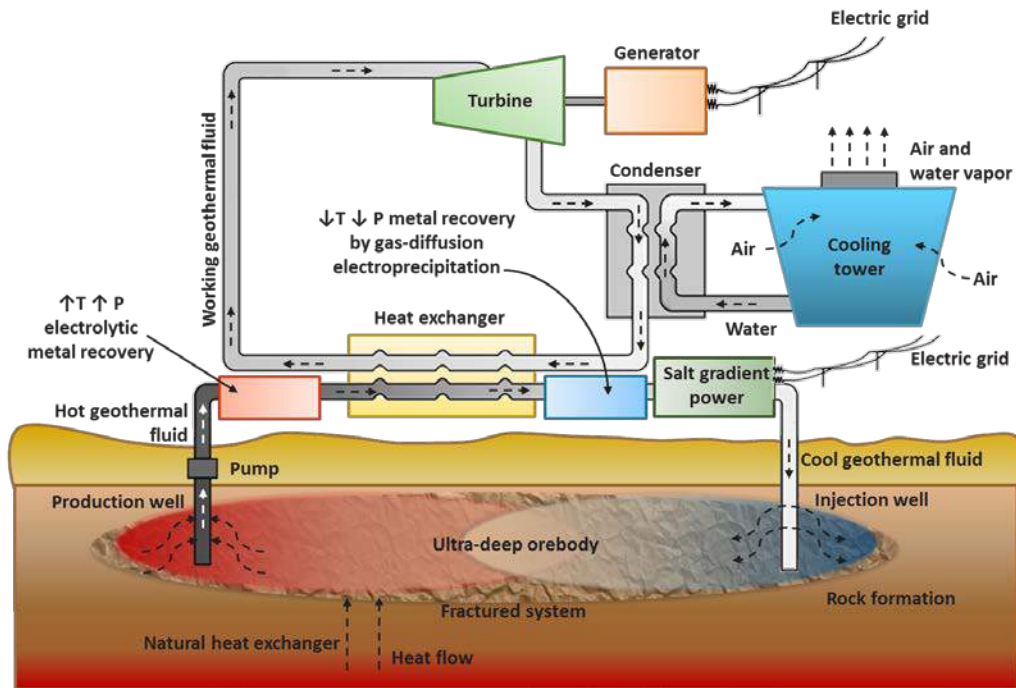


Figure 1: Schematic representation of the CHPM concept. The information presented in this report relates to the release of metals from the 'ultra-deep orebody' and into the recirculating geothermal fluid

3. Laboratory measurements to determine heat conductivity

3.1. Introducing the Thermal Conductivity Meter

TK04 determines thermal conductivity based on the transient heat flow method (needle probe method) according to ASTM D5334-08 (ASTM Standard D5334-08, "Standard Test Method for Determination of Thermal Conductivity of Soil and Soft Rock by Thermal Needle Probe Procedure"). A line source is heated with constant power, and source temperature is recorded simultaneously. Thermal conductivity is calculated from the resulting heating curve (i.e. the rise of temperature vs. time). The method yields absolute thermal conductivity values and does not require reference or calibration measurements.

TK04 (on Figure 2) can measure the thermal conductivity of solids or solid fragments (including sediment, rock, drill cores or drill cuttings from boreholes), pastes, powders and viscous liquids in a measuring range of 0.1 to 10 W m⁻¹K⁻¹ and a temperature range of -25 to 125°C.



Figure 2: Thermal Conductivity Meter TK04 with HLQ probe

A standard size needle probe for laboratory use (Standard VLQ) and a large and particularly robust needle probe for field measurements, (Field VLQ) are available. For hard or brittle sample materials which are difficult to prepare for inserting a needle probe in, TK04 uses a modified line-source method for plane surfaces. The needle is embedded in the underside of a cylinder-shaped probe body (HLQ probe) which is placed on top of the sample surface. No drilling is required. In addition to the Standard HLQ probe for laboratory use a Mini HLQ for small samples is available.

TK04 is fully software-controlled by a connected computer or notebook. The TK04 software runs complete measuring series unattended and evaluates the data, results are saved directly to the computer's hard disk and can be analyzed in detail and printed after the measuring series is completed.

As thermal conductivity tests are sensitive to factors such as the contact between probe and sample, sample size, heating power, convection (for moist samples) or temperature changes, the software automatically monitors and corrects the temperature drift of the sample and provides tools for detecting sample preparation problems and instable measuring conditions.

The TK04 software combines measuring and evaluation under a single graphical user interface. The software connects directly to the graphical presentation and analysis software TkGraph for creating result diagrams and checking the data for influences of sample preparation, measuring conditions and external disturbances.

3.2. Specification of the measurements

There are some parameters which can be chosen by the user before the thermal conductivity measurements. These parameters are summarized in Table 1. The values are chosen based on the size, type and expected conductivity of the rock samples.

Table 1: Fixed parameters for thermal conductivity measurements

Type of probe	HLQ probe
Heating power	3 W/m
Total measuring time	80 s
Drift control*	10

*The drift control parameter modifies the criterion used to decide if the temperature drift of the sample is sufficiently small or sufficiently predictable to start measuring, 10 is the default value.

Heating power and drift control is adjusted automatically during the measurement to achieve the highest accuracy. When the measurement starts the line, source is heated for the chosen measuring time and the source temperature is recorded simultaneously in time. After finishing a single measurement, the drift-corrected temperature-time data are saved. The heating curve then is evaluated using an algorithm. The algorithm analyzes the heating curve in up to several thousand different time intervals. From each interval rated suitable for thermal conductivity determination a thermal conductivity value is calculated, then the software automatically chooses the solution best matching the theory as the result of the measurement.

3.3. Samples

Measurements are reported from samples collected at 14 sites in the Tokaj mountain of North-Eastern Hungary. This mountain is built almost exclusively of Tertiary volcanics. The rock types, sampling sites, and samples' ID are summarized in Table 2 and shown on Figure 3. CHPM2020 project consortium was aware of the limitations of samples from the project targeted depth. In order to keep up the proper pace of lab activities we involved near surface volcanic samples to test and apply the proper methodology.

Table 2: Summarizing table of heat conductivity measurement samples

Sample ID	Sampling site	Rock type
T1	Bodrogkisfalud	rhyolite ash-flow tuff
T2	Sátoraljaújhely	pyroxene amphibole dacite
T3	Sátoraljaújhely	welded rhyolite tuff
T4	Kishuta	rhyodacite
T5	Kishuta	red rhyolite

Sample ID	Sampling site	Rock type
T6	Kishuta	pyroxene andesite
T7	Kishuta	pumiceous rhyolite
T8	Kishuta	rhyolite
T9	Bózsza-Pálháza	derived rhyolite tuff
T10	Gönc	pyroxene dacite
T11	Gönc	clay tuffite
T12	Vizsoly	rhyolite avalanche tuff
T13	Boldogkőváralja	allothigenetic rhyolite tuff
T14	Boldogkőváralja-Arka	acidic pyroxene-andesite



Figure 3: A photograph of the measured samples

Samples are cut for 80x15 mm size. Because of the roof surface of the samples contact fluid was used. Contact fluid improves the contact between sample and probe and hence the quality of results considerably. For the measurements, the contact fluid (Wacker P12 paste, TC: $0.81 \text{ Wm}^{-1}\text{K}^{-1}$) is applied to the underside of the probe where the line source is located. Measurements were performed at a constant 22-25 °C room temperature.

3.4. Results

Table 3 gives a summary of the measurement results. The measurements can be considered coherent for the single rock types, the maximum variation during the measurements was less than 3%, the average value was less than 2%. During measurement special attention was given to provide constant circumstances, eliminating noise, vibration and static ambient temperature. The measurements were compared to Hungarian literature data (Pethő-Vass, 2011; Egerer-Kertész, 1993) from a wide range of measurements, while our samples were originated from one region of Hungary.

Our andesite measurements show a much narrower range of heat conductivity than that of the literature data (Figure 4). It is probably due to the fact that our samples were pyroxene type propylites. Dacite measurements are mostly in the range of literature data, the outlier data are the results of rhyodacite measurements. The measurements on rhyolite significantly differ from literature data, and there is only partial overlap between measured and literature heat conductivity data for various tuffs. Detailed measurement data can be found in appendix 11.1 and figures in appendix 11.2.

Table 3: Summarizing table of the results in heat conductivity measurements

Sample ID	Rock type	Average thermal conductivity (W/mK)	Variation (%)	Number of measurement	max. number of heating cycle
T1	rhyolite ash-flow tuff	0.81	± 1.3 ; ± 1.5	2	15
T2	pyroxene amphibole dacite	1.87	± 1.5	1	10
T3	welded rhyolite tuff	0.77	± 2.5	1	8
T4	rhyodacite	0.77	± 2.7	1	6
T5	red rhyolite	1.10	± 1.4 ; ± 2.2	2	10
T6	pyroxene andesite	1.68	± 1.5 ; ± 2	2	10
T7	pumiceous rhyolite	0.79	± 1.8 ; ± 2.5	2	9
T8	rhyolite	1.65	± 1.4	1	9
T9	derived rhyolite tuff	0.4	± 2.3 ; ± 1.9	2	7
T10	pyroxene dacite	1.47	± 1.7	1	10
T11	clay tuffite	1.56	± 1.9	1	10
T12	rhyolite avalanche tuff	0.26	± 2.8	1	5
T13	allothigenetic rhyolite tuff	0.37	± 1.2	1	3
T14	acidic pyroxene-andesite	1.73	± 1.9	1	10

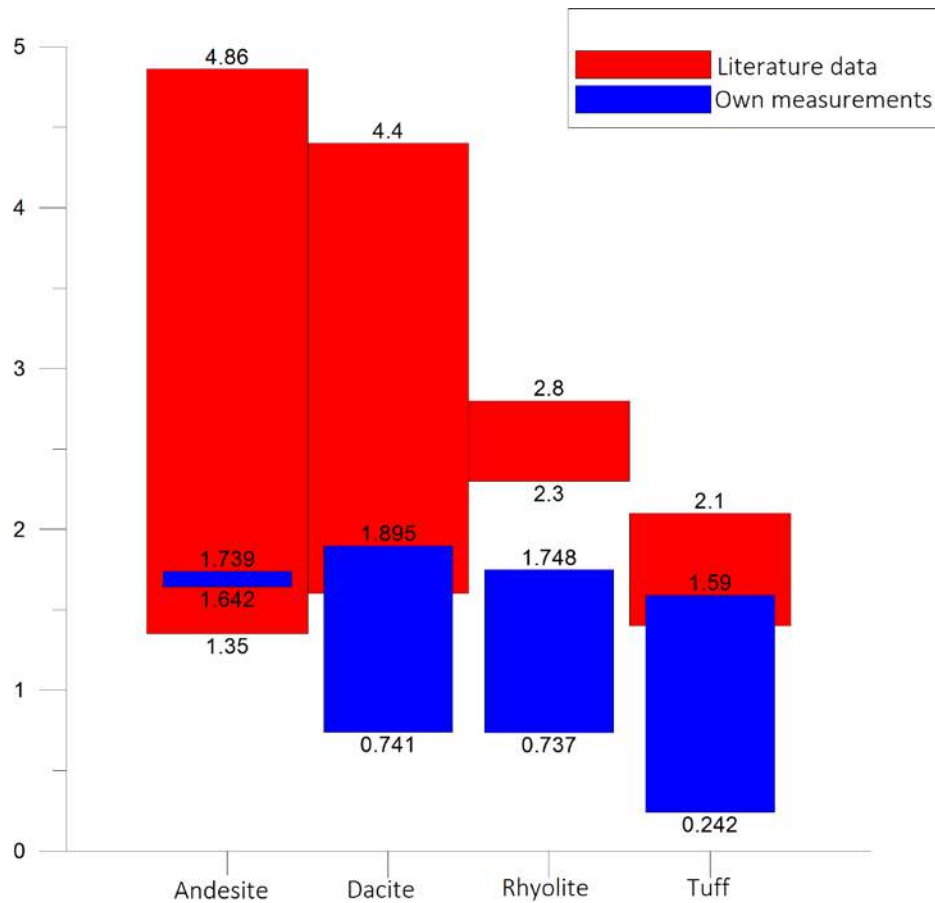


Figure 4: Comparison of literature data (Pethő-Vass, 2011; Egerer-Kertész, 1993) and own measurements of heat conductivity for various samples

3.5. Heat conductivity measurements by laser

Complementary investigations were made with a laser based heat conductivity meter. The device uses small performance (5 W) laser and a thermometer. Rock samples (andesite, granite and sandstone) were prepared for measurement such as inserting previously calibrated sensors which registers value in every 0.5 sec. These rock samples were different from the previous ones, because these samples were prepared for laser treatment. Registered values were calculated to °C with calibration. The calculated and corrected temperature values were plotted on a graph and to the given linear case a Fourier equation was fitted. These parameters are suitable to calculate the linear specific heat capacity (α) in m^2/s . With the following equation the heat capacity and heat density can be calculated:

$$\alpha \left[\frac{m^2}{sec} \right] = \frac{\lambda \left[\frac{W}{m \cdot K} \right]}{\rho \left[\frac{kg}{m^3} \right] \cdot c \left[\frac{J}{kg \cdot K} \right]} \text{ and } \lambda \left[\frac{W}{m \cdot K} \right] = \alpha \left[\frac{m^2}{sec} \right] \cdot \left(\rho \left[\frac{kg}{m^3} \right] \cdot c \left[\frac{J}{kg \cdot K} \right] \right)$$

Other equations used in calculations:

$$T = T1 \cdot \left\{ 1 - \operatorname{erf} \left[\frac{l}{\sqrt{\alpha \cdot t}} \right] \right\} + T0,$$

where T0 is starting temperature (°C),

T1 is temperature difference (°C),

l is distance (m),
and t is time (s).

3.6. Results

The results of each measurement are shown below. Measurement for andesite sample can be seen on Figure 5 and data in Table 4. During andesite sample measurement χ^2 was 0.12042 and R^2 was 0.99338 (χ^2 :chi-squared test; R^2 :correlation coefficient).

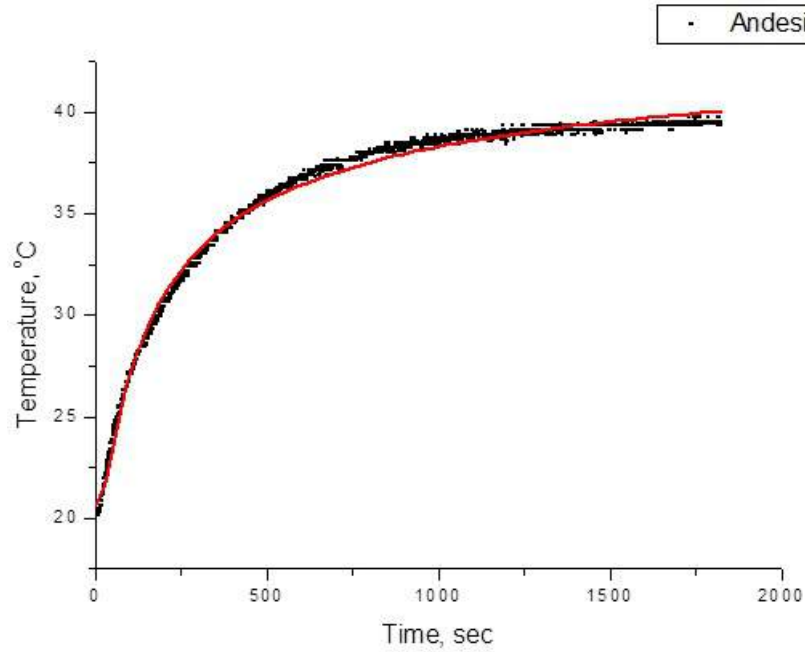


Figure 5: Heat conductivity measurement of andesite sample

Table 4: Data for calculating the heat conductivity of andesite sample

Parameter	Value	Error
T0	20.65752	0.04208
T1	24.51524	0.03885
l	0.01	0
α	1.5458E-6	9.7087E-9

(Zero error means, the parameter is measured, not calculated!)

Measurement for granite sample can be seen on Figure 6 and data in Table 5. During granite sample measurement χ^2 was 0.20337 and R^2 was 0.98769.

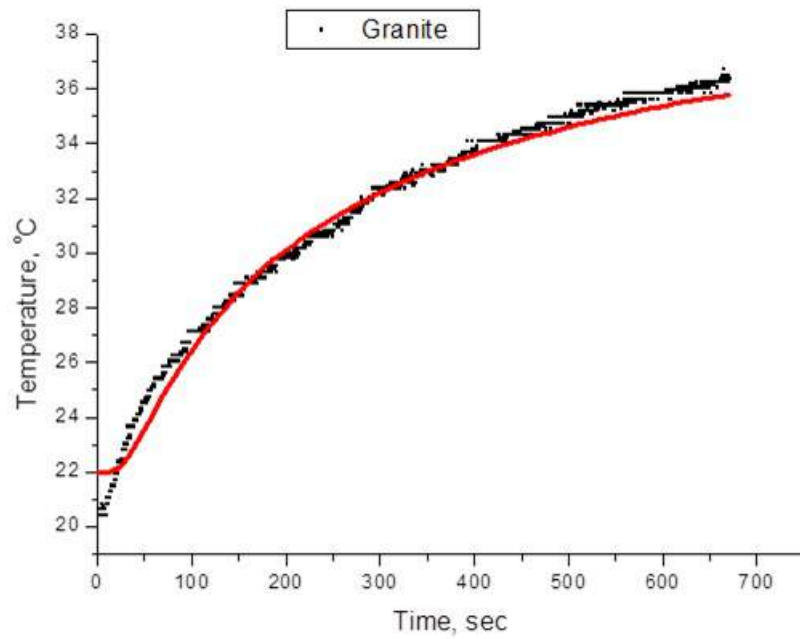


Figure 6: Heat conductivity measurement of granite sample

Table 5: Data for calculating the heat conductivity of granite sample

Parameter	Value	Error
T0	22.00747	0.05247
T1	22.23865	0.07478
l	0.01	0
α	1.217E-6	1.5073E-8

(Zero error means, the parameter is measured, not calculated!)

Measurement for sandstone sample can be seen on Figure 7 and data in Table 6. During sandstone sample measurement χ^2 was 0.1553 R^2 was 0.9905.

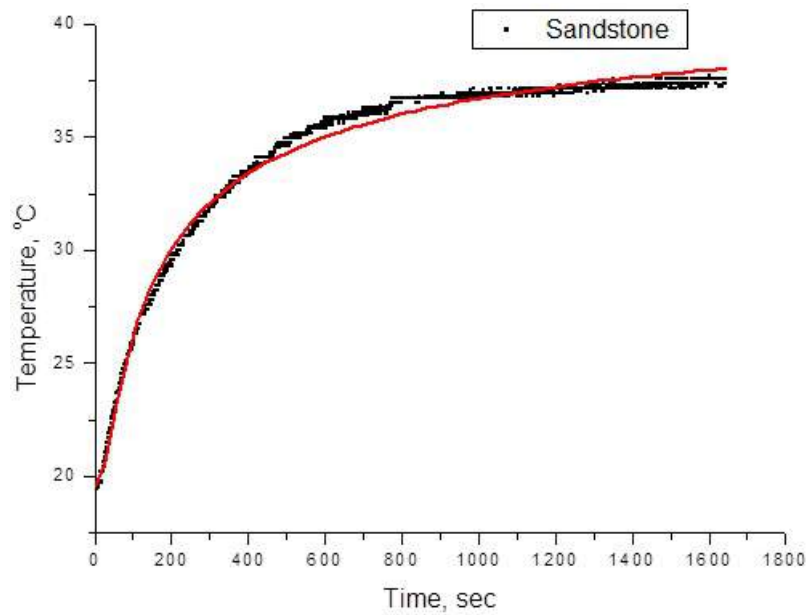


Figure 7: Heat conductivity measurement of sandstone sample

Table 6: Data for calculating the heat conductivity of sandstone sample

Parameter	Value	Error
T0	19.58023	0.05087
T1	23.27896	0.04695
l	0.01	0
α	1.7539E-6	1.3959E-8

(Zero error means, the parameter is measured, not calculated!)

From the measured data with the aforementioned equations the heat conductivity can be calculated for each sample. Table 7 describes the results for each measurement.

Table 7: Summarizing table of heat conductivity measurements by laser

Rock type	Heat conductivity $\left[\frac{W}{m \cdot K}\right]$
Andesite	3,36
Granite	2,81
Sandstone	3,6

4. Stress field determination of different metallic rocks by rock mechanics

4.1. Rock strength measurements

Studying mechanical properties of the rocks require sophisticated tests. Usual behaviour models of materials describe not only properties but mechanical condition of the material as well. Thus, idealized models of materials should be selected and adjusted to the characteristics of the rock and its properties must be determined by measurements to obtain accurate results. Mathematical and computational methods can provide acceptable results if the properties used for the model describe the behaviour of the rock mass properly.

In situ characteristics of the rock must be taken into consideration, consequently, measurements should be done on site if possible. As in situ results are available to a limited extent only, many times laboratory tests of rock samples are required. These are obtained in labs and are converted into the characteristics of the rock mass itself according to experiences and theoretical considerations and using conversion factors based on the comparison of in situ and laboratory test results.

It is a well-known fact that none of the linear failure curves may be applied in the whole range of stresses (compressive and tensile stresses). In the range of tensile stresses and small compressive stresses, failure may better be described with parabolic curves, but such curves yield no good approximation in the case of large compressive stresses. In this range, the correlation between normal and shear stresses is more linear. All this led to the idea that it is suitable to apply a hyperbolic failure curve across the whole range of stresses.

The main advantage of the process proposed is that every element is supported by measurement results. Uniaxial compressive and tensile strength as well as conventional triaxial compressive strength at different confining pressure should be measured to obtain accurate results. The values of the measurement results obtained in this way are plotted on the σ - τ plane (Mohr plane). Then, according to the usual principles of function approximation, the hyperbolic failure curve, best accommodated to measurement results, is determined.

We carried out the following measurements:

Uniaxial compressive strength – Suggested methods for Determining the Uniaxial Compressive Strength and Deformability of Rock Materials, *International Journal of Rock Mechanics and Mining Sciences & Geomechanics Abstracts*, Vol. 16, No. 2, pp.135-140.

Triaxial compressive strength – *Suggested Methods for Determining the Strength of Rock Materials in Triaxial Compression: Revised Version*, *International Journal of Rock Mechanics and Mining Sciences & Geomechanics Abstracts*, Vol. 20, No. 6, pp.285-290.

Indirect tensile strength by Brazil test – *Suggested Methods for Determining Tensile Strength of Rock Materials*, *International Journal of Rock Mechanics and Mining Sciences & Geomechanics Abstracts*, Vol. 15, No. 3, pp.99-103.

4.2. Uniaxial compressive tests – execution and interpretation

The most common approach to study the mechanical properties of rocks is by using an unconfined compressive test. If the lateral surface of the rock is traction-free, the configuration is referred to as uniaxial compression ($\sigma_1 > 0$, $\sigma_2 = \sigma_3 = 0$). Using this configuration, the uniaxial strain (ϵ) depends upon uniaxial stress (σ) and can be measured. If σ is plotted against ϵ given the stress-strain curve, the point at which it reaches the maximum stress value is the uniaxial compressive strength (σ_c) [MPa] and this point marks the transition from ductile to brittle behavior. From the slope of a stress-strain curve at 50 % of the ultimate stress, Young's modulus (elasticity modulus (E) [GPa]) can be experimentally determined; the elastic modulus is calculated at 50 % of the ultimate strength, according to the ISRM (2006).

This material property describes well the rigidity of the samples. The Poisson's ratio value (ν) is the ratio of the axial and lateral strains. Most rocks have Poisson's ratio values ranging between 0.2 and 0.4. A perfectly incompressible material deforms elastically at small strains and would have a Poisson's ratio of exactly 0.5.

Due to the differences of the rock samples and the uncertainty of the measuring methods, this material constant could be not determined with absolute certainty. Destruction work (or strain energy— W_d) can be calculated from the measured stress-strain curves. This equals the area under the measured curve and the energy necessary to break the rock.

Several characterizing stress levels can be determined through laboratory tests that are substantial in understanding the failure (damage) process of brittle rocks during compression. The complete axial stress–strain relations by Cai (2010) and Martin (1993) illustrated on Figure 8. The symbols are the following:

- σ_{cc} is the crack closure stress level,
- σ_{ci} is the crack initiation stress level,
- σ_{cd} is called the crack propagation stress level. This latter parameter is close to the long-term strength of the rock.

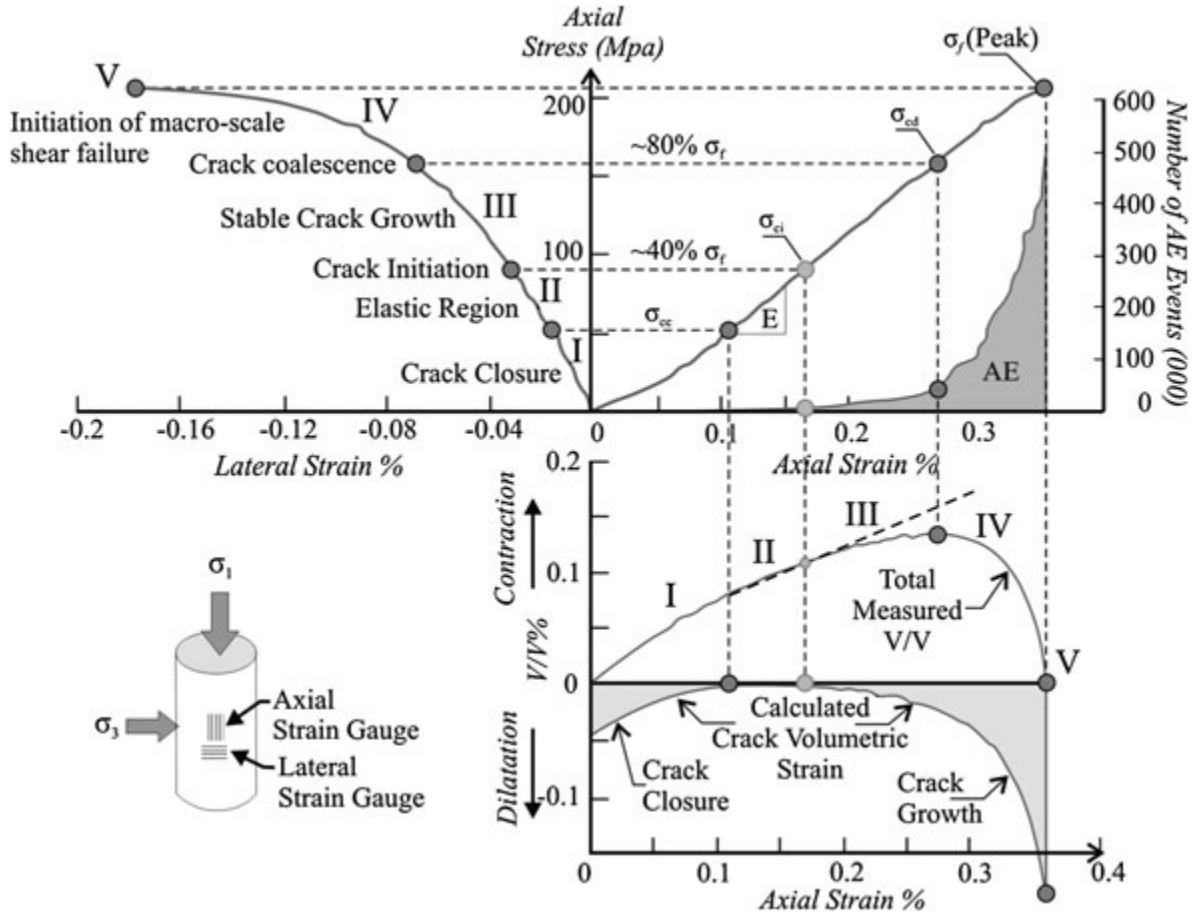


Figure 8: Stress-strain diagram of a rock showing the stages of crack development (Cai, 2010)

The crack initiation stress (σ_{ci}) can be identified on intact rocks during laboratory tests by the onset of stable crack growth or dilatency. This can be defined from the stress–volumetric strain curve as the point of the departure of the volumetric strain observed at a given mean stress from that observed in uniform loading to the corresponding pressure (Bieniawski, 1967). In the case of a uniaxial (or triaxial) test, the volumetric strain ε_v is defined by:

$$\varepsilon_v = \varepsilon_a + 2\varepsilon_l \quad (1)$$

where: ε_a and ε_l are the axial and lateral strains, respectively. The crack volumetric strain ε_{cv} is defined by Martin (1993), so that:

$$\varepsilon_{cv} = \varepsilon_v + \frac{1 - 2\nu}{E} \sigma_a \quad (2)$$

where σ_a is the axial stress, E is the Young's modulus, and ν is Poisson's ratio. As Figure 8 illustrates, both the volumetric strain and the crack volumetric strain plots can be used to determine the crack initiation stress level (σ_{ci}). This parameter can also be identified as the point where the volumetric strain starts to differ from the straight line of the elastic deformation stage (stage II), or the crack volumetric strain deviates from zero, as shown in Figure 8.

Microscopic observations indicate that newly generated cracks are tensile in nature, generated by extension train, and mostly aligned in the same direction as the maximum compressive stress. After crack initiation, the propagation of the microcracks is a stable process, which means that the cracks only extend by limited amounts in response to given increments in stress.

During this research, unconfined compressive tests were carried out, ie. $\sigma_3 = 0$. In Figure 9 an average failure appearance is shown in case of rigid rocks.

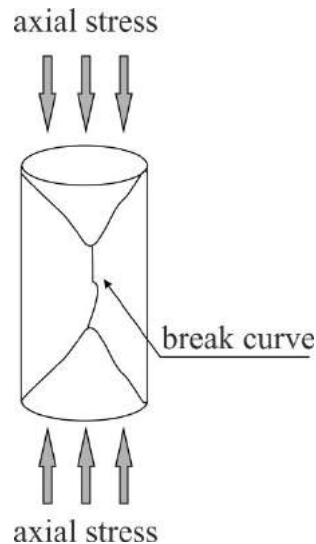


Figure 9: Appearance of the rupture for an average rigid rock

For the measurement of strength and elastic properties of rock samples the equipment's of the Mining Engineering Department of the University of Miskolc were used:

- Hydraulic test loading machine up to 1000 kN loads
- Triaxial cell and hydraulic unit up to 300 bar confining pressure
- Cells for measuring load and displacement and QUANTUM-X data acquisition system produced by HBM (Hottinger Baldwin Messtechnik GmbH)
- CATMAN software for data processing

Uniaxial compressive strength and Young's modulus measurements are presented on Figure 10-26 of CHPM samples. Hyperbolic failure curve and cohesion measurement results are shown on Figure 27-34 of CHPM samples. All the results are summarized in Table 8 below.

Table 8: Results of rock stress measurements

Sample	Uniaxial compressive strength [MPa]	Tensile strength (Brasil) [MPa]	Triaxial compressive strength [MPa] confining pressure 300 bar	Young's modulus [GPa]	Hyperbolic failure curve	Angle of internal friction [°]	Cohesion (about of failure curve) [MPa]
4	22,6	3,84	112,7	4,6	yes	30,0	6,4
5	84,4	12,5	312,3	5,7	yes	50,1	21,9
6	85,5	7,7	368,1	8,1	yes	53,9	18,2
7	80,4	17,2	75,5	6,2	discrepancy	discrepancy	31,1
11	34,1	8,7	311,2	5,8	yes	53,6	19,7
13/a (white)	30,4	6,1	lack of triaxial test	9,4	lack of triaxial test	lack of triaxial test	10,8
13/b (gray)	43,2	12,2	lack of triaxial test	8,7	lack of triaxial test	lack of triaxial test	discrepancy
14	199,4	16,3	394,0	12,9	yes	47,1	36
18	82,8	12,6	lack of triaxial test	9,5	lack of triaxial test	lack of triaxial test	21,9
22	70,2	12,9	145,8	8,2	yes	25,6	20,5
36	67,3	8,2	lack of triaxial test	14,2	lack of triaxial test	lack of triaxial test	14,7
38	122,3	11,8	269,3	26,0	yes	41,4	35,1
41	69,3	22,6	lack of triaxial test	25,4	lack of triaxial test	lack of triaxial test	discrepancy

42	lack of uniaxial test	10,2	lack of triaxial test	lack of uniaxial test	lack of triaxial test	lack of triaxial test	lack of uniaxial test
44	96,2	8,4	lack of triaxial test	21,3	lack of triaxial test	lack of triaxial test	16,5
45	165,0	16,5	283,2	33,2	yes	36,5	24,6
47	101,4	7,2	lack of triaxial test	29,5	lack of triaxial test	lack of triaxial test	15,2
48	54,9	14,1	lack of triaxial test	19,3	lack of triaxial test	lack of triaxial test	discrepancy
49	lack of uniaxial test	18,7	lack of triaxial test	lack of uniaxial test	lack of triaxial test	lack of triaxial test	lack of uniaxial test

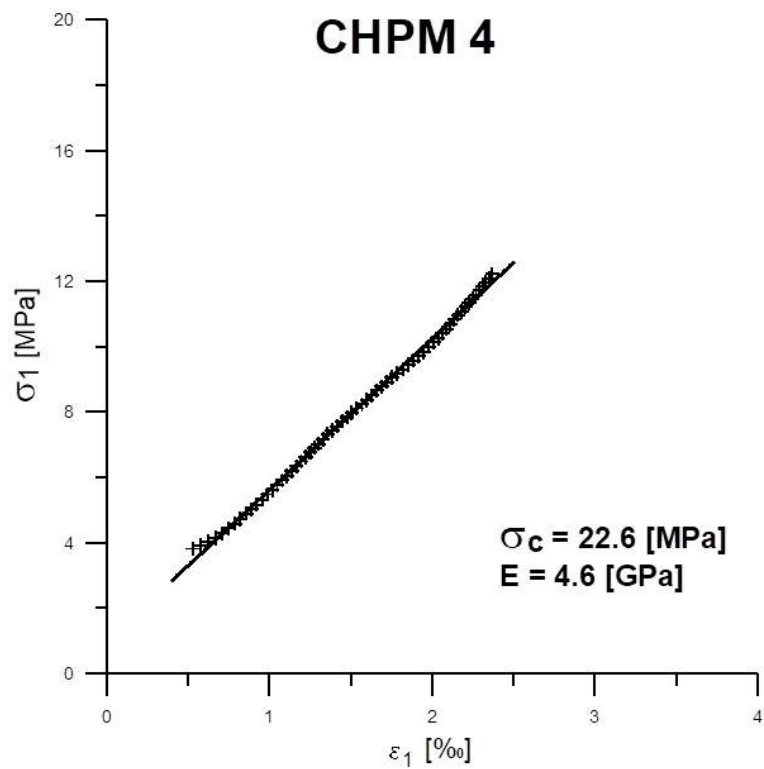


Figure 10: Uniaxial compressive strength and Young's modulus of CHPM4 sample

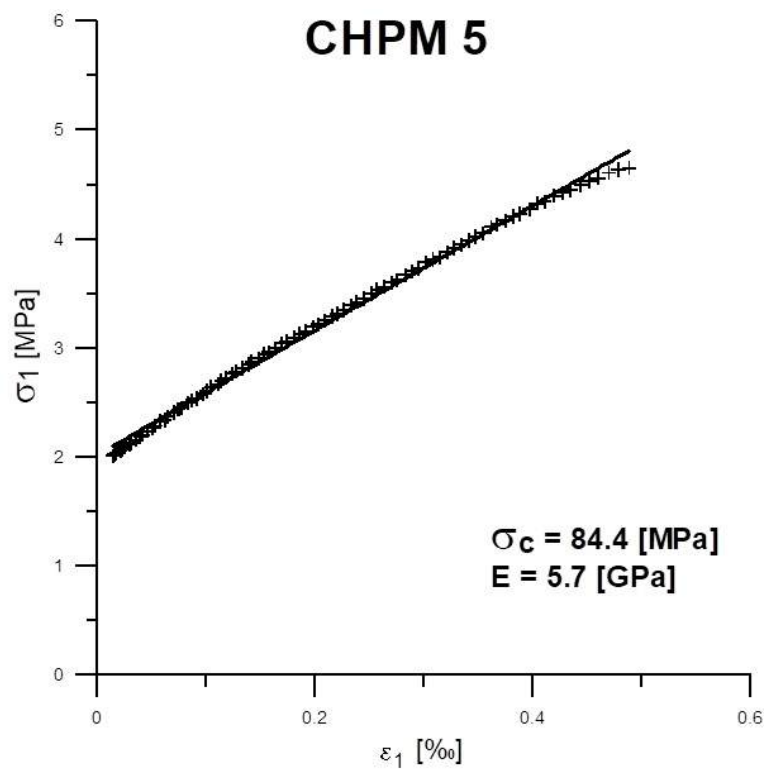


Figure 11: Uniaxial compressive strength and Young's modulus of CHPM5 sample

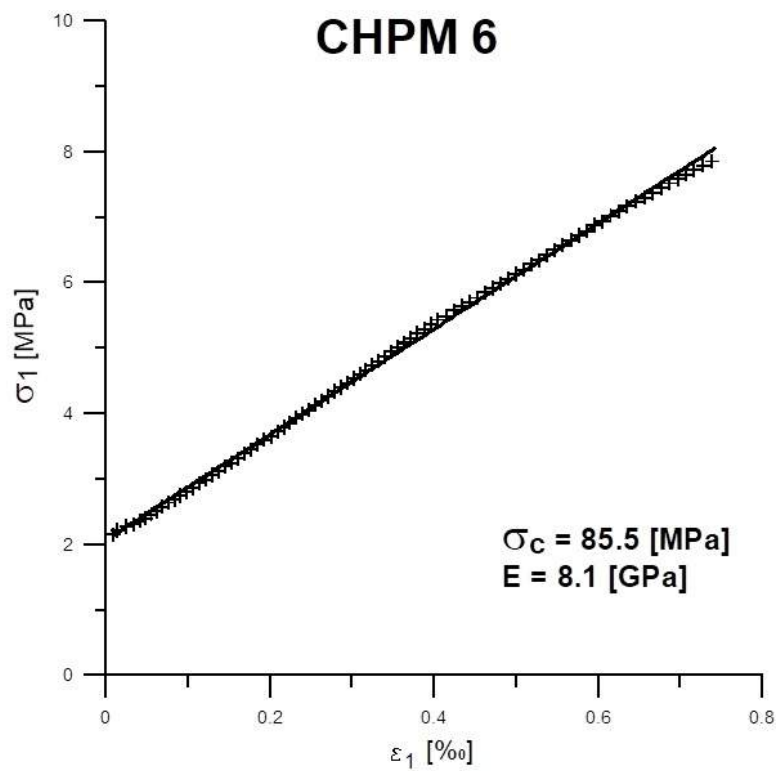


Figure 12: Uniaxial compressive strength and Young's modulus of CHPM6 sample

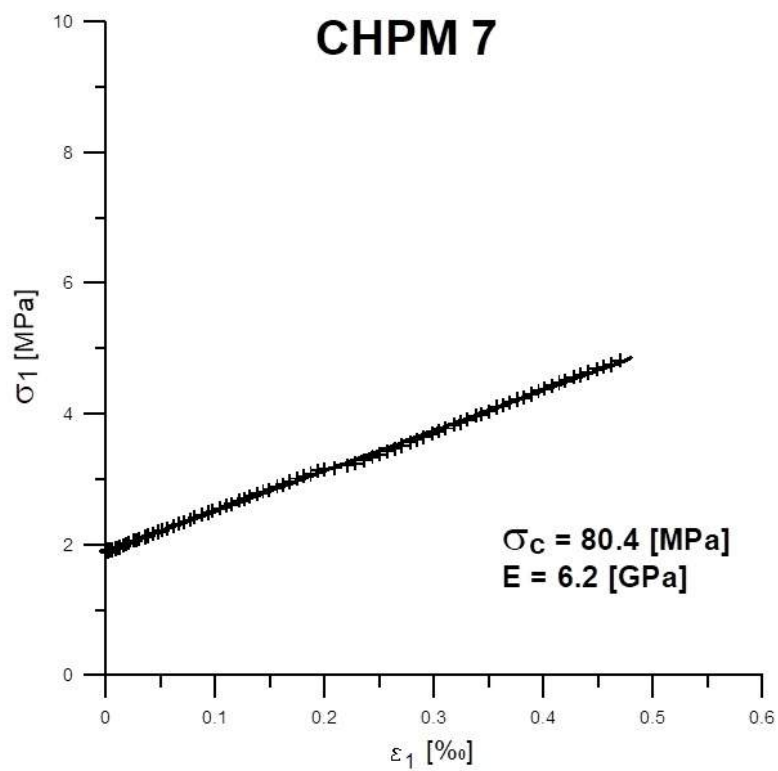


Figure 13: Uniaxial compressive strength and Young's modulus of CHPM7 sample

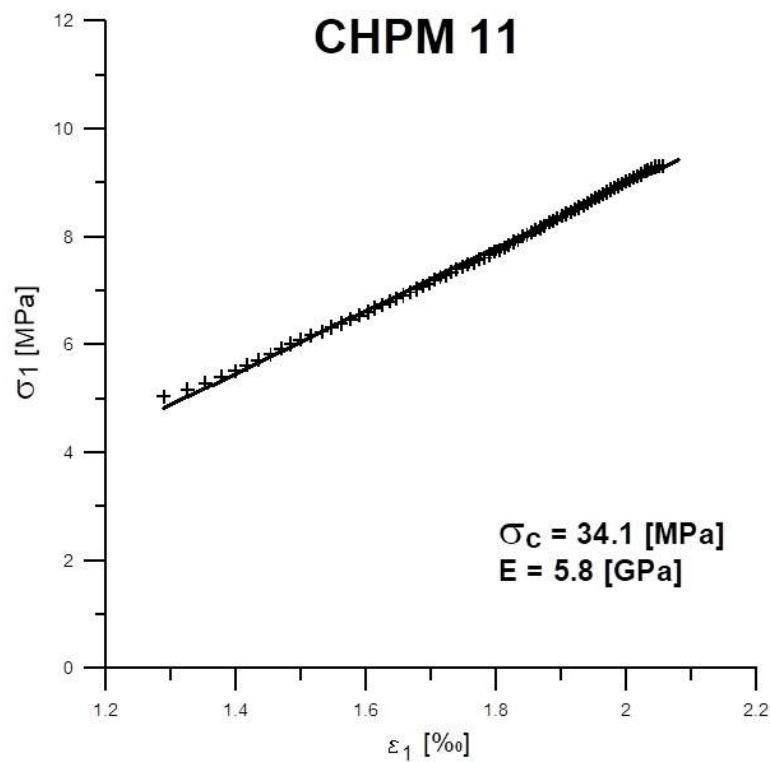


Figure 14: Uniaxial compressive strength and Young's modulus of CHPM11 sample

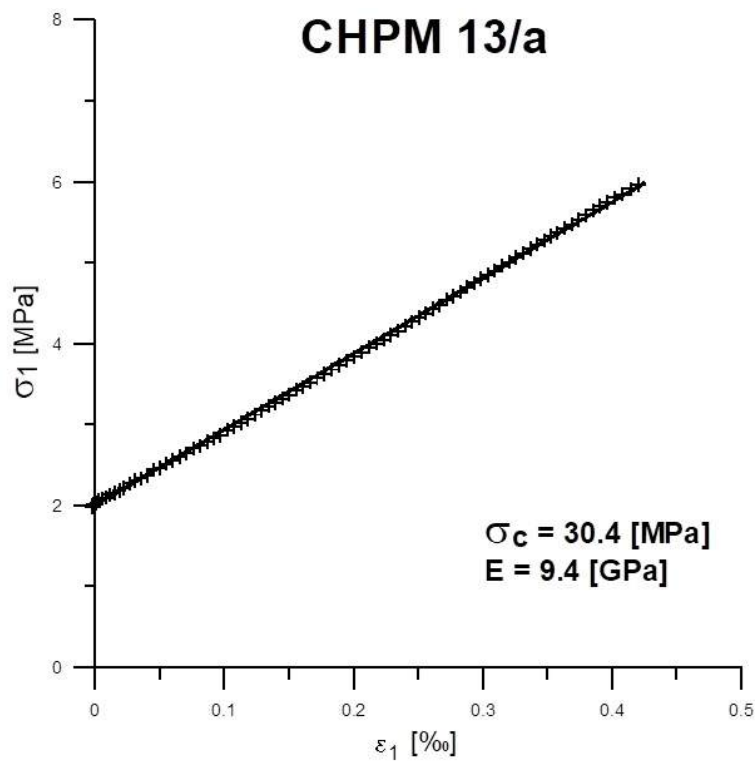


Figure 15: Uniaxial compressive strength and Young's modulus of CHPM13/a sample

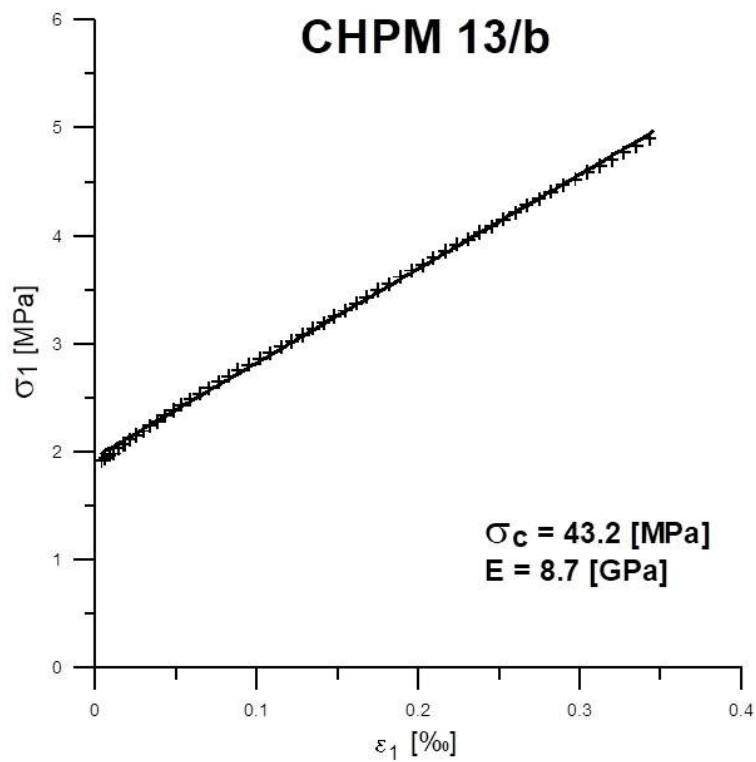


Figure 16: Uniaxial compressive strength and Young's modulus of CHPM13/b sample

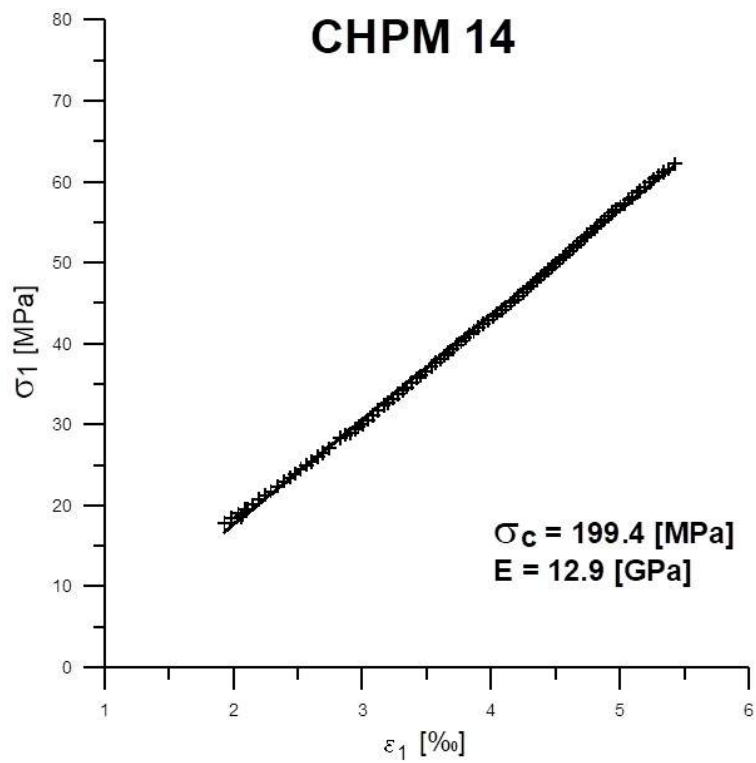


Figure 17: Uniaxial compressive strength and Young's modulus of CHPM14 sample

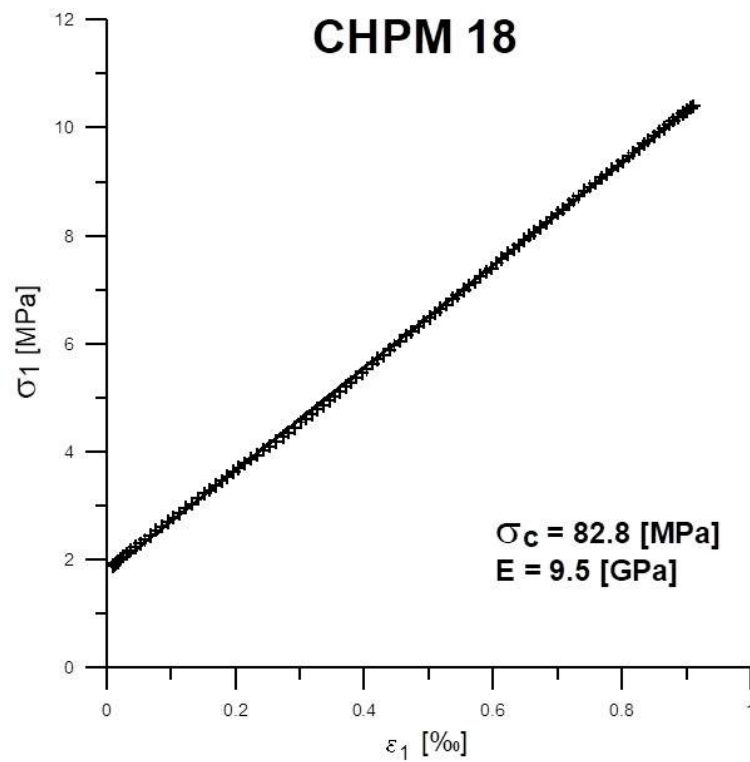


Figure 18: Uniaxial compressive strength and Young's modulus of CHPM18 sample

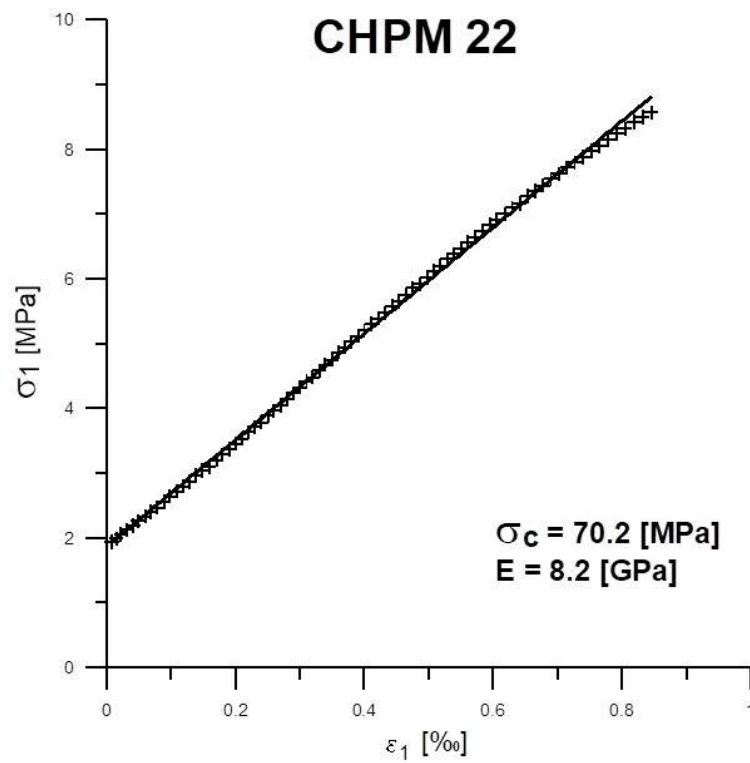


Figure 19: Uniaxial compressive strength and Young's modulus of CHPM22 sample

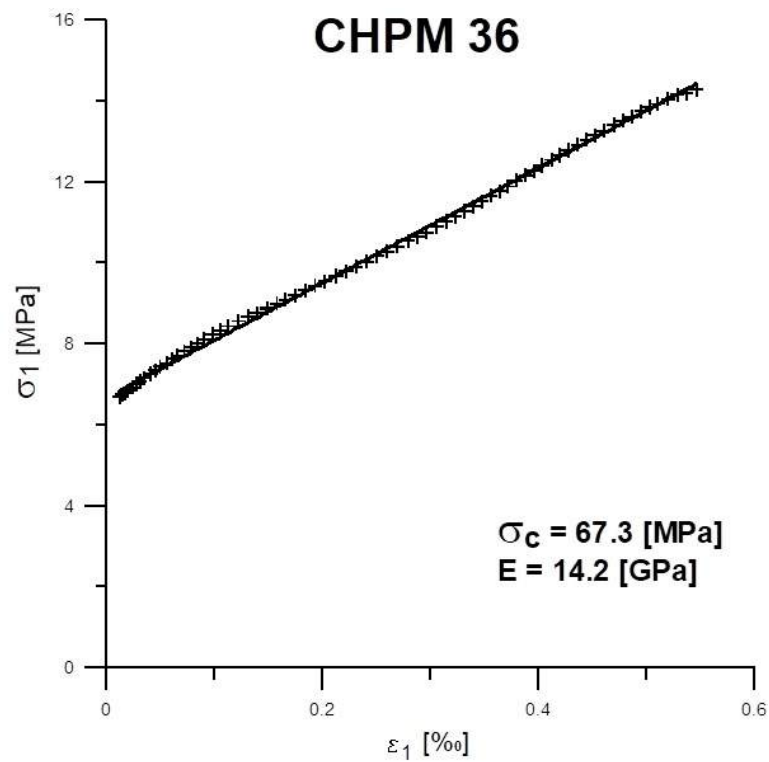


Figure 20: Uniaxial compressive strength and Young's modulus of CHPM36 sample

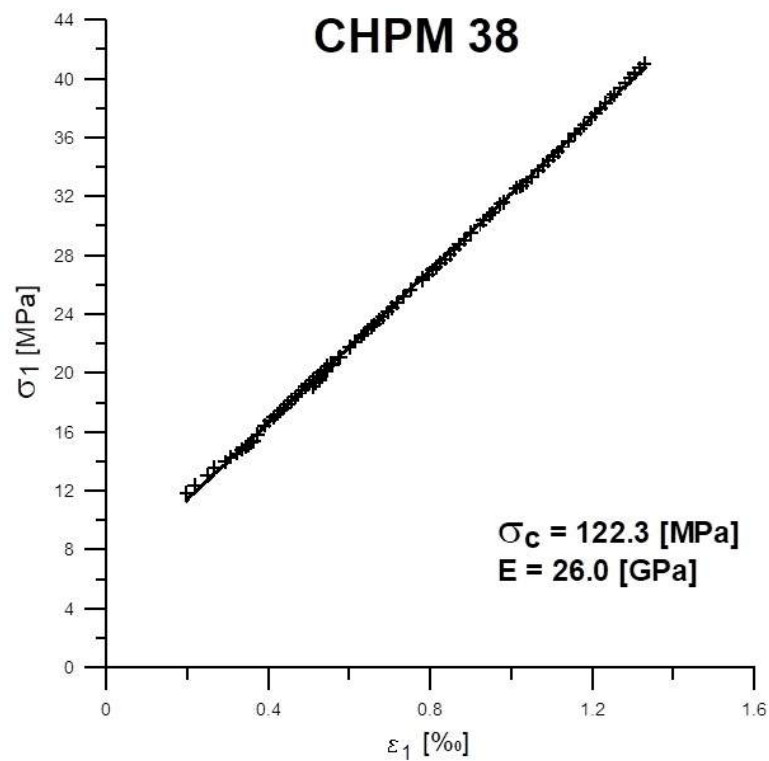


Figure 21: Uniaxial compressive strength and Young's modulus of CHPM38 sample

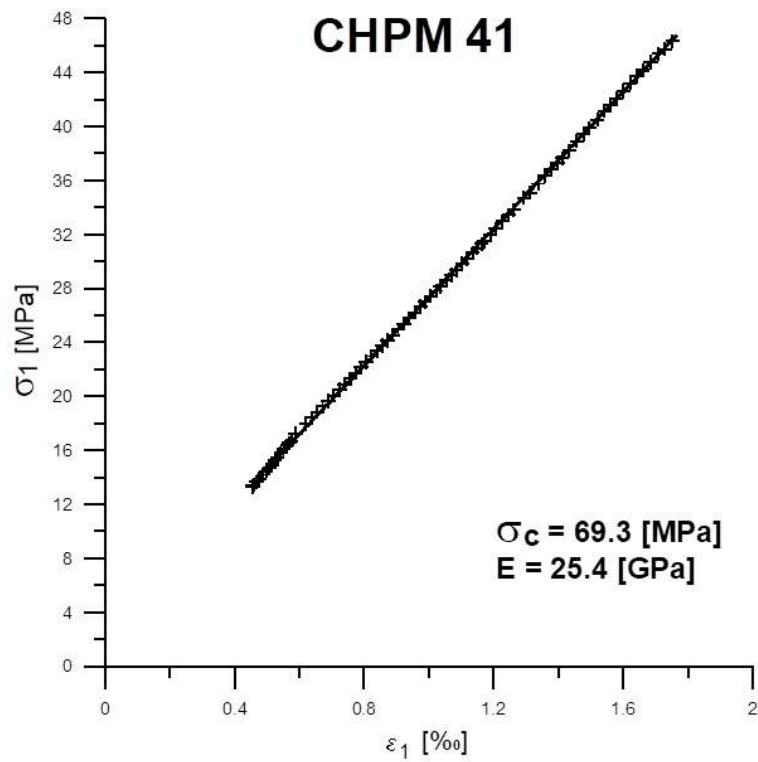


Figure 22: Uniaxial compressive strength and Young's modulus of CHPM41 sample

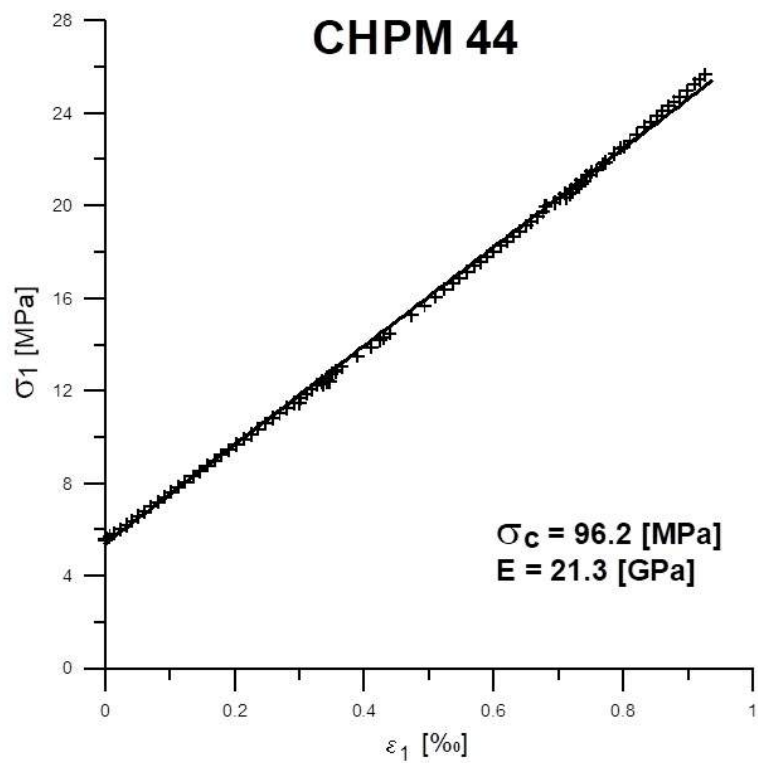


Figure 23: Uniaxial compressive strength and Young's modulus of CHPM44 sample

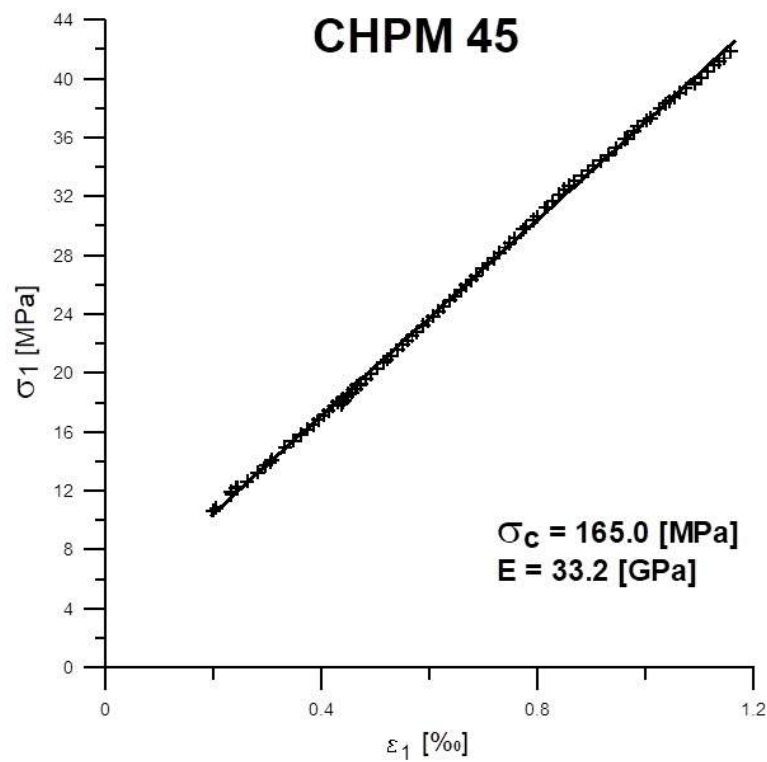


Figure 24: Uniaxial compressive strength and Young's modulus of CHPM45 sample

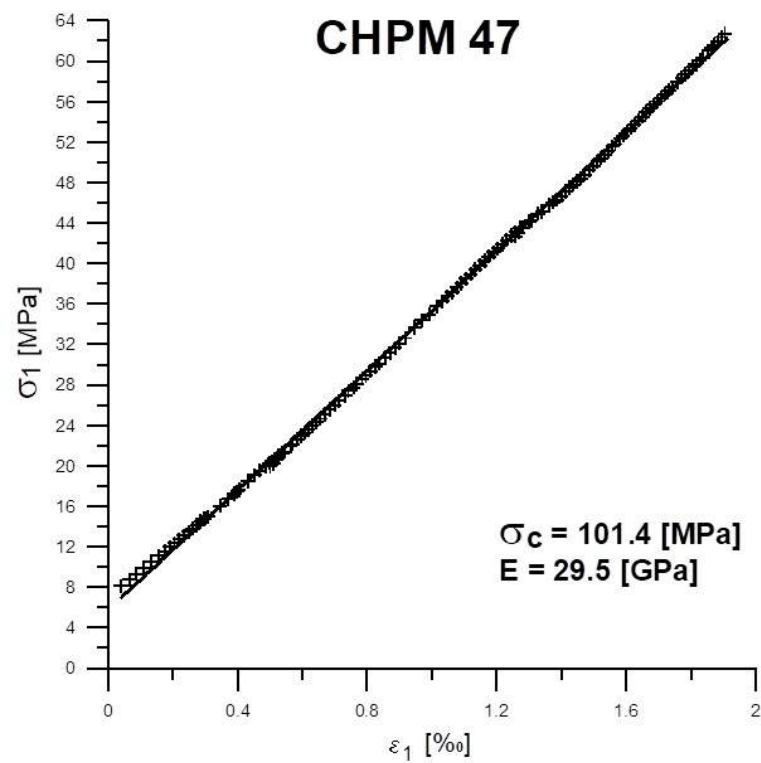


Figure 25: Uniaxial compressive strength and Young's modulus of CHPM47 sample

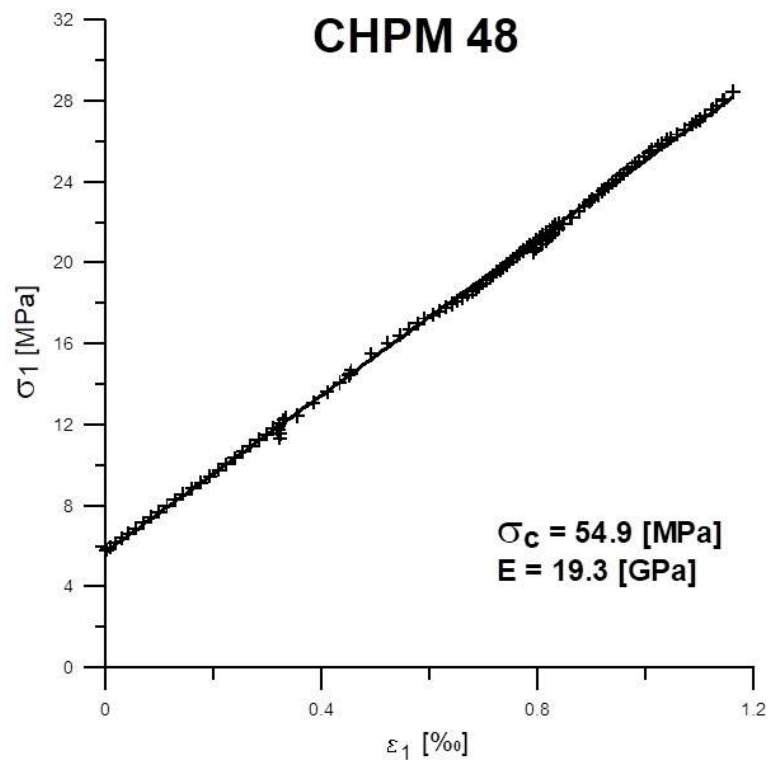


Figure 26: Uniaxial compressive strength and Young's modulus of CHPM48 sample

Hiperbolic Failure Curve

4. sample

Equation of hiperbolic failure curve: $((x+23,58)/19,74)^2 - (y/9,86)^2 = 1$

Relative fault of approximation: 1,02%

Cohesion: 6,4 MPa

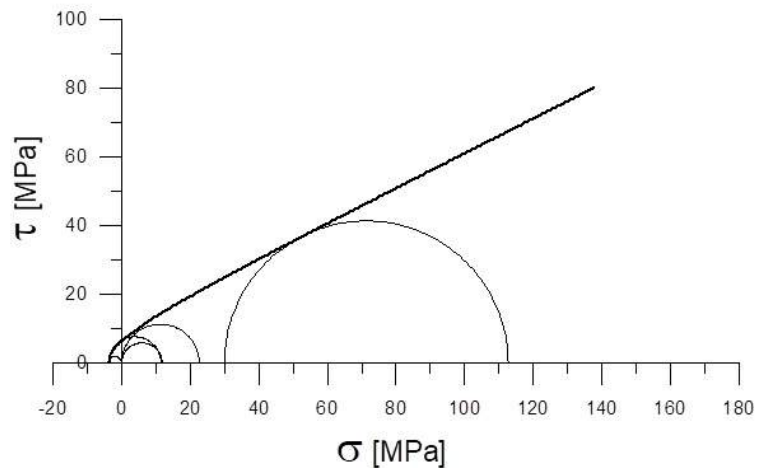


Figure 27: Hyperbolic failure curve and cohesion value of CHPM4 sample

Hiperbolic Failure Curve

5. sample

Equation of hiperbolic failure curve: $((x+24,29)/11,79)^2 - (y/12,16)^2 = 1$

Relative fault of approximation: 2,76%

Cohesion: 21,9 MPa

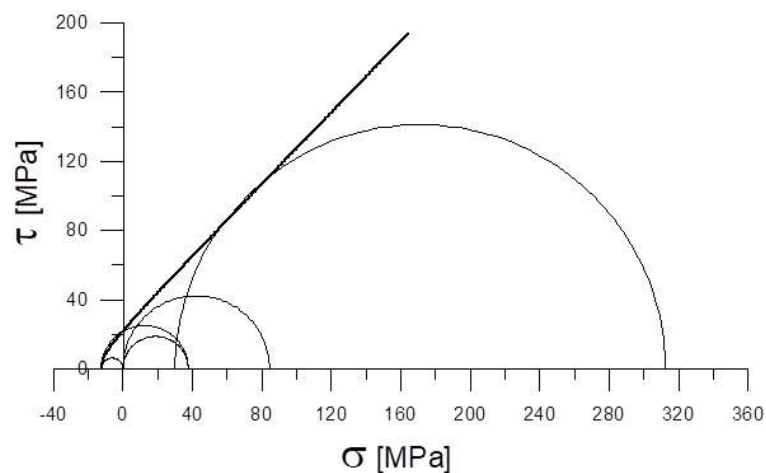


Figure 28: Hyperbolic failure curve and cohesion value of CHPM5 sample

Hiperbolic Failure Curve 6. sample

Equation of hiperbolic failure curve: $((x+17,33)/9,63)^2 - (y/12,18)^2 = 1$

Relative fault of approximation: 1,57%

Cohesion: 18,2 MPa

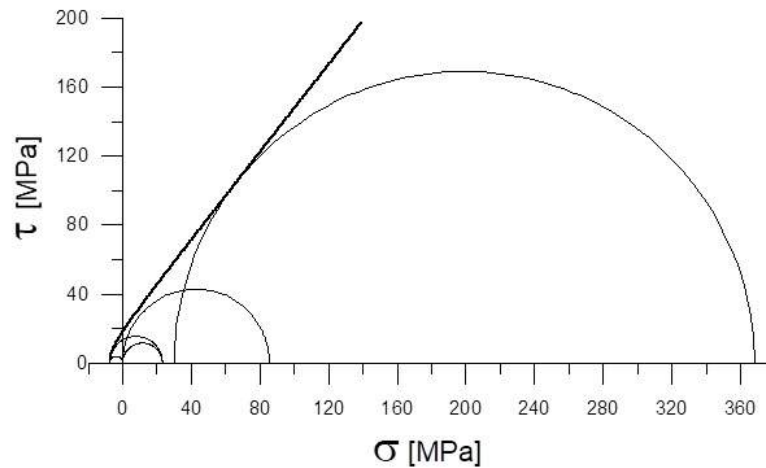


Figure 29: Hyperbolic failure curve and cohesion value of CHPM6 sample

Hiperbolic Failure Curve 11. sample

Equation of hiperbolic failure curve: $((x+23,9)/15,20)^2 - (y/16,26)^2 = 1$

Relative fault of approximation: 5,94%

Cohesion: 19,7 MPa

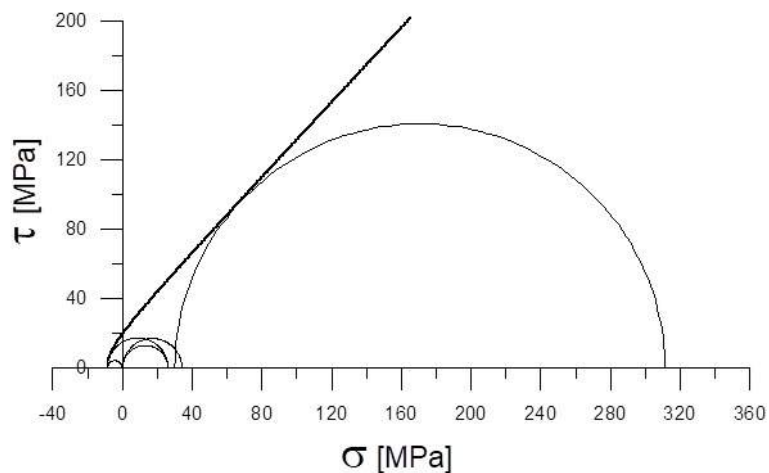


Figure 30: Hyperbolic failure curve and cohesion value of CHPM11 sample

Hiperbolic Failure Curve

14. sample

Equation of hiperbolic failure curve: $((x+46,31)/30,01)^2 - (y/30,63)^2 = 1$

Relative fault of approximation: 0,02%

Cohesion: 36,0 MPa

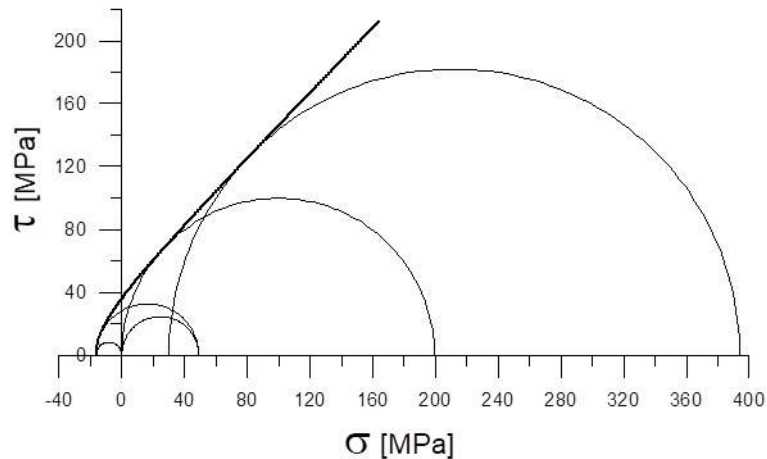


Figure 31: Hyperbolic failure curve and cohesion value of CHPM14 sample

Hiperbolic Failure Curve

22. sample

Equation of hiperbolic failure curve: $((x+307,5)/294,6)^2 - (y/68,5)^2 = 1$

Relative fault of approximation: 2,11%

Cohesion: 20,5 MPa

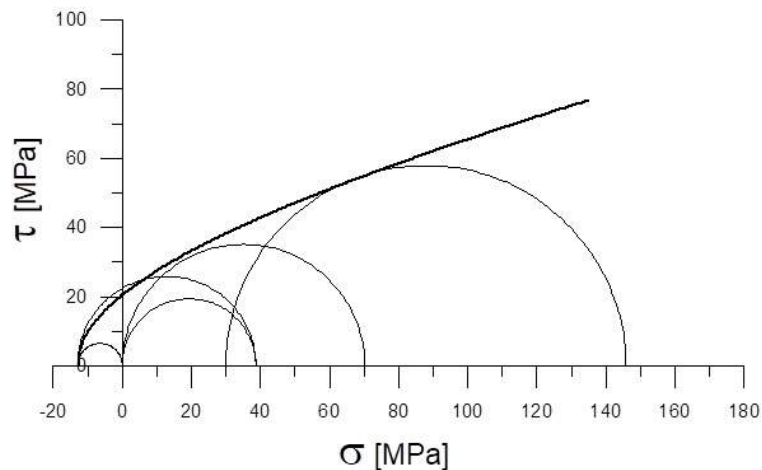


Figure 32: Hyperbolic failure curve and cohesion value of CHPM22 sample

Hiperbolic Failure Curve 38. sample

Equation of hiperbolic failure curve: $((x+44,6)/32,8)^2 - (y/26,6)^2 = 1$

Relative fault of approximation: 0,04%
Cohesion: 24,6 MPa

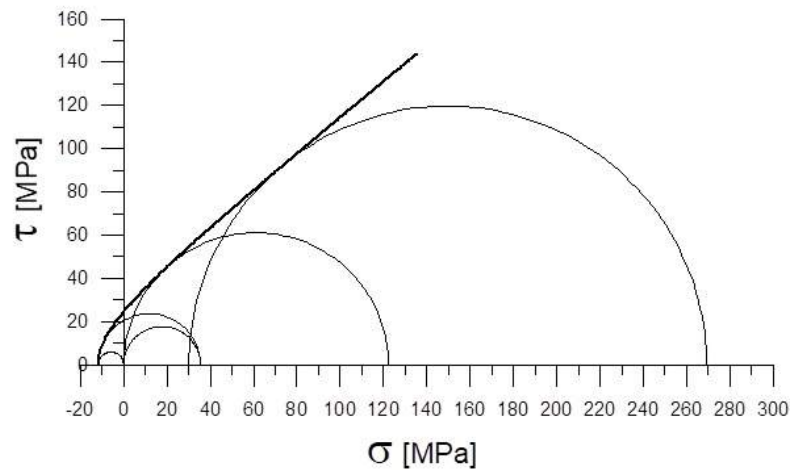


Figure 33: Hyperbolic failure curve and cohesion value of CHPM38 sample

Hiperbolic Failure Curve 45. sample

Equation of hiperbolic failure curve: $((x+104,4)/87,9)^2 - (y/54,7)^2 = 1$

Relative fault of approximation: 0,14%
Cohesion: 35,1 MPa

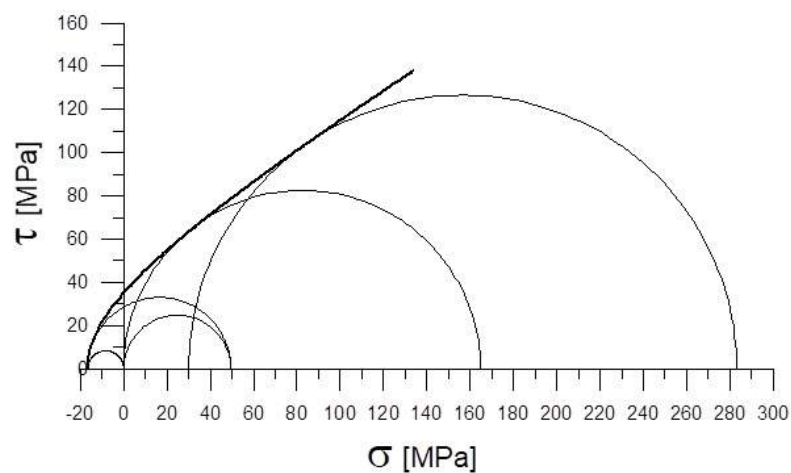


Figure 34: Hyperbolic failure curve and cohesion value of CHPM45 sample

4.3. Conclusions

The laboratory measurements of metallic rocks conducted represent information about the intact rocks investigated. On the bases of these the tensile strength (Brasil) of examined samples ranges between 3.8 MPa and 22.6 MPa, uniaxial compressive strength ranges between 22.6 MPa and 199.4 MPa. These two parameters determine the Brinke value, which refers to the micro fracturing of rocks. In this case the Brinke value is mostly between 3 and 6, only in case of sample number 14, 38, 44 and 47 exceeds 10. This implies that during the stimulation of such reservoir, with technologies such as hydroshearing, the fracture system will decisively be determined by the already existing macro-scale fractures.

5. Fracture enhancement in structures using a variety of laboratory experiments

5.1. Introduction

The goal of this research was to investigate the influence of the laser effect on the strength and the deformability of the intact rock. For this purpose, both uniaxial compressive tests (UCT) and indirect tensile tests (ie. Brasil tests) were carried out in accordance with the Suggested Method of the International Society for Rock Mechanics (Ulusay & Hudson, 2006). The preparation of the samples followed the instruction of the ISRM too. Note: up to now the investigations done were only two main rock mechanical investigation types, but in the future the influence of the laser shock for the rock will be measured in the case of triaxial test. A special triaxial test equipment is under construction at the moment – naturally, the experience of the uniaxial compressive tests will be used in the triaxial tests. It can be also mentioned, that if the tensile strength and the uniaxial compressive strength is well known, the failure criteria of the intact rock can be calculated.

Two different types of rock were investigated in this research: the quasi homogeneous, very high strength aphanitic andesite and a crystalline (porphyritic) granite. The primary aim of the research was to determine the influence of the laser on these rock types. These rocks were collected in Hungary because quantity of CHPM samples was not enough for this type of investigation.

In the first part of this report we present the results of the laboratory tests. In the second part interpretation methods and the values measured are analyzed. Finally, in the conclusions we will summarize the results and suggest new tests in the future.

5.2. Experimental laser set

The research team of ZERLUX Ltd. has been engaged in the development of laser technology solutions in downhole conditions for several years in Hungary. Recent developments on the fields of laser technology enable us to use low energy loss high power laser devices (HPLD) even at large depths via the new standard high carrying capacity optical fibers (Kovács et al, 2016). Their system is comprised of a high-power laser generator and a custom design directional laser drilling head. In this phase of the development the laser technology is particularly well suited to cost efficiently drill short laterals in the rock (Figure 35).



Figure 35: High power laser devices set by ZERLUX Ltd.

The heat stress on the rock, generated by the laser beam, results in micro fractures in the immediate vicinity of the section treated with laser. A laser device with 1.5 kW laser beam power was applied for the rock mechanic investigations by ZERLUX Ltd (Figure 35). If this process proves to be successful, we will have a chance to develop a laser tool to control the shape of the fractured rock volume without increasing the pressure while hydraulic fracturing (Kovács et al., 2014).

Using the laser, the influence of the laser shock inside the sample was investigated. The shock was applied at constant stress. The strain of the sample was continuously measured. Unfortunately, the horizontal (radial) strain could not be detected due to the high temperature.

The applied constant stress was calculated from the whole stress-strain curve: it was around, but not more than 4 % of the peak stress (ie. the strength) of the rock. Thus, the Young's modulus of the rock can be calculated.

Hypothetical stress–strain curves for three different rocks are presented in Figure 9 according to Ramamurthy et al. (2017). According to their figure, curves OA, OB and OC represent three stress–strain curves with failure occurring at A, B and C, respectively. According to their sample, curves OA and OB have same modulus but different strengths and strains at failure, whereas curves OA and OC have same strength but different moduli and strains at failure. This implies that neither the strength nor the modulus can be chosen to represent alone the overall quality of the rock. Rather, strength and modulus together will give a realistic understanding of the rock response for engineering usage. This approach to define the quality of intact rocks was proposed by Deere and Miller (1966) by considering the modulus ratio (MR), which is defined as the ratio of tangent modulus of the intact rock (E) at 50 % of failure strength and its compressive strength (σ_c).

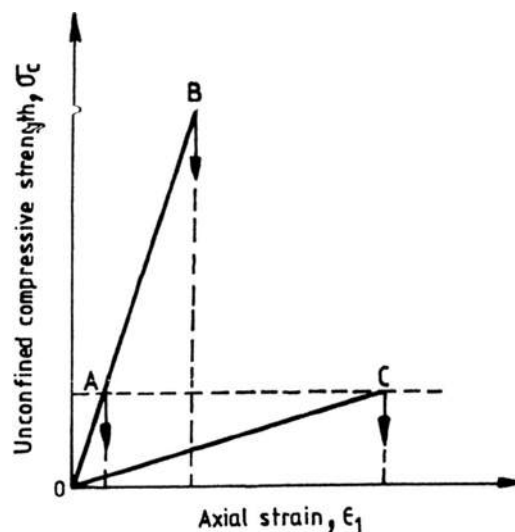


Figure 36: Hypothetical stress–strain curves (Ramamurthy et al. 2017)

The modulus ratio $MR = E/\sigma_c$ between the modulus of elasticity (E) and uniaxial compressive strength (σ_c) for intact rock samples varies from 106 to 1600 (Palmström & Singh, 2001). For most rocks MR is between 250 and 500 with average $MR = 400$; ie. $E = 400 \sigma_c$

Palchik (2011) examined the MR values for 11 heterogeneous carbonate rocks from different regions of Israel. The investigated dolomites, limestones and chalks had weak to very strong strength with wide range of elastic modulus. He found that MR is closely related to the maximum axial strain ($\varepsilon_{a,max}$) at the uniaxial strength of the rock (σ_c) and the following relationship was found (see Figure 37):

$$MR = \frac{2k}{\varepsilon_{a,max} (1 + e^{-\varepsilon_{a,max}})} \quad (3)$$

where k is a conversion coefficient equal to 100, and $\varepsilon_{a,max}$ is in %. When MR is known, $\varepsilon_{a,max}$ (%) is obtained from E. (3) as:

$$\varepsilon_{a,max} = \frac{k}{MR - 0.46k} \quad (4)$$

since the expansion of the expression $2/(1 + e^{-\varepsilon_{a,max}})$ using Taylor's theorem shows the value of $2/(1 + e^{-\varepsilon_{a,max}}) = 1 + 0.46 \varepsilon_{a,max}$ (Palchik, 2013).

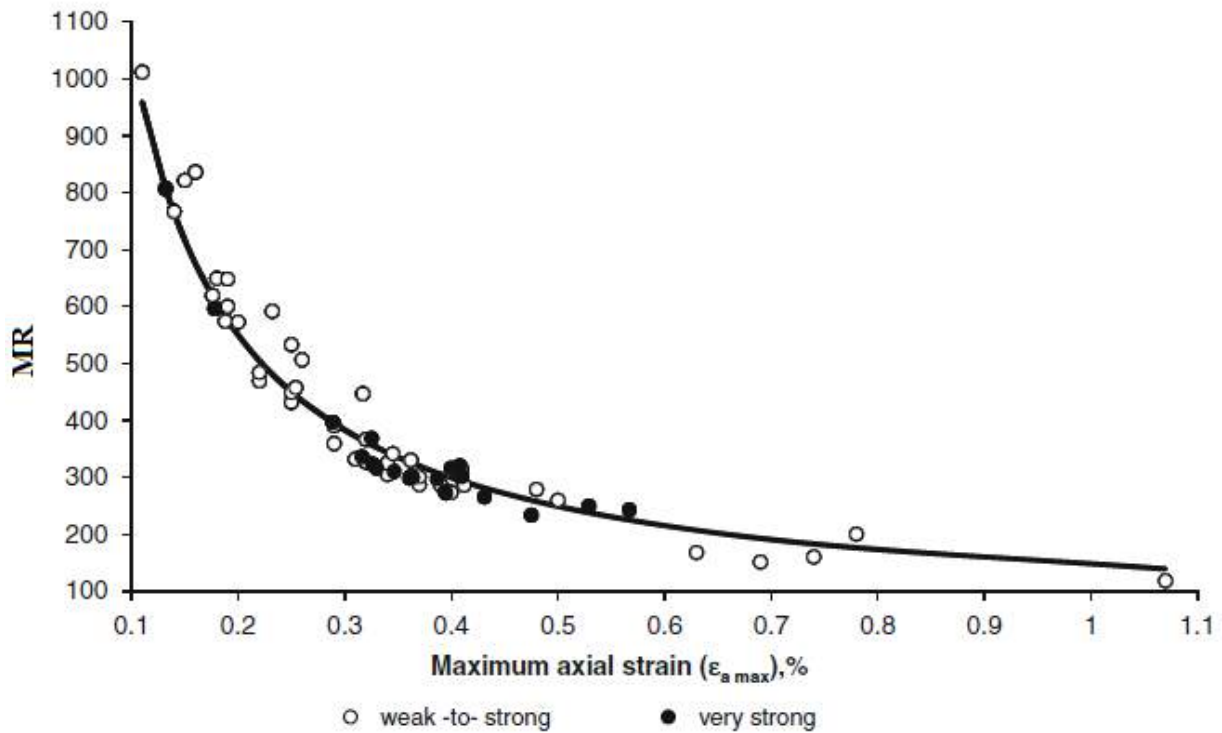


Figure 37: Relationship between modulus ratio (MR) and maximum axial strain ($\varepsilon_{a,max}$) using different carbonate rocks (Palchik, 2011)

The Hungarian granitic rocks were analyzed according to the above presented method (see Figure 38). It was found, that MR is between 300 and 600, and exponentially decreasing with the maximum axial strain (Vásárhelyi et al, 2016).

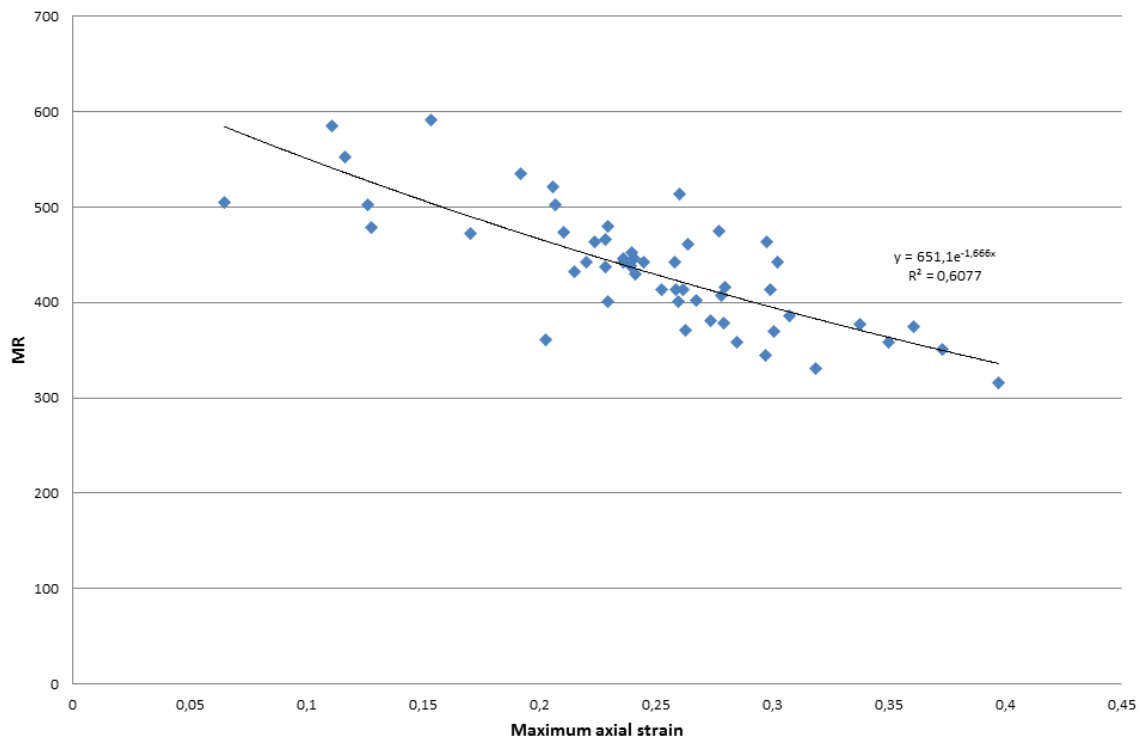


Figure 38: Relationship between modulus ratio (MR) and maximum axial strain on Hungarian granitic rocks

5.3. Indirect (Brazilian) tests - execution and interpretation

In the Brazilian test, a disc shape specimen of the rock is loaded by two opposing normal strip loads at the disc periphery. The load is continuously increased at a constant rate until failure of the sample occurs. The loading rate depends on the material and may vary from 10 to 50 kN/min. At the failure, the tensile strength of the rock is calculated as follows:

$$\sigma_t = 2P/(\pi DL) \quad (5)$$

where P is the applied load, D and L are the diameter and the thickness of the sample, respectively. The above equation uses the theory of elasticity for isotropic continuous media and gives the tensile stress perpendicular to the loaded diameter at the center of the disc at the time of failure. Figure 39 represents the experimental setup before laser treatment and in Figure 40, the test procedure is presented before (Figure 41) and after the failure.



Figure 39: Experimental setup before laser treatment

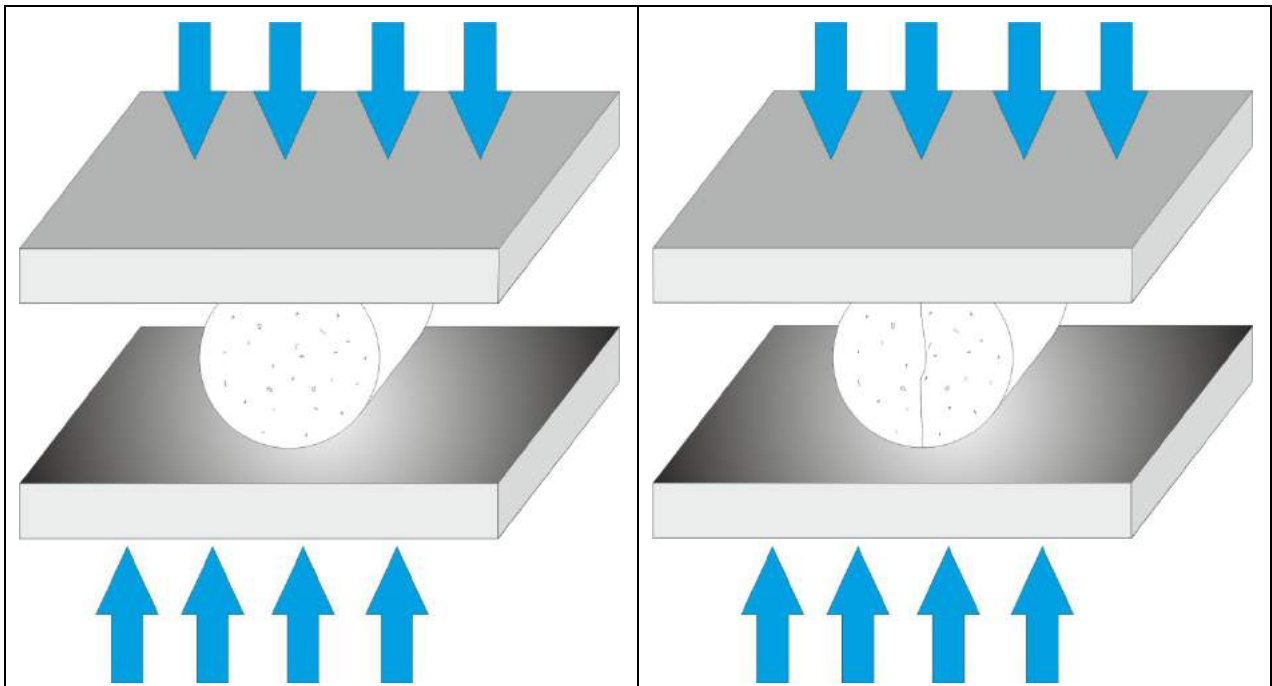


Figure 40: Brazilian (indirect) tensile test – before and after the failure

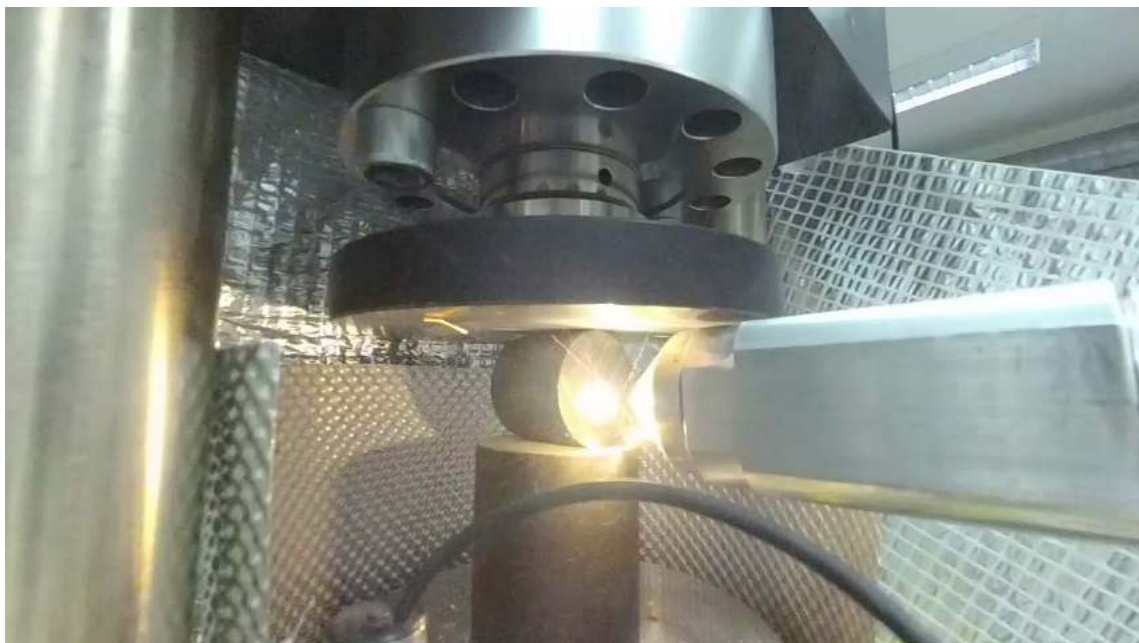


Figure 41: Experimental setup during laser treatment

It is well known, that the failure of the rock will occur due to the tensile normal stress of the cracks in the rock – so the influence of the laser shock in the middle of the Brazilian tests is highly important in this research (Figure 42).

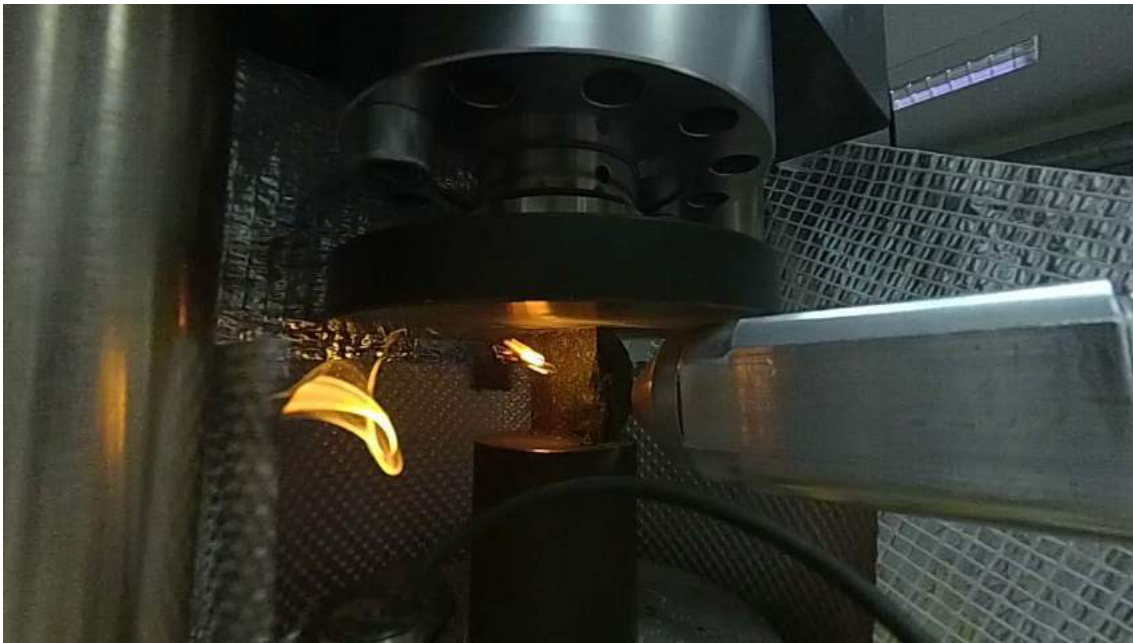


Figure 42: Failure of the rock sample

5.4. Results of andesite tests

Firstly, both the uniaxial compressive strength and tensile strength of the intact rock were determined without applying laser.

The tensile strengths are calculated in Table 9. and the tensile stress – lateral strain relationships are represented on the Figure 43. The average tensile strength of the investigated andesite was 12 MPa with a standard deviation of 2.9 MPa. The minimum value of the tensile strengths was 7.7 MPa, the maximum value 17.0 MPa (Table 9).

Table 9: Results of the indirect tensile strength tests on andesite without laser

	Density [kg/m ³]	Tensile Strength [MPa]
20171129_Andezit_Br_1	2664	11.1
20171129_Andezit_Br_2a	2698	10.5
20171129_Andezit_Br_2b	2698	9.8
20171130_Andezit_Br_1	2686	14.7
20171130_Andezit_Br_2	2681	7.7
20171130_Andezit_Br_3	2666	17.0
20171130_Andezit_Br_4	2687	10.9
20171130_Andezit_Br_5	2682	14.4
average	2683	12
standard deviation	12.0	2.9

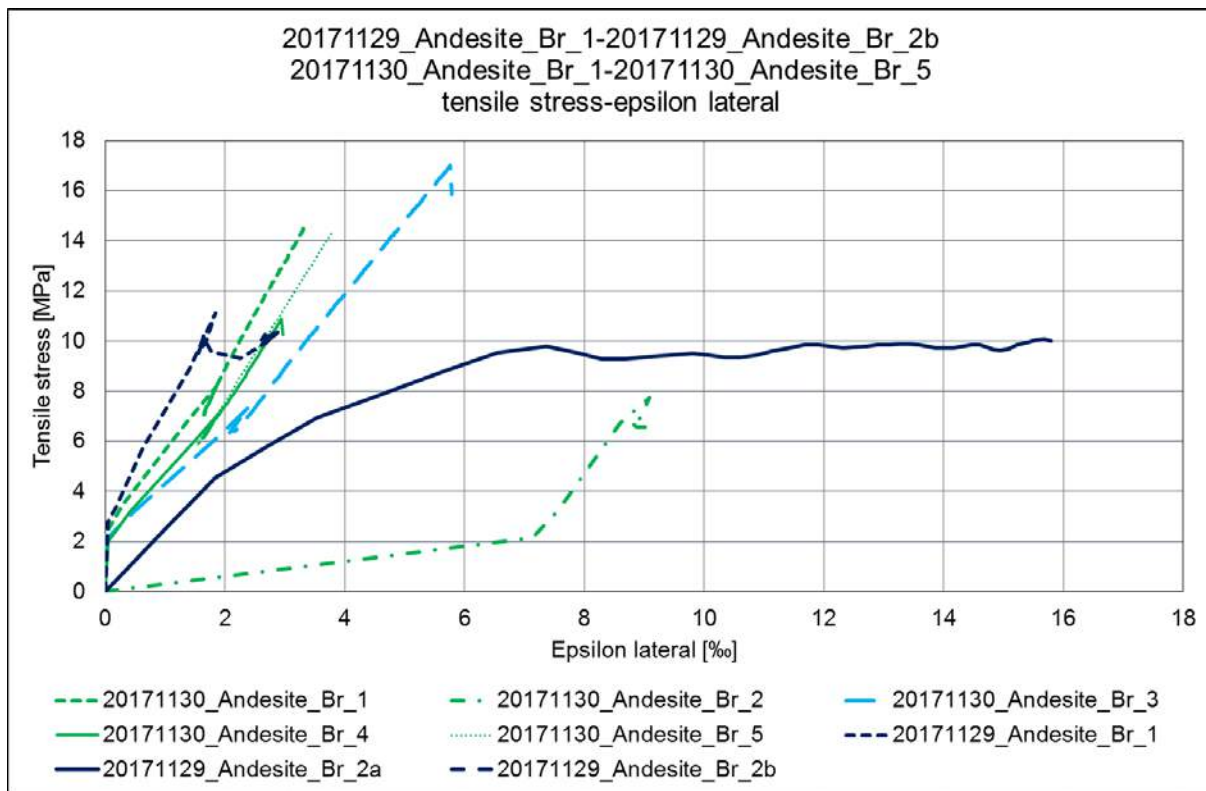


Figure 43: Relationship between tensile stress and lateral strain on andesite without laser

Uniaxial compressive strengths (Table 10) and the relationship between the uniaxial compressive stress and the axial strain were calculated from the results of the uniaxial compressive strength tests (Figure 44). The Young's modulus at 50 % of the ultimate compressive strength was determined from the slope of the uniaxial compressive stress- axial strain curve was. The modulus ratios MR between the Young's modulus and uniaxial compressive strength were also calculated (Table 10).

5.5. Results of uniaxial compressive strength tests on andesite without laser

The average of the uniaxial compressive strength of the investigated andesite was 330 MPa with a standard deviation of 20.4 MPa. The minimum value of the tensile strengths was 304 MPa, the maximum value 354 MPa (Table 10). The average of the Young's modulus was 40 GPa with a standard deviation of 2.9 GPa. The average of the modulus ratios was 121 with a standard deviation of 8.9 (Table 10). The maximal axial strain reached the value between 8 and 10 per mill (Figure 44).

Table 10: Results of uniaxial compressive strength tests on andesite without laser

	Density [kg/m ³]	Uniaxial compressive strength σ_c [MPa]	Young modulus E [GPa]	MR (E/ σ_c)
20171130_Andesite_Ua_1	2677	354.2	39.2	110
20171130_Andesite_Ua_2	2664	330.6	43.8	132
20171130_Andesite_Ua_3	2670	304.2	36.7	120

average	2670	330	40	121
standard deviation	5.3	20.4	2.9	8.9

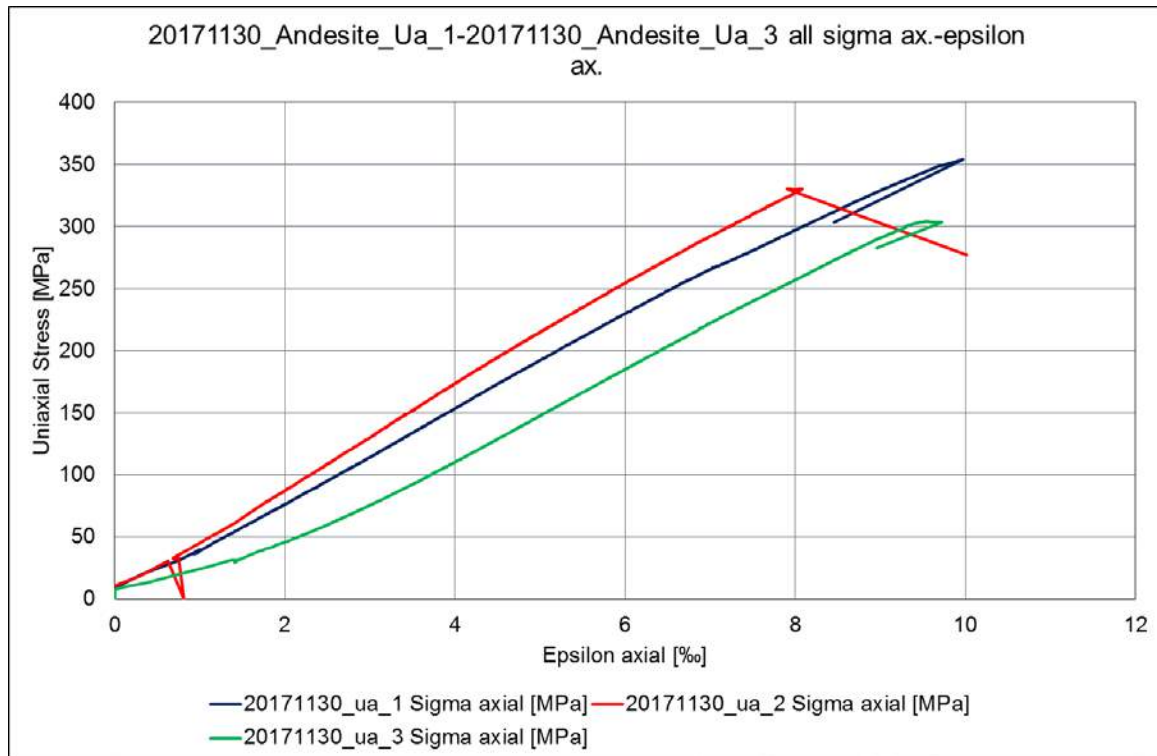


Figure 44: Relationship between uniaxial compressive stress and axial strain on andesite without laser

For the study of the effect of laser radiation on the strength of volcanic rock samples the uniaxial compressive strength and tensile strength were determined with applying laser.

5.6. Results of the indirect tensile strength test on andesite with laser radiation

In the case of the indirect tensile strength test the focus of the laser beam was either on the base or on the mantle of the samples. The laser distance was 2cm from the surface of the sample. During the tests the sample was loaded up to an adjusted constant load and during this constant load either the base or the mantle of the sample was radiated with laser (Figure 45-51). The value of the adjusted constant load was between 4.4 and 8.4 MPa (Table 11 and Figure 45). In every case the sample was broken quickly after the start of the laser radiation. During the laser heat load the lateral strain was significantly increased (Figure 45-51) which is the signal of the formation and spread of micro cracks in the rock structure.

Table 11: Results of the indirect tensile strength test on andesite with laser

	Density [kg/m ³]	Tensile strength σ_t [MPa]	Laser distance	Laser focus place
20171207_Andesite_Laser_Br_1_mantle	2664	8.4	2 cm	mantle
20171207_Andesite_Laser_Br_2_mantle	2670	8.4	2 cm	mantle
20171207_Andesite_Laser_Br_3_mantle	2687	5.6	2 cm	mantle
20171207_Andesite_Laser_Br_8_base	2685	8.4	2 cm	base
20171207_Andesite_Laser_Br_9_base	2785	4.4	2 cm	base
average	2698	7.1		
standard deviation	44.1	1.7		

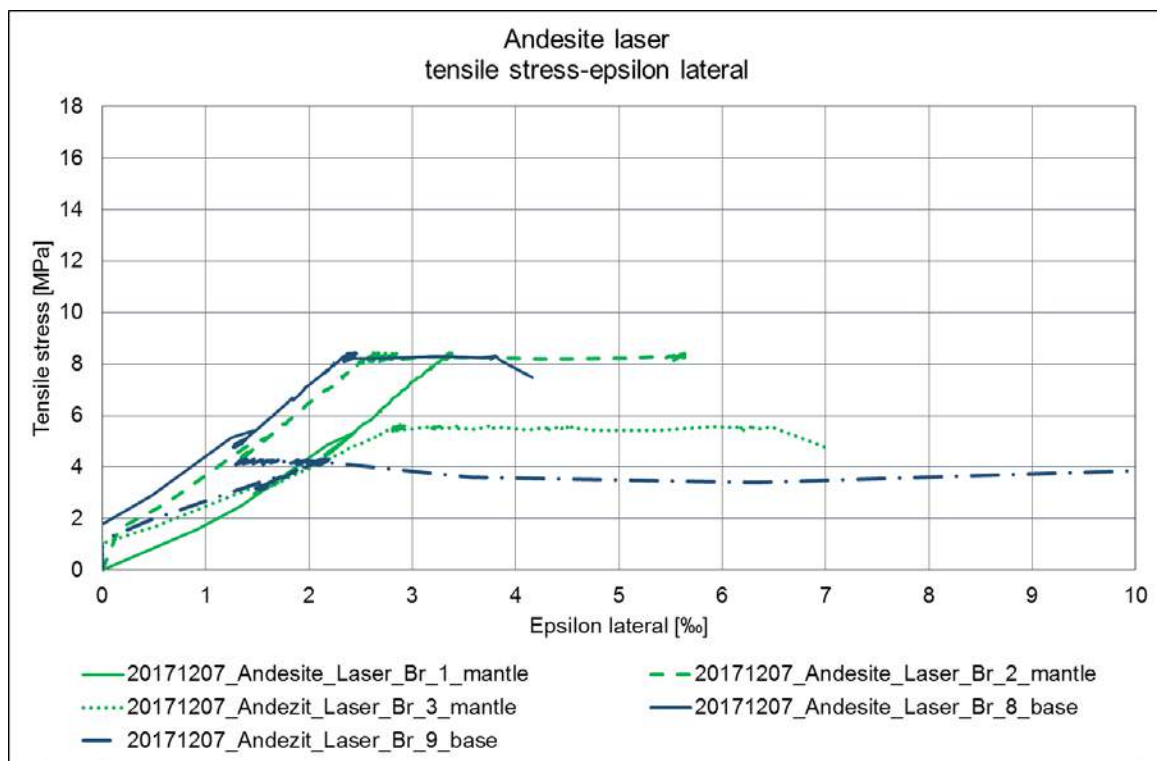


Figure 45: Relationship between tensile stress and lateral strain on andesite under laser radiation

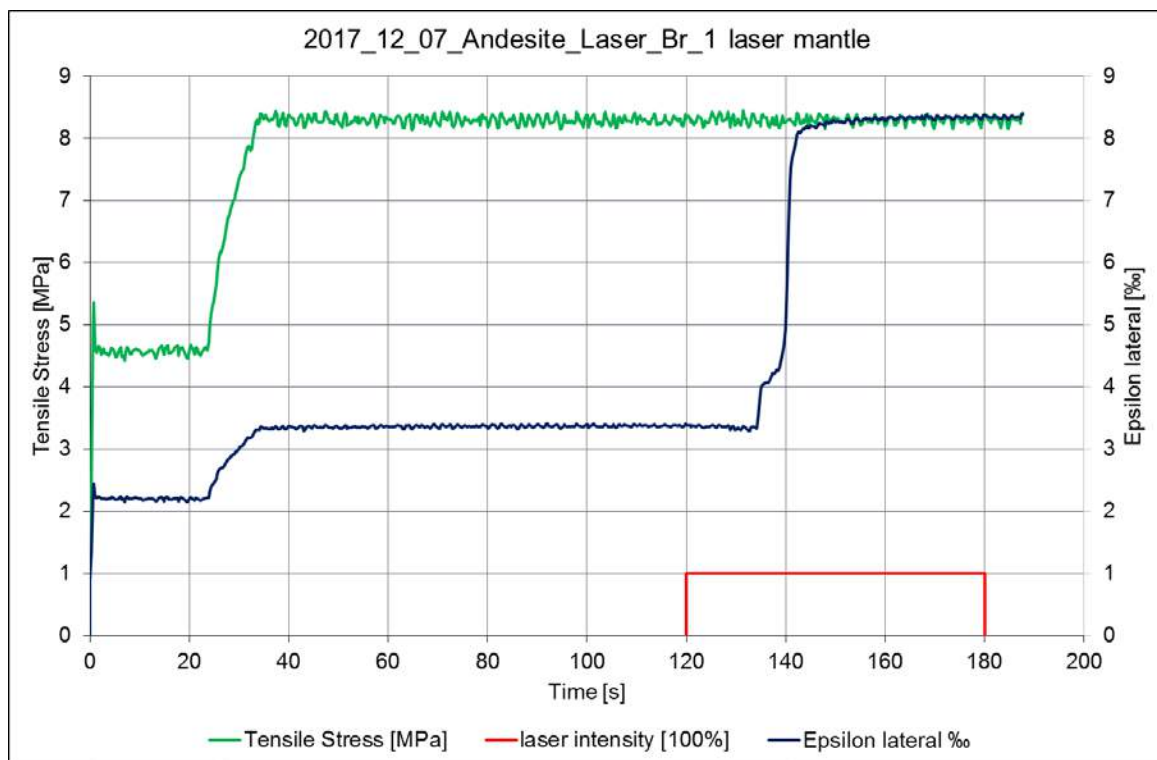


Figure 46: Relationship between tensile stress and time as well as lateral strain and time on andesite under laser radiation on the mantle of the sample

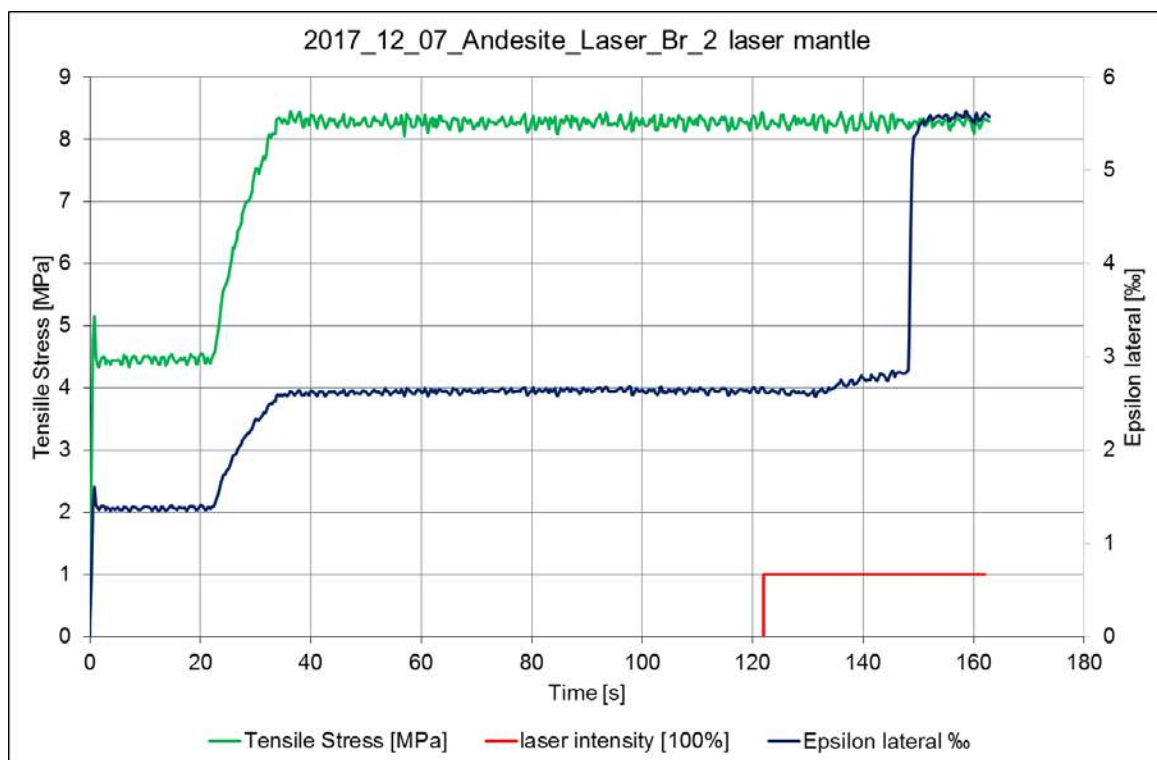


Figure 47: Relationship between tensile stress and time as well as lateral strain and time on andesite under laser radiation on the mantle of the sample

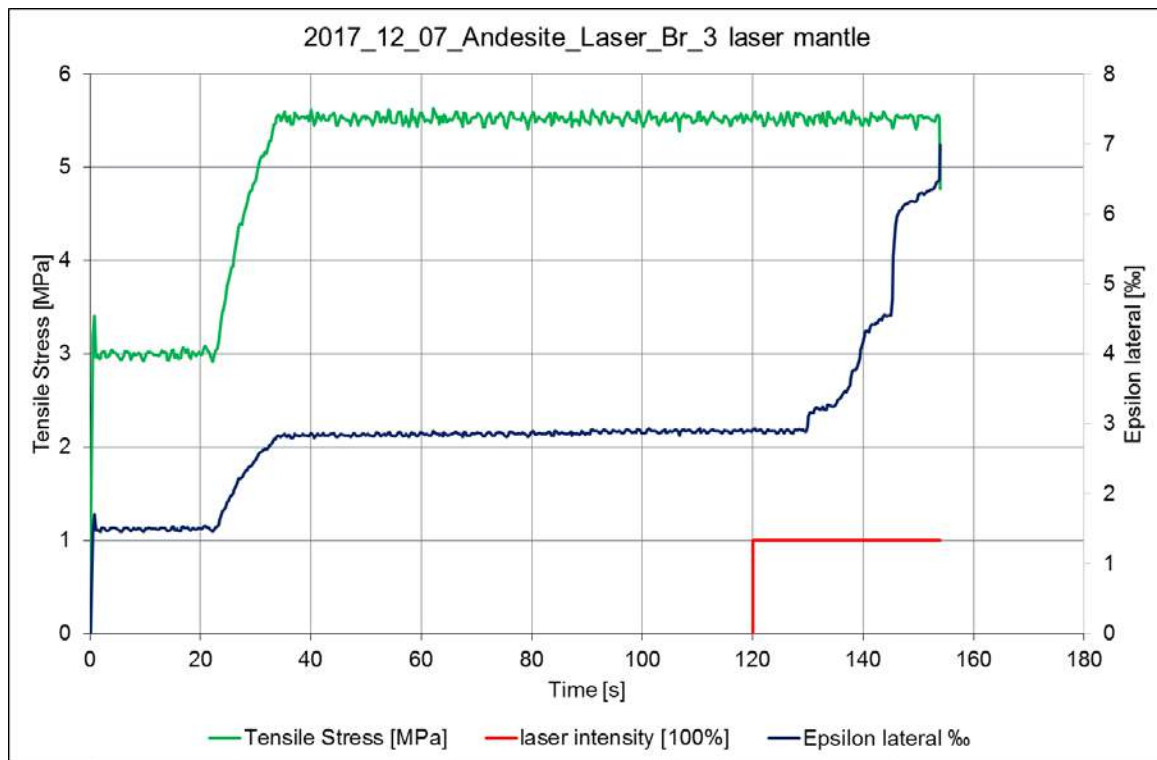


Figure 48: Relationship between tensile stress and time as well as lateral strain and time on andesite under laser radiation on the mantle of the sample

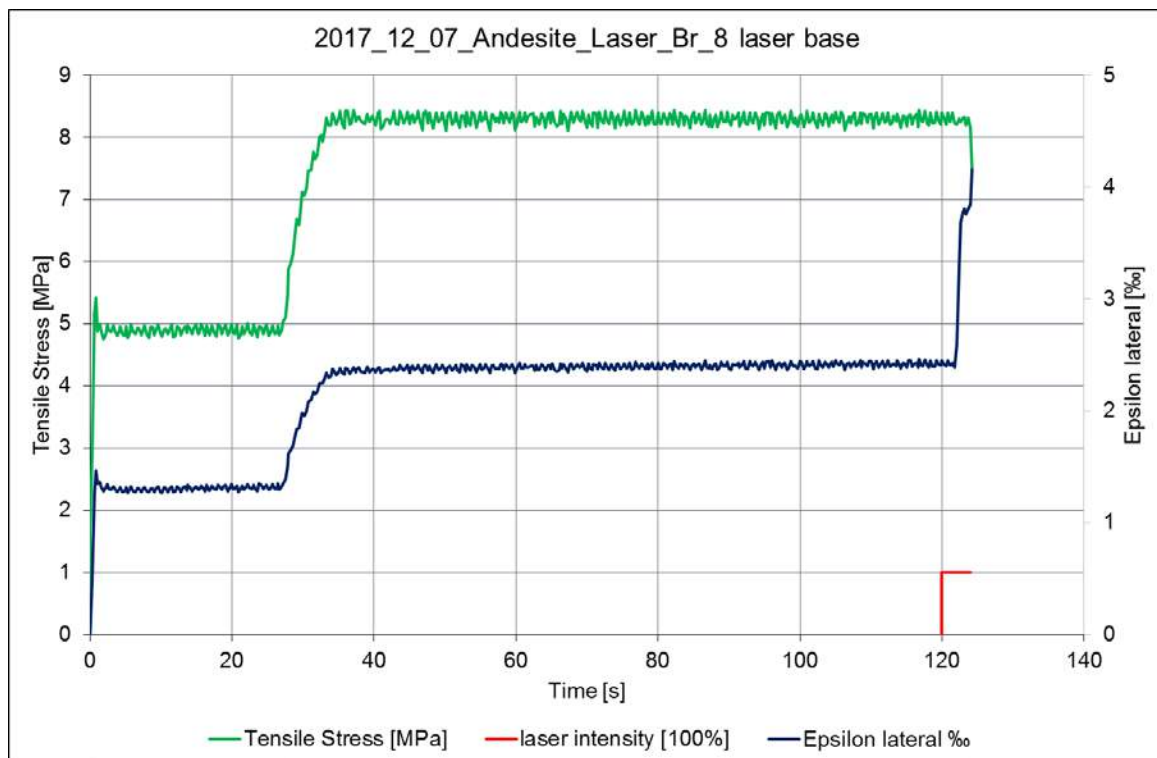


Figure 49: Relationship between tensile stress and time as well as lateral strain and time on andesite under laser radiation on the base surface of the sample

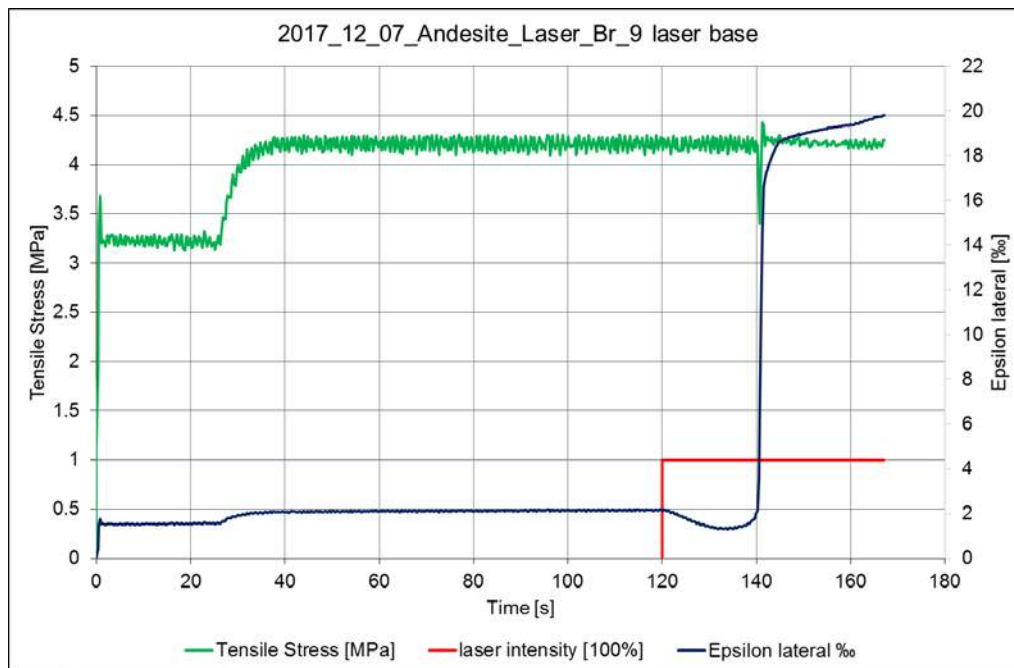


Figure 50: Relationship between tensile stress and time as well as lateral strain and time on andesite under laser radiation on the base surface of the sample

5.7. Results of the uniaxial compressive strength tests on andesite with laser radiation

In the case of the uniaxial compressive strength test the focus of the laser beam was on the mantle of the samples at half the height of the samples. The laser distance was 2 cm from the surface of the sample (Figure 51). During the tests the sample was loaded up to an adjusted constant load and during this constant load the mantle of the sample was radiated with laser (Figure 53-64). The value of the adjusted constant load was 145, 175 and 195 MPa (Table 12 and Figure 53-64), this is 45-55% of the uniaxial compressive strength value of the laser with not loaded andesite (Table 10). In every case the sample was radiated with laser beam cyclically. The heat load and the undercooling cycle was held up to 1 min, 2 min and 3 min separately. During the laser heat load the sample was dilated in axial direction and during the cooling cycle it was smaller (Figure 53-64) which is the sign of the formation and spread of micro cracks in the rock structure by heating and the closing of this cracks by the cooling cycle (Figure 52).

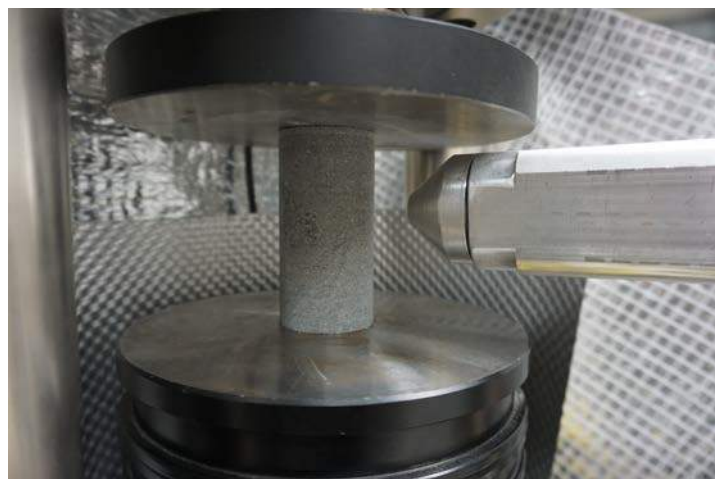


Figure 51: Experimental setup during laser treatment



Figure 52: Failure of the rock sample over time

Table 12: Results of the uniaxial compressive strength test on andesite with laser

	Density [kg/m ³]	Uniaxial compressive strength (σ_c) [MPa]	Young modulus E [GPa]	MR (E/σ_c)
2017_11_29_Andesite_Laser_Ua_2	2659	145.5	39.8	274
2017_11_29_Andesite_Laser_Ua_3	2659	191.7	41.2	215
2017_11_29_Andesite_Laser_Ua_4	2684	191.7	46.7	244
2017_12_01_Andesite_Laser_Ua_1	2707	175.7	38.9	221
2017_12_01_Andesite_Laser_Ua_2	2660	175.8	36.3	207
2017_12_01_Andesite_Laser_Ua_3	2661	175.6	35.0	199
2017_12_01_Andesite_Laser_Ua_4	2668	175.8	35.8	204
2017_12_01_Andesite_Laser_Ua_5	2707	176.0	38.5	219
2017_12_01_Andesite_Laser_Ua_6	2706	176.1	39.6	225
2017_12_01_Andesite_Laser_Ua_7	2664	175.8	33.0	187
average	2677	176	38	219
standard deviation	20.1	11.9	3.6	23.3

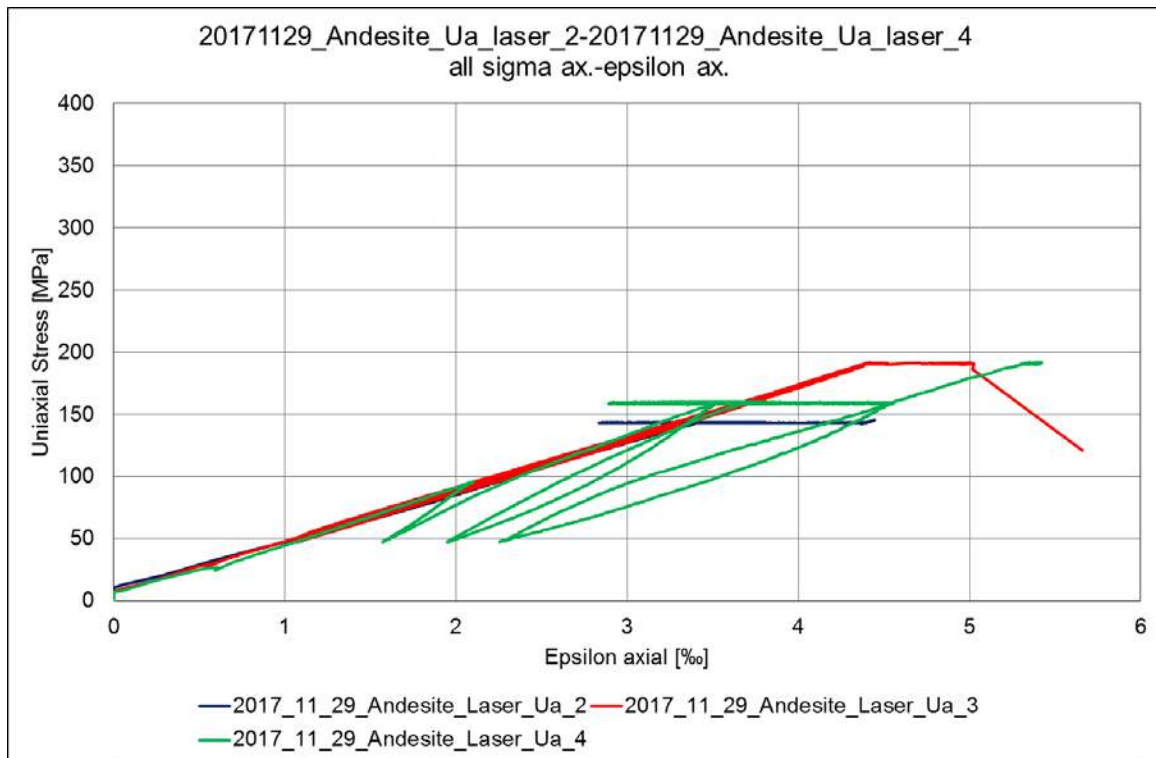


Figure 53: Relationship between uniaxial compressive stress and axial strain on andesite under laser radiation on the mantle of the sample

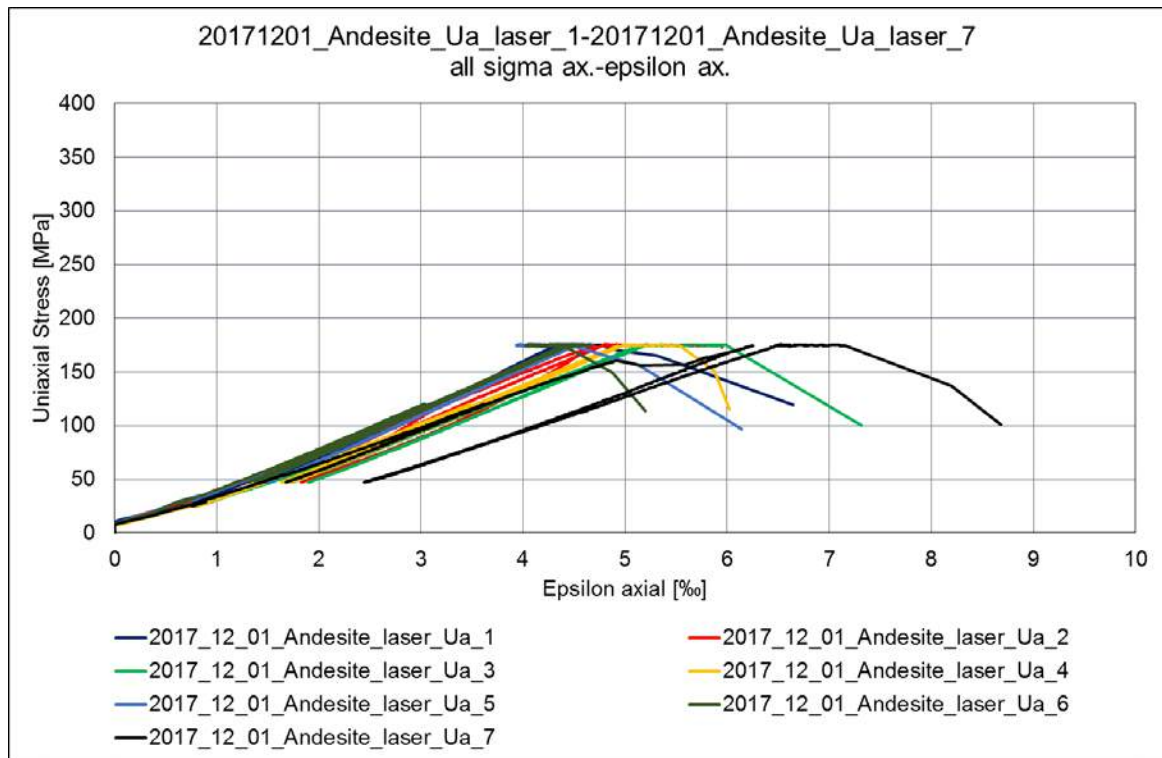


Figure 54: Relationship between uniaxial compressive stress and axial strain on andesite under laser radiation on the mantle of the sample

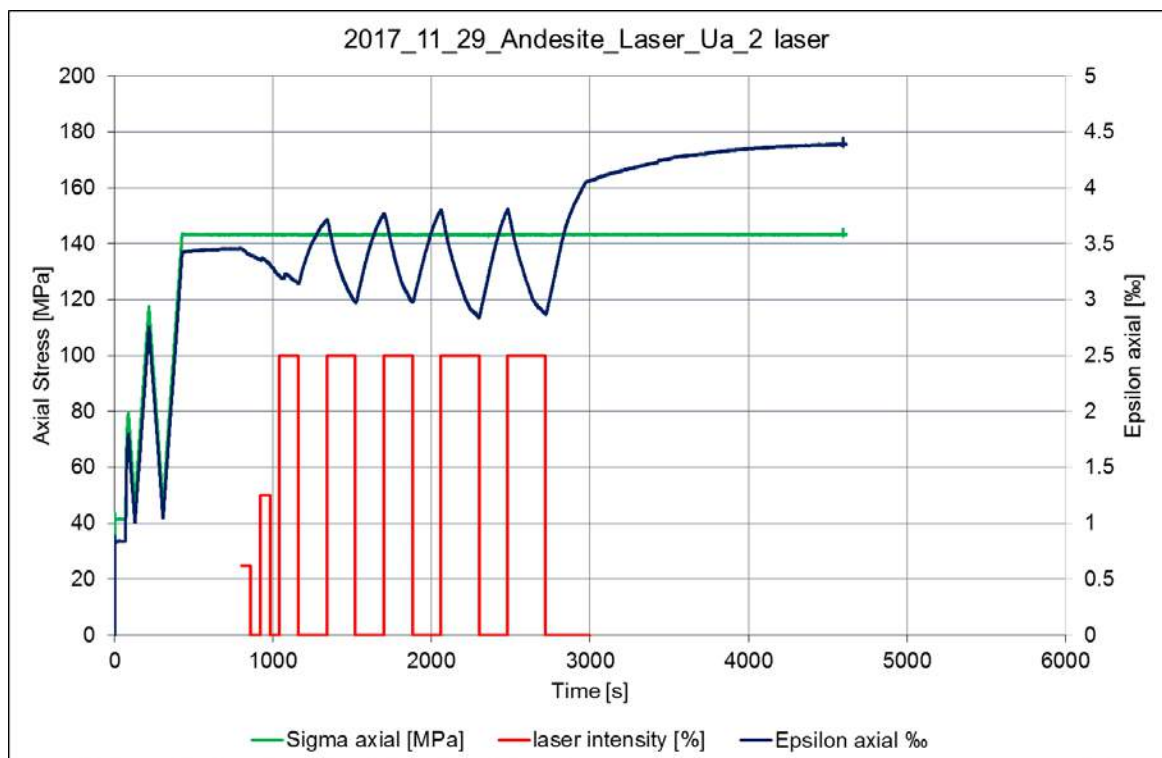


Figure 55: Relationship between uniaxial compressive stress and time as well as axial strain and time on andesite under laser radiation on the mantle of the sample

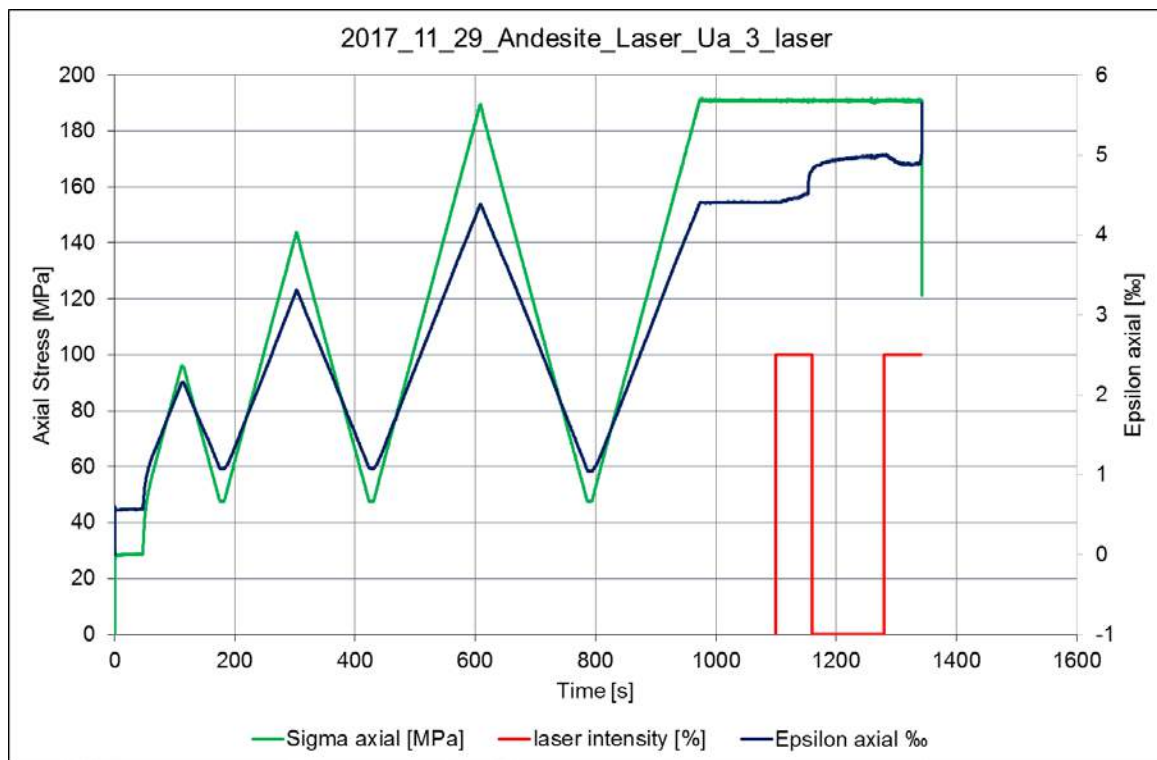


Figure 56: Relationship between uniaxial compressive stress and time as well as axial strain and time on andesite under laser radiation on the mantle of the sample

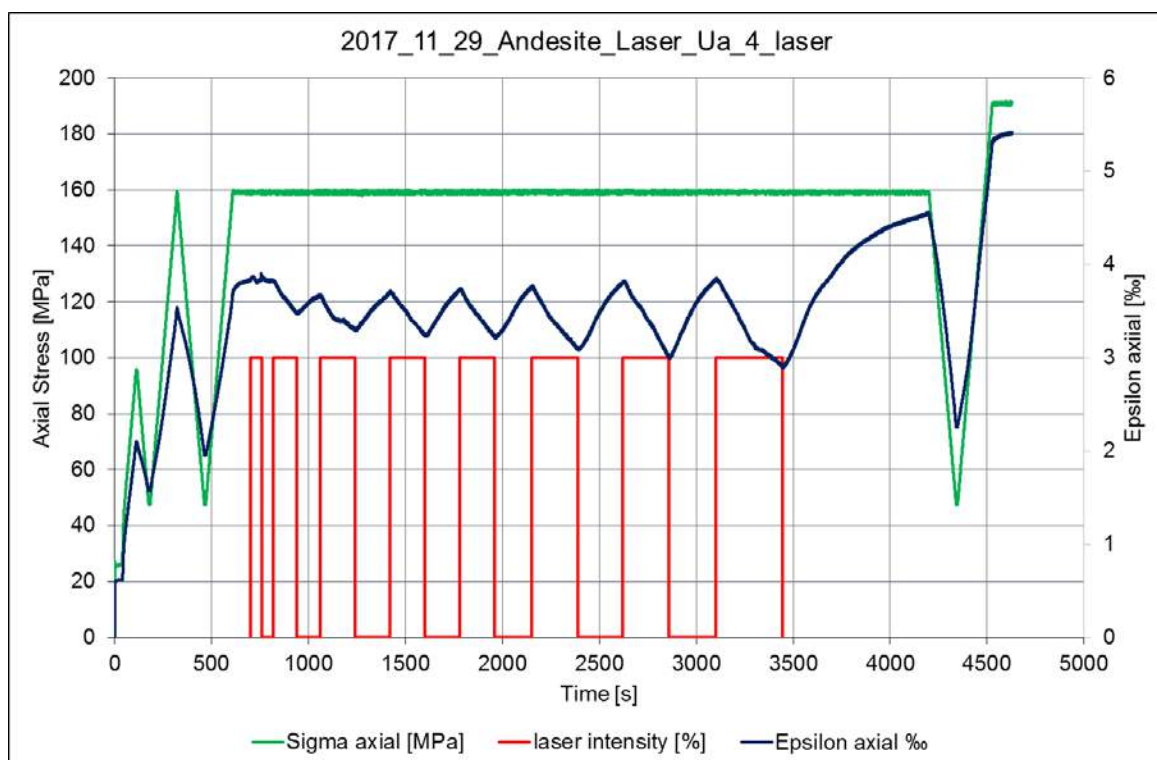


Figure 57: Relationship between uniaxial compressive stress and time as well as axial strain and time on andesite under laser radiation on the mantle of the sample

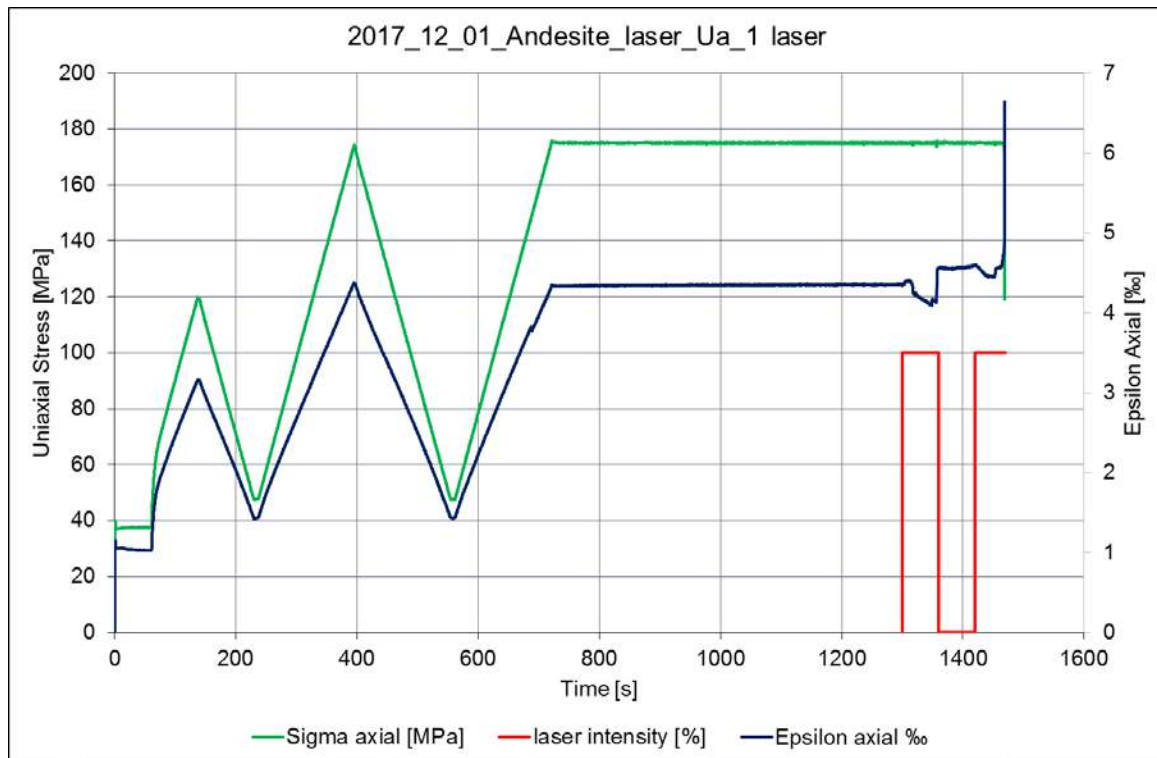


Figure 58: Relationship between uniaxial compressive stress and time as well as axial strain and time on andesite under laser radiation on the mantle of the sample

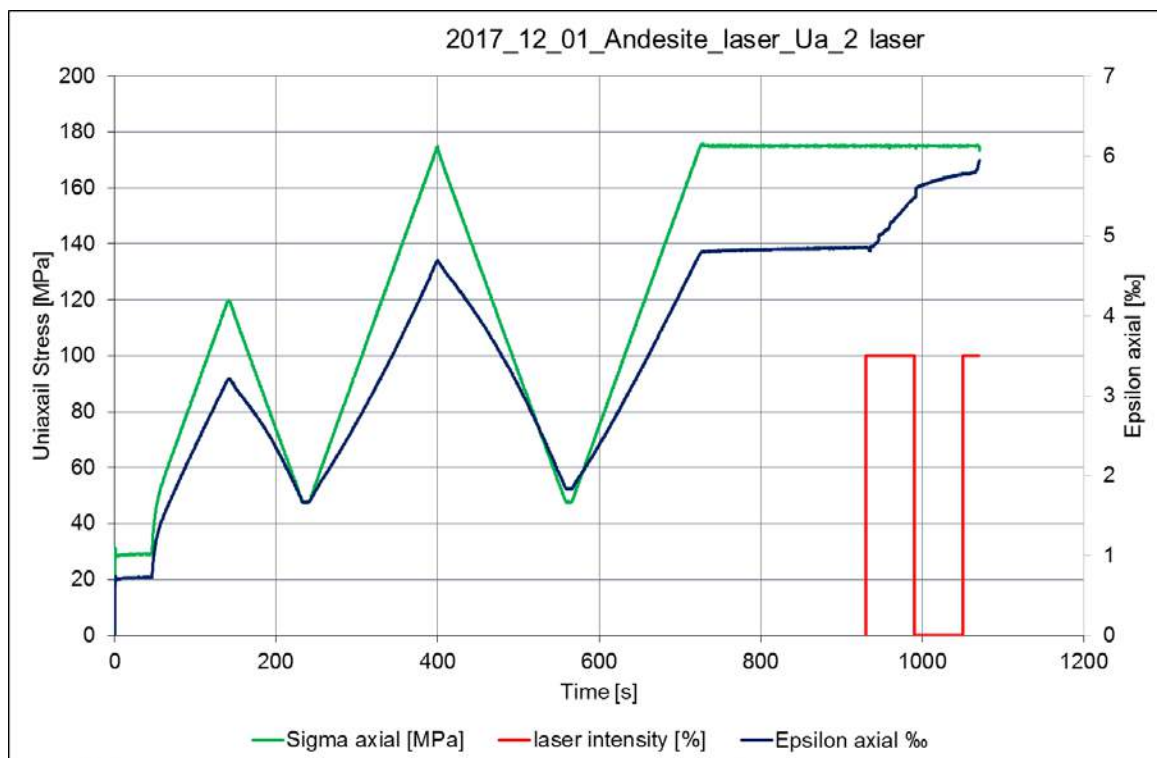


Figure 59: Relationship between uniaxial compressive stress and time as well as axial strain and time on andesite under laser radiation on the mantle of the sample

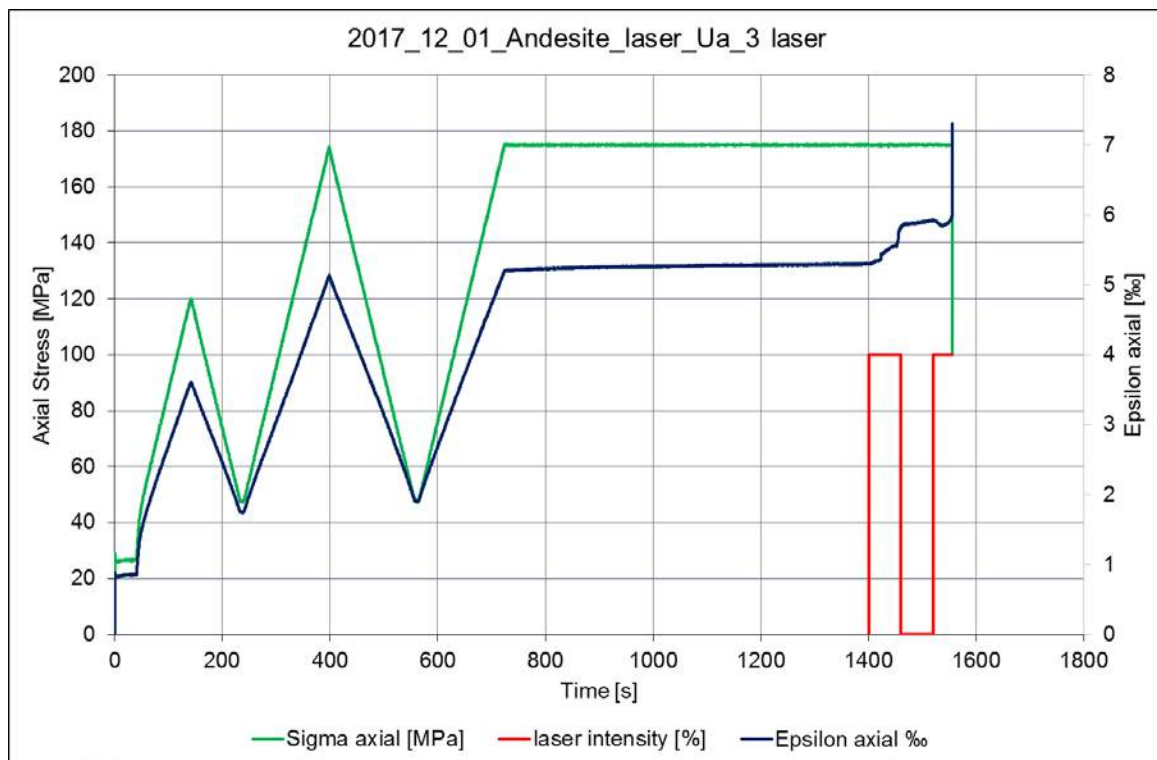


Figure 60: Relationship between uniaxial compressive stress and time as well as axial strain and time on andesite under laser radiation on the mantle of the sample

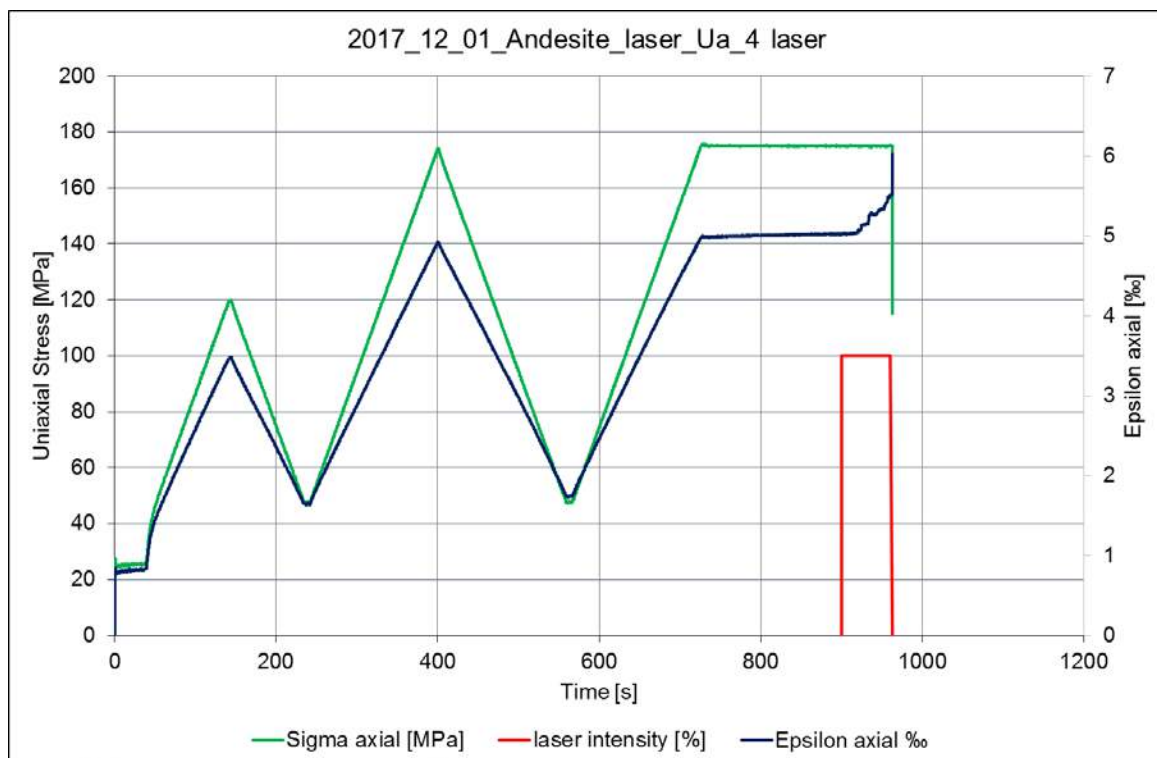


Figure 61: Relationship between uniaxial compressive stress and time as well as axial strain and time on andesite under laser radiation on the mantle of the sample

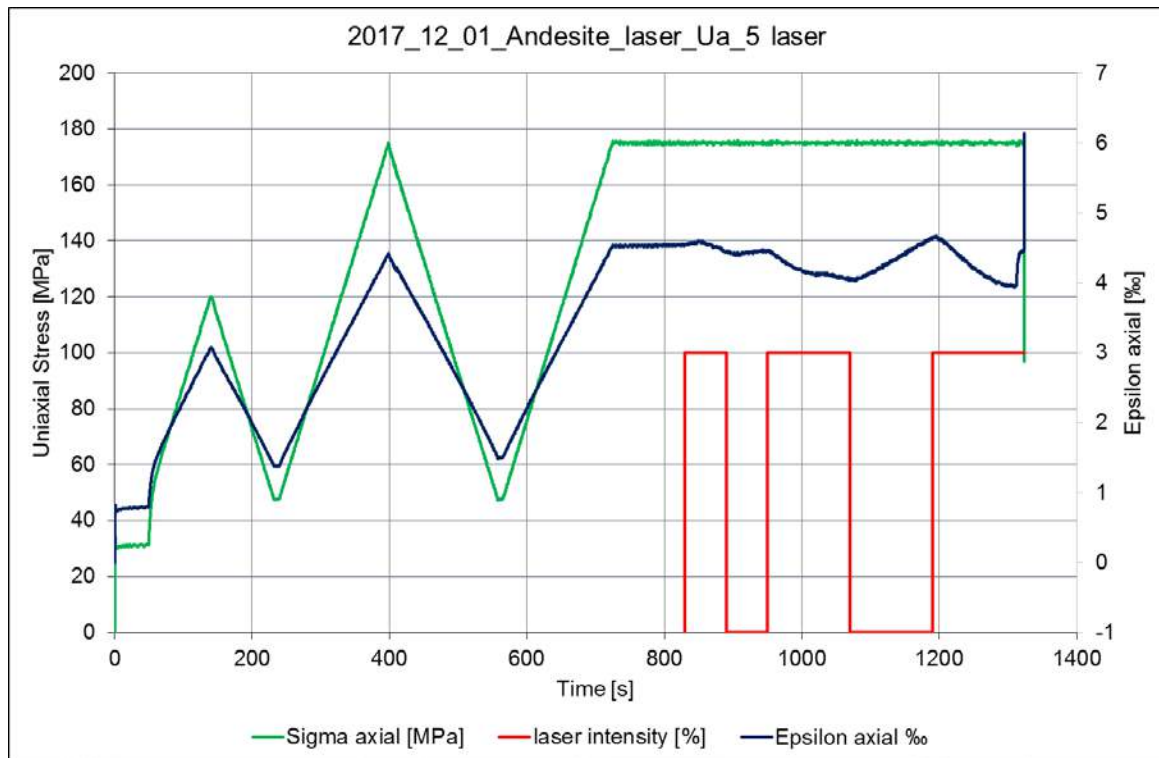


Figure 62: Relationship between uniaxial compressive stress and time as well as axial strain and time on andesite under laser radiation on the mantle of the sample

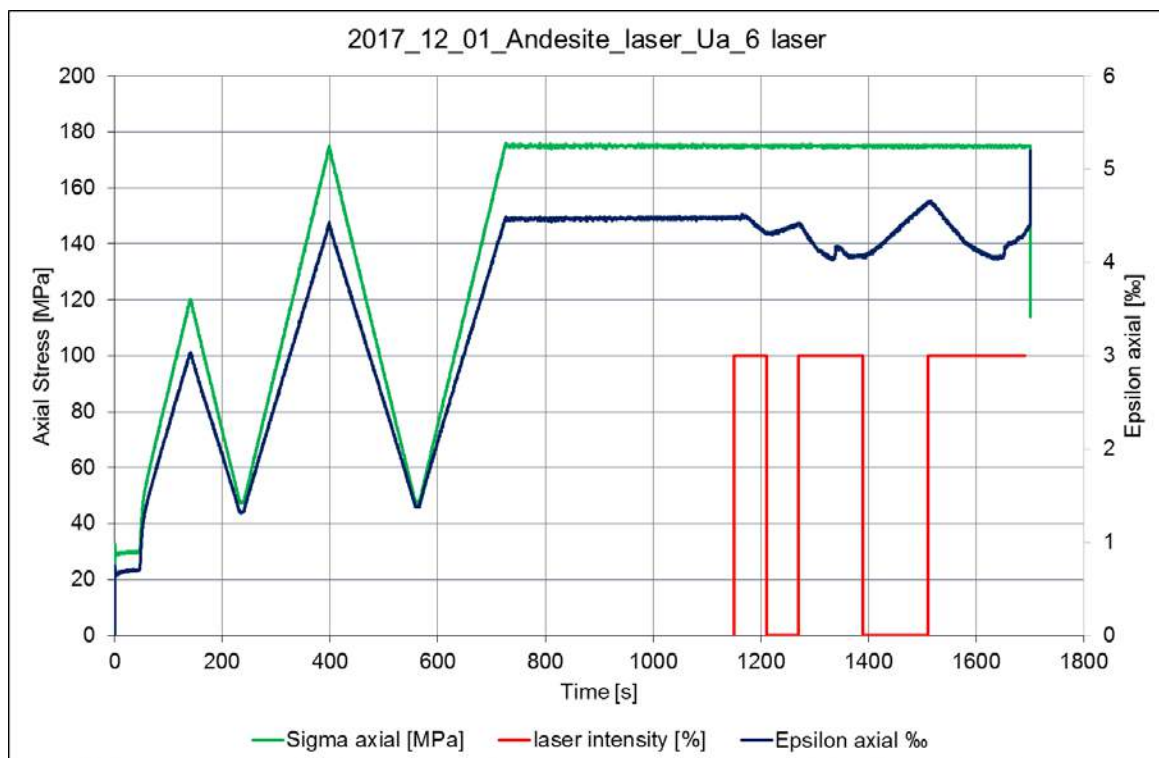


Figure 63: Relationship between uniaxial compressive stress and time as well as axial strain and time on andesite under laser radiation on the mantle of the sample

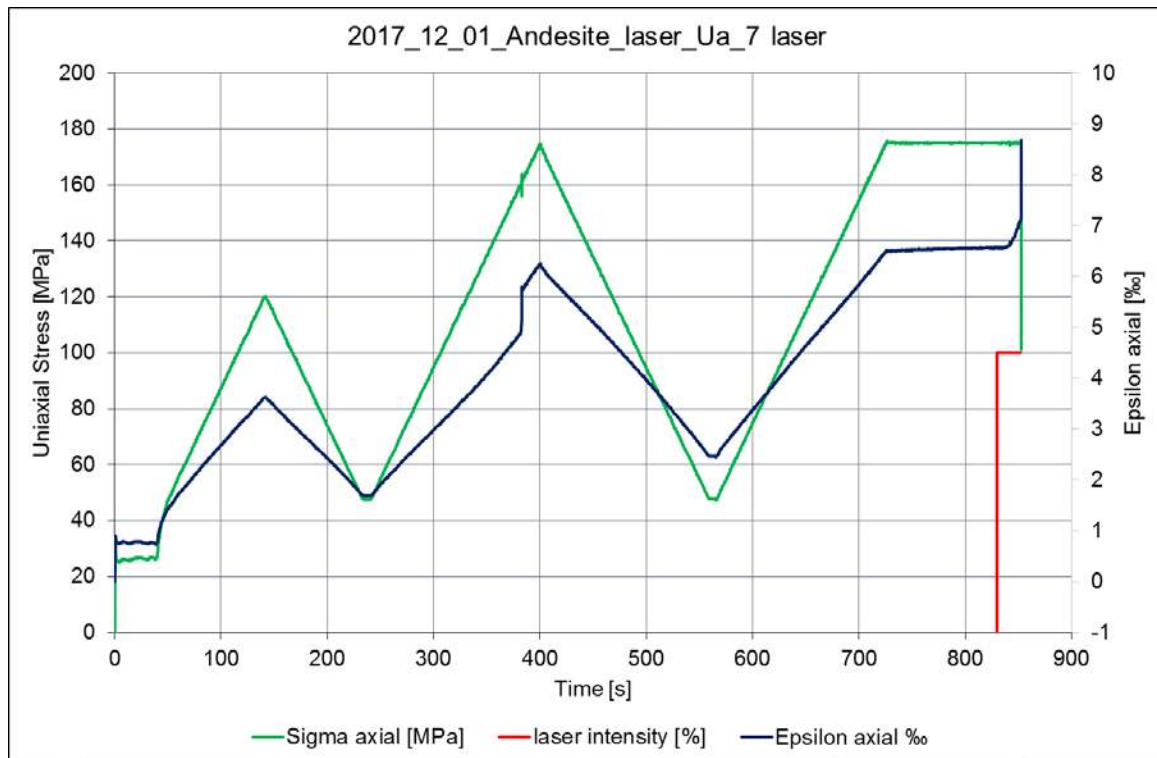


Figure 64: Relationship between uniaxial compressive stress and time as well as axial strain and time on andesite under laser radiation on the mantle of the sample

5.8. Results of granite tests

The uniaxial compressive strength of the investigated granite was 169 MPa (Table 13). The Young's modulus was 43 GPa and the modulus ratio was 253 (Table 13 and Figure 65).

Table 13: Results of uniaxial compressive strength tests on granite without laser

	Density [kg/m ³]	Uniaxial compressive strength (σ_c) [MPa]	Young modulus E [GPa]	MR (E/σ_c)
20171207_Granite_ua_1	2789	168.9	42.7	253

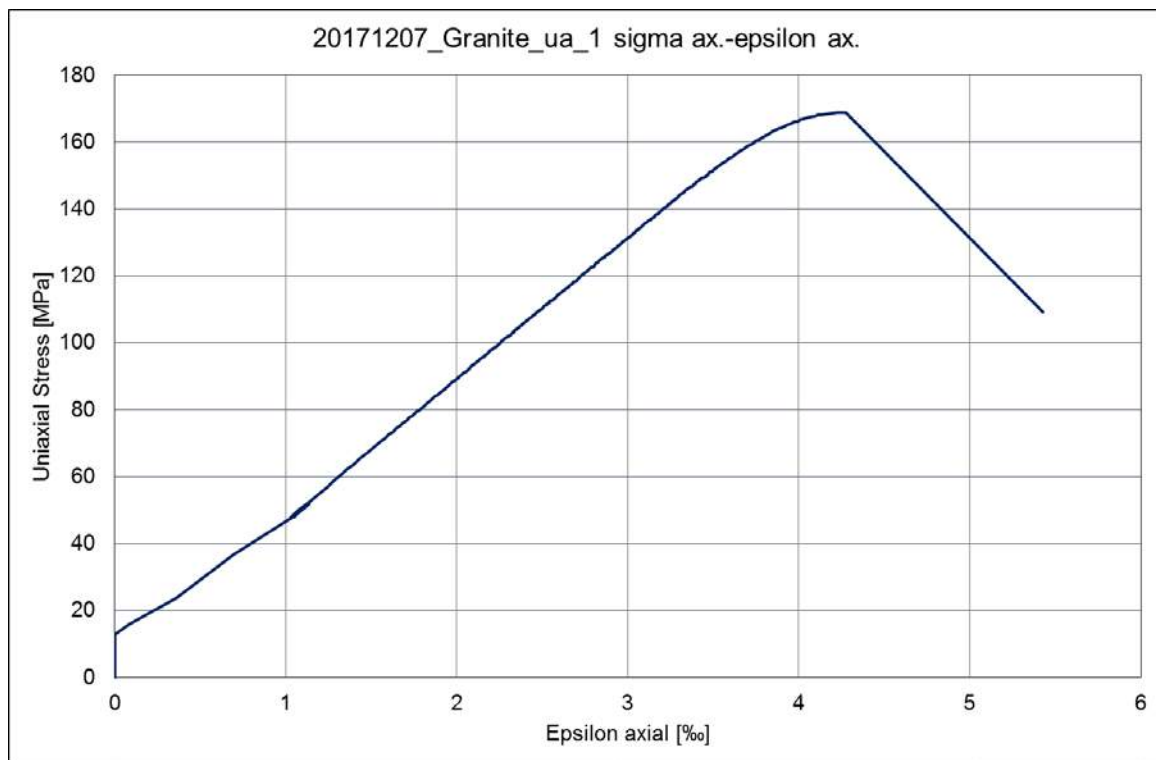


Figure 65: Relationship between uniaxial compressive stress and axial strain on granite

5.9. Results of uniaxial compressive strength tests on granite with laser

In the case of the uniaxial compressive strength test the focus of the laser beam was on the mantle of the samples at half the height of the samples. The laser distance was 2cm from the surface of the sample. During the tests the sample was loaded up to an adjusted constant load and during this constant load the mantle of the sample was radiated with laser (Figure 66-69). The value of the adjusted constant load was 120 MPa (Table 14 and Figure 66), this is the 70% of the uniaxial compressive strength value of the with laser not loaded granite (Table 13). In every case the sample was broken rapidly during the heat load. During the laser heat load the sample axial strain was increased, the sample was smaller in the direction of the uniaxial load (Figure 57, Figure 69).

Table 14: Results of uniaxial compressive strength tests on granite under laser radiation

	Density [kg/m ³]	Uniaxial compressive strength (σ_c) [MPa]	Young modulus E [GPa]	MR (E/σ_c)
20171207_Granite_laser_ua_2	2783	119.8	43.5	363
20171207_Granite_laser_ua_3	2789.76	120.0	41.4	345
average	2786	120	42	354
standard deviation	3.6	0.1	1.0	8.9

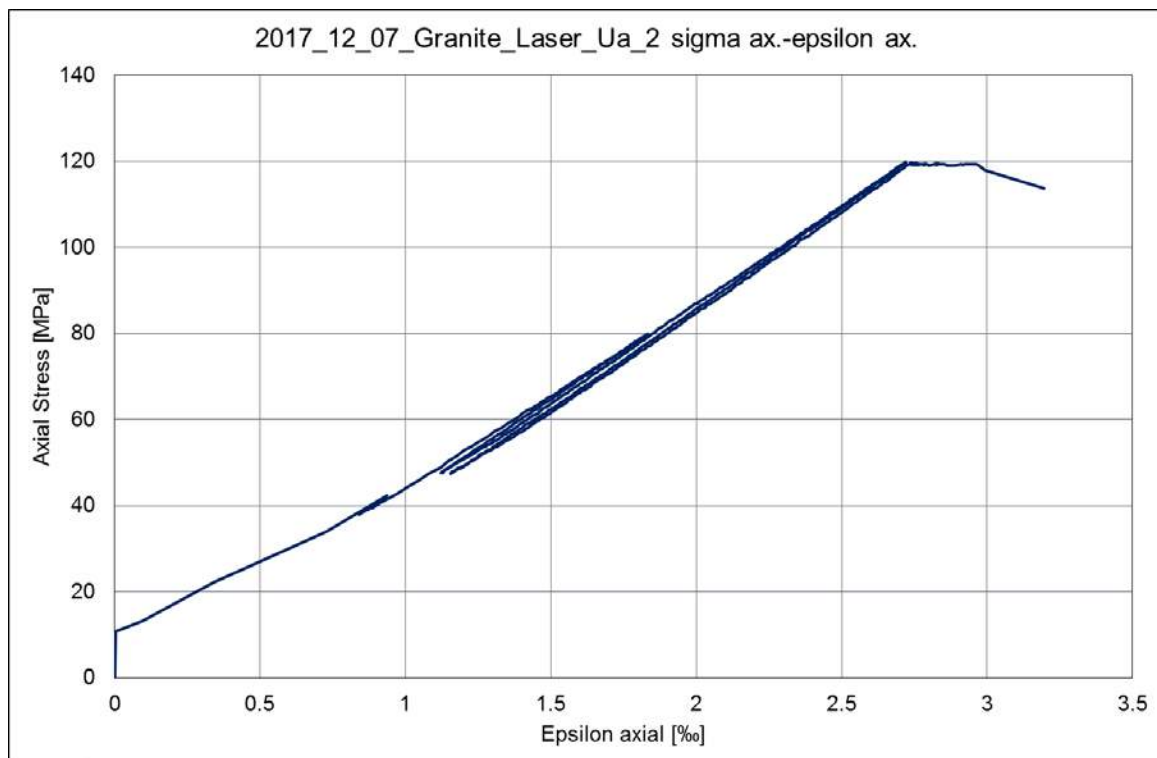


Figure 66: Relationship between uniaxial compressive stress and axial strain on granite

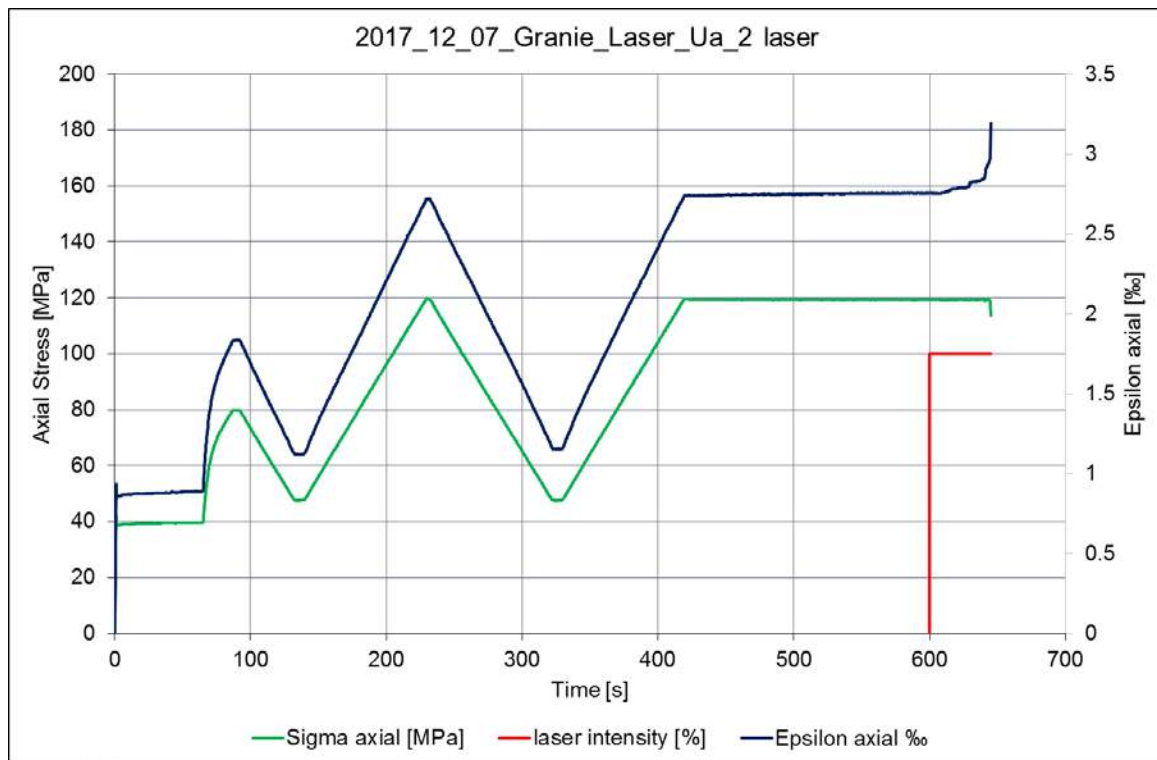


Figure 67: Relationship between uniaxial compressive stress and time as well as axial strain and time on granite under laser radiation on the mantle of the sample

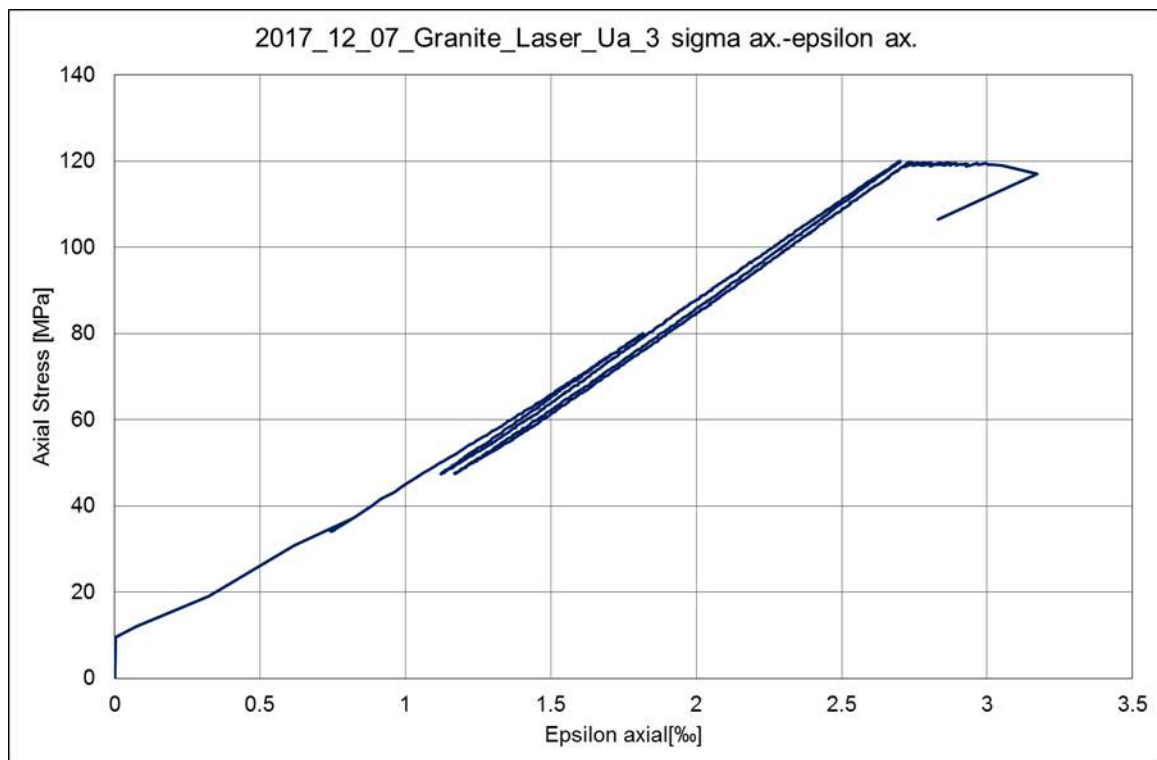


Figure 68: Relationship between uniaxial compressive stress and axial strain on granite

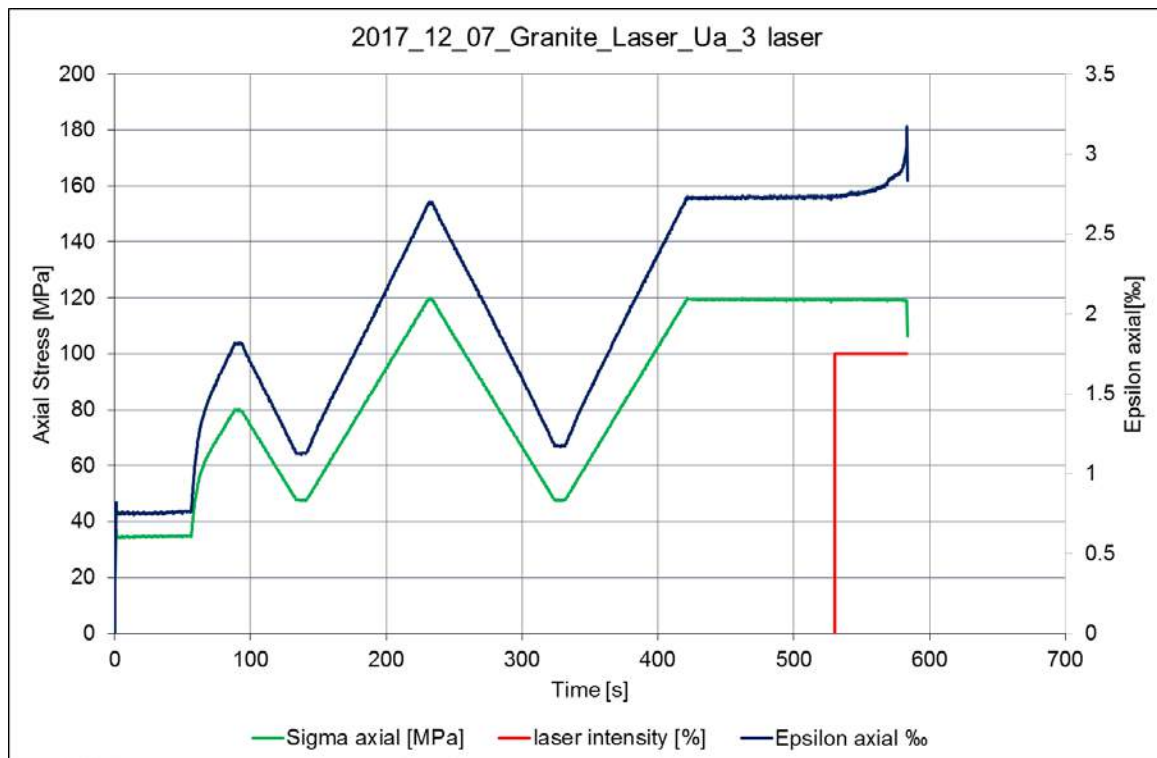


Figure 69: Relationship between uniaxial compressive stress and time as well as axial strain and time on granite under laser radiation on the mantle of the sample

5.10. Results of the indirect tensile strength test on granite with laser radiation

In the case of the indirect tensile strength test the focus of the laser beam was either on the base or on the mantle of the samples. The laser distance was 2 cm from the surface of the sample. During the tests the sample was loaded up to an adjusted constant load and during this constant load either the base or the mantle of the sample was radiated with laser (Figure 70-73). The value of the adjusted constant load was between 4.3 and 6.4 MPa (Table 15 and Figure 70). In every case the sample was broken quickly after the start of the laser radiation. During the laser heat load the lateral strain significantly increased (Figure 70-73) which signals the formation and spread of micro cracks in the rock structure.

Table 15: Results of indirect tensile strength tests on granite under laser radiation

	Density [kg/m ³]	Tensile strength σ_t [MPa]	Laser distance	Laser focus place
20171207_Granit_Laser_Br_4	2788	6.4	2 cm	mantle
20171207_Granit_Laser_Br_5	2782	4.3	2 cm	mantle
20171207_Granit_Laser_Br_6	2782	6.4	2 cm	base
average	2784	5.7		
standard deviation	3.0	1.0		

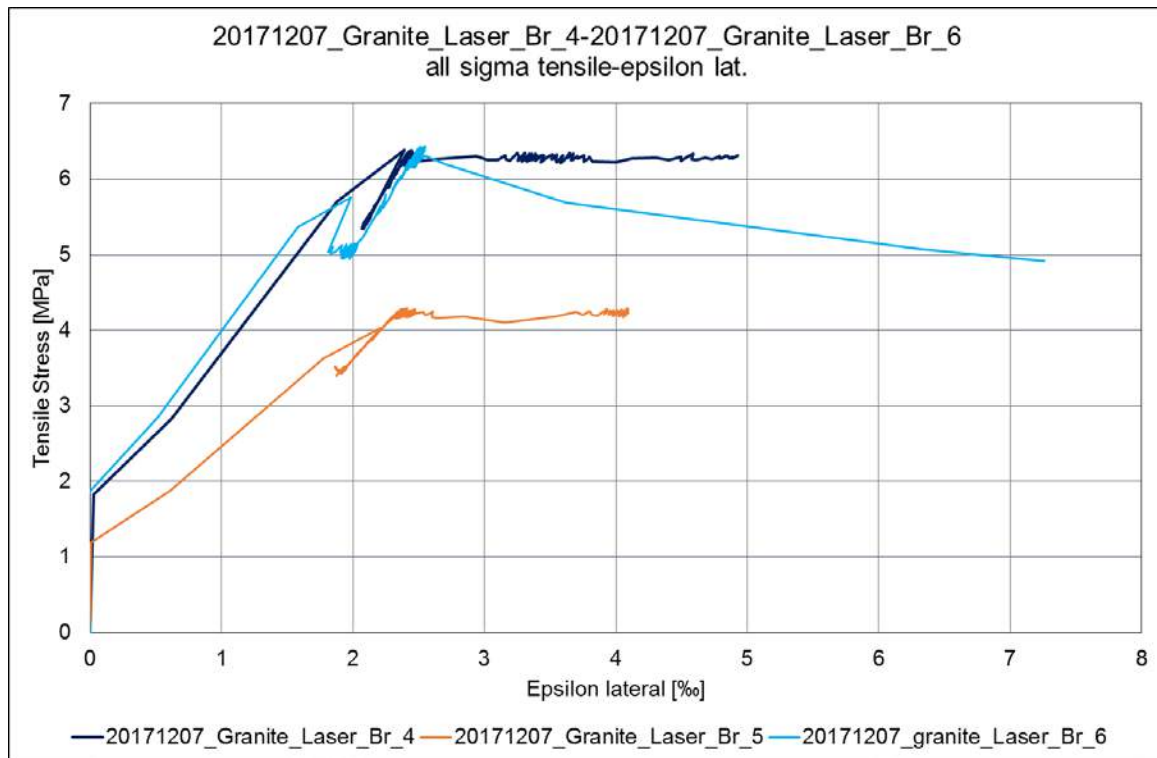


Figure 70: Relationship between tensile stress and lateral strain on granite under laser radiation

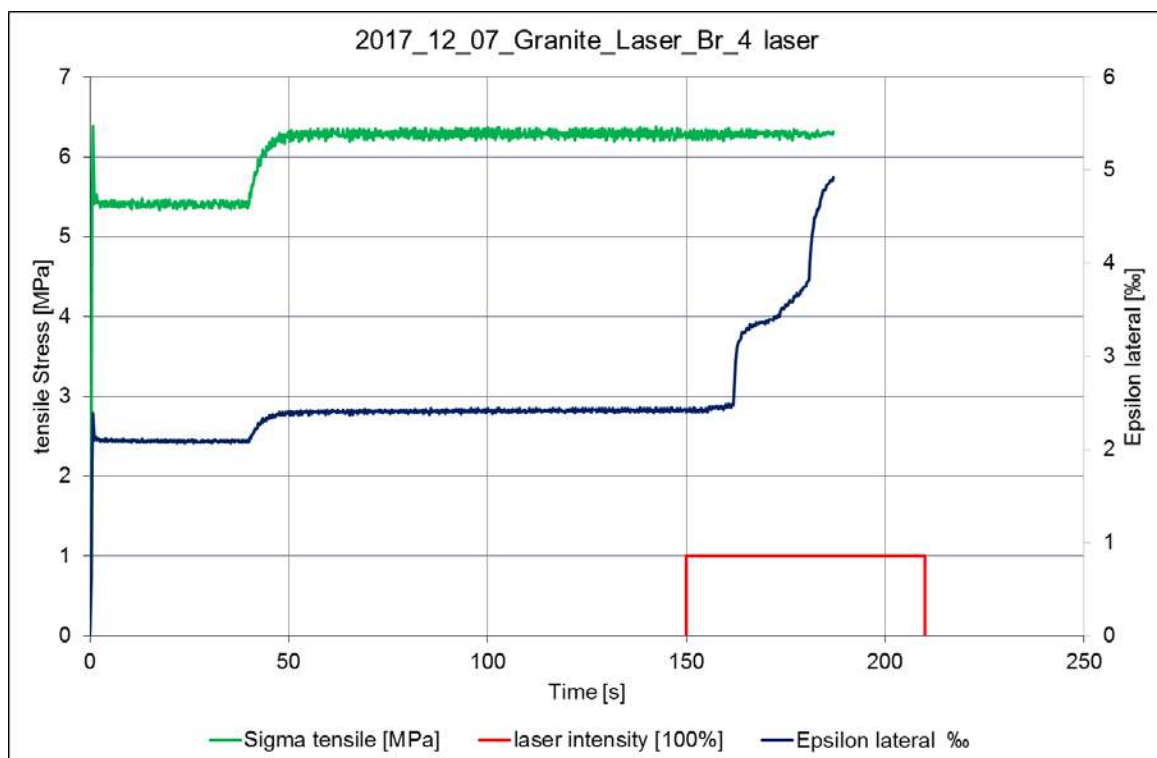


Figure 71: Relationship between tensile stress and time as well as lateral strain and time on granite under laser radiation on the base surface of the sample

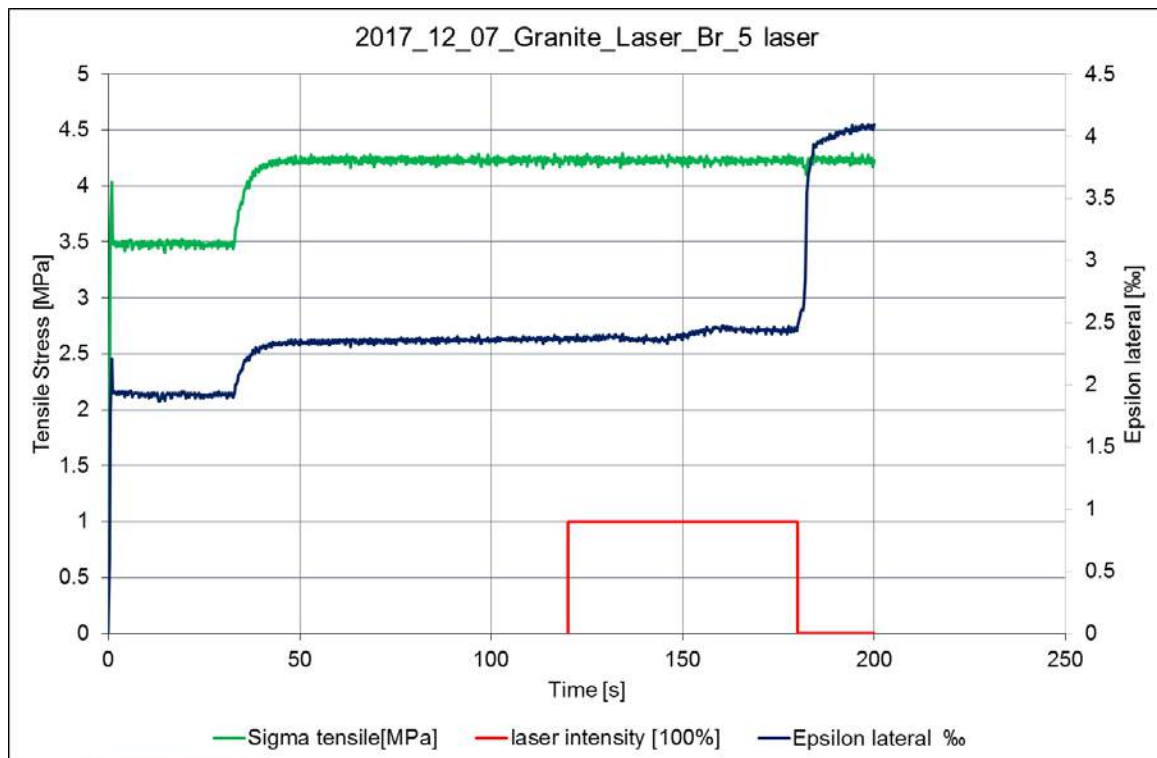


Figure 72: Relationship between tensile stress and time as well as lateral strain and time on granite under laser radiation on the base surface of the sample

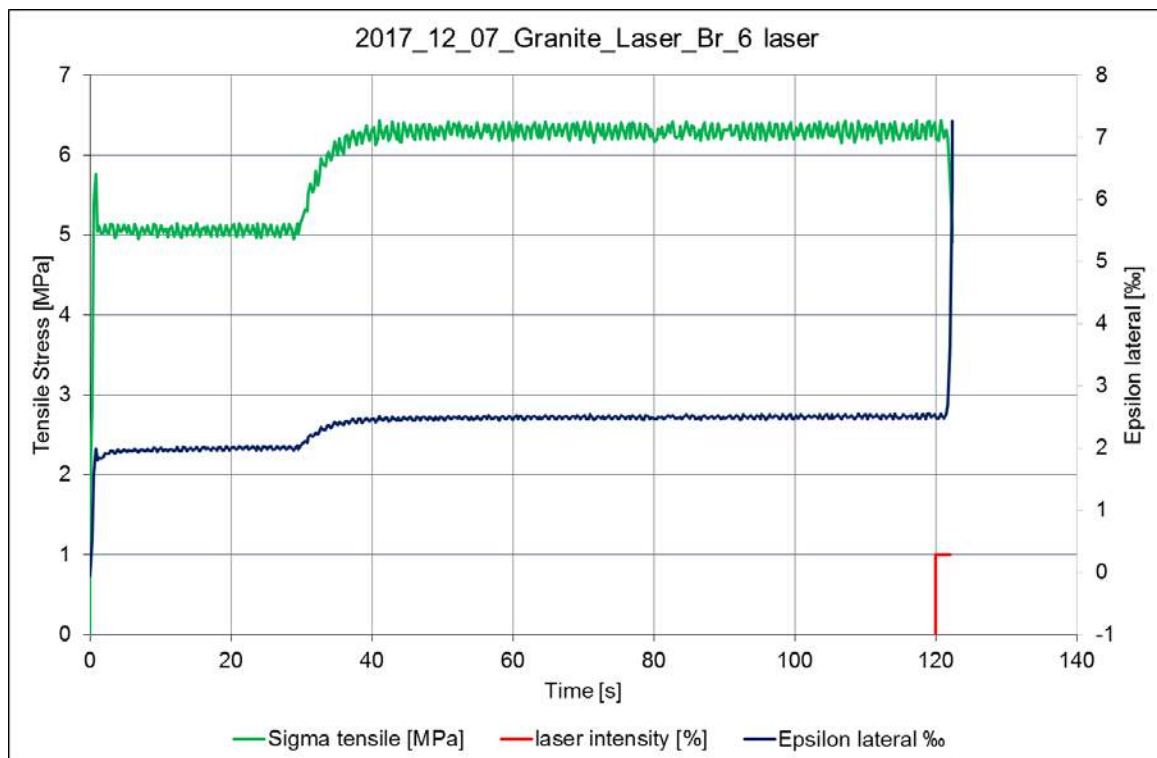


Figure 73: Relationship between tensile stress and time as well as lateral strain and time on granite under laser radiation on the base surface of the sample

5.11. Conclusions

Using laser shock during destructive rock mechanical tests, it can be seen, that rock failure can occur at lower stress levels. This phenomenon was measured better at Brazilian (indirect) tensile tests than uniaxial compressive tests. It is well known that the failure of the rock is due to the tensile stress of the micro cracks. It means that the laser shock (applied during tensile test) influences the instable crack propagation of the micro cracks. If the downhole laser will be developed this technology could be useful to reduce the pressure need of hydrofracturing or hydroshearing.

Using the classical failure theorems (ie. Mohr-Coulomb or Hoek-Brown failure criteria) the tensile strength of the rock decreases more than the uniaxial compressive strength, ie. the ratio of the two values should be increased (namely: Brince number, $R = \sigma_c / \sigma_t$). Increases in the Brince number (R), causes the rigidity of the intact rock to increase too (Vásárhelyi et al., 2016).

The rigid (brittle) rock can be broken up into several smaller pieces, and new ruptures can be developed according to earlier research results (Nagy et al., 2013).

Unfortunately, the tests results did not make determining the exact changes (increase) in brittleness possible – future tests will be needed for this to be measured and calculated.

6. Fluid flow experiments with different levels of artificial enhancement in pressure chamber

6.1. Aim

The goal of the leaching tests in the CHPM project is to have an idea and an optimal composition of leaching fluid, which is able to most effectively bring certain metals from the underground to the surface in solution. This chapter includes complementary experiments to Task 2.2 Metal content mobilisation using mild leaching (led by NERC-BGS). In this work a flow-through pipe reactor was used to most accurately summon the natural properties of a typical geothermal reservoir at 2.5 km - 3 km depth. In this reactor a continuous fluid flow was maintained and samples were collected after the fluid-rock interaction.

6.2. Methodology – device built – explanation

The methodology used, to reach the goal of this chapter, included the operation of a customized device to create the physical properties of an underground reservoir on a laboratory scale (Figure 74). Therefore, a high pressure high temperature device was used and operated at approximately 250°C temperature and 250 bar pressure at the same time. These parameters correspond to 2.5 km depth in an average geothermal field. In the pipe reactor a sample (grinded to maximum 250 µm) of approximately 150 gramm was placed and a flow rate of 0.1 ml/min to 5 ml/min was maintained by a HPLC pump.

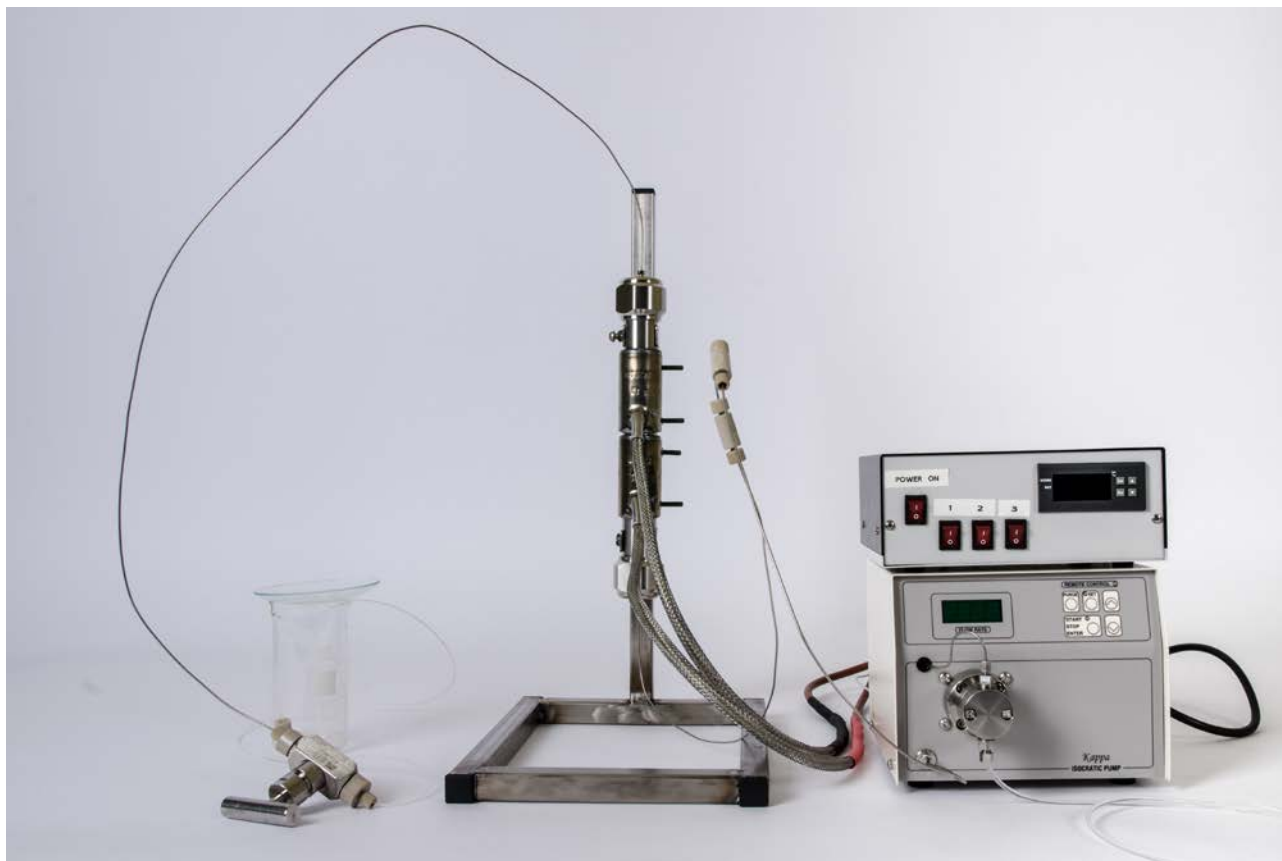


Figure 74: The experimental setup for flow-through leaching tests

6.3. Samples

Investigated samples were discussed in detail in D1.3, Table 16 shows a short summary of the relevant samples. In D1.3 these, and many more were measured and described systematically, during our laboratory experiments a grinded version of the following ones were into the pipe reactor.

Table 16: Samples investigated in leaching measurements

Sample	Origin	Type	Characteristics
CHPM3	HU Gyöngyösoroszi	Vein	A fragment of a calcite vein with base metal sulphides.
CHPM4	HU Rudabánya	MVT	Banded baritic lead ore from a metasomatic deposit hosted by limestone; galena grains in dark bands can be recognized with coarse grained white barite lenses and fine grained limonitic matrix.
CHPM 5	HU Recsk	Porphyry	Represents an intrusion related porphyry copper deposit; a breccia with sulphide matrix and veins
CHPM 6	HU Recsk	Skarn	Originates from the same site as Sample 5. It is a massive pyrite-chalcopyrite-iron oxide ore from the skarn zone.
CHPM 12	BMMB Masca-Cacova Ierii	Skarn	Represents a magnetite deposit also enriched in sulphides, with visible chalcopyrite.
CHPM 14	BMMB Masca-Baisoara	Skarn	Represents a magnetite deposit also enriched in sulphides, with visible chalcopyrite.
CHPM 29	Portugal, Cotovio CTO8001, 1000 m	Borra de Vinho	Green siliceous shales, between purple shales
CHPM 32	Portugal, Cotovio CTO8001, 1089 m	Grandaços	Grey dark shales. S0 defined by fine silt layers
CHPM 39	Portugal, Cotovio CTO8001, 1504,8 m	Upper volcanics	Acid volcanics - clastic facies
CHPM 40	Portugal, Cotovio CTO8001, 1557,5 m	Upper volcanics	Acid volcanics - clastic facies
CHPM 42	Portugal, Cotovio CTO8001, 1661,5 m	Upper volcanics	Acid volcanics - clastic facies
CHPM 43	Portugal, Cotovio CTO8001, 1678 m	Upper volcanics	Whyte acid volcanics - clastic facies, granular texture

As it is shown in Table 16, half of the examined samples were originated from a drill hole in Portugal. The targets of the drilling were deep geological formations (990 – 1887 m). To have a better understanding of the geological quality of samples, Figure 75 represents the cross-section of the drilling which provided some of the samples. The sampling program was led by João Xavier Matos and Elsa Ramalho (LNEG) in December 2016, at Somincor/Lundin Mining Lombador, Portugal. The exact location of the drillhole is (WGS 84): 59° 56' 54" N, 41° 56' 75" E.

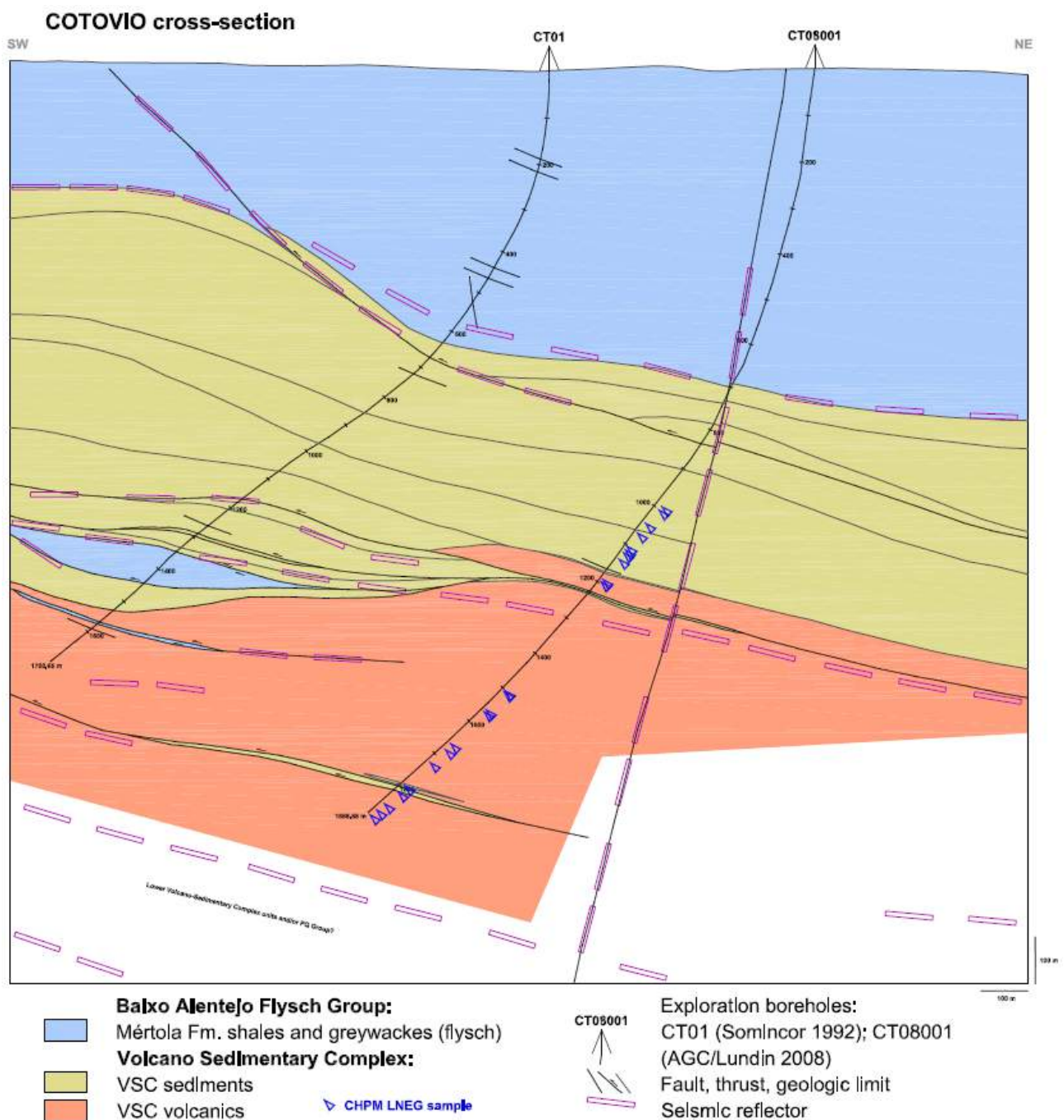


Figure 75: Cross-section of CTO8001 drilling, on the figure blue arrow heads mark the original location of the samples which were used in the laboratory (Courtesy of LNEG)

All samples above were leached with deionized water and with 0.1M acetic acid to compare the efficiency of mobilisation.

Table 17: A summarizing table of circumstances during each measurement

Sample number	Temperature (°C)	Pressure minimum (bar)	Pressure maximum (bar)	Residence time (min)	Comments
CHPM3.1	200	220	230	35	
CHPM3.2	200	229	240	35	
CHPM3.3	200	231	242	34	
CHPM3.1A	250	240	252	58	A lot of bubbles are visible
CHPM3.2A	250	240	252	52	A lot of bubbles are visible
CHPM4.1	200	225	290	36	A few small bubbles are visible
CHPM4.2	200	250	257	48	Pump stopped and pressure dropped during measurement
CHPM4.3	200	250	285	35	
CHPM4.4	200	250	280	6	Just washing out the equipment to see if any crystal forming in this
CHPM4.1A	250	250	260	33	
CHPM4.2A	250	250	260	48	Opening and closing the valve
CHPM4.3A	250	250	260	51	Really bubbly
CHPM4.4A	250	250	260		This is not good, had to open the valve
CHPM5.1	200	220	240	25	Bubbly
CHPM5.2	200	270	283	37	Sample destroyed during transportat
CHPM5.3	200	283	293	37	No bubbles here
CHPM5.1A	250	250	250	30	
CHPM5.2A	250	250	250	38	
CHPM5.3A	250	250	250	46	
CHPM5.4A	250	250	250	54	
CHPM6.1	200	200	225	30	The collected water sample mells like dust or sand
CHPM6.2	200	225	250	34	
CHPM6.3	200	260	270	37	
CHPM6.4	200	260	270	37	Smells like soil, the sample is a bit opal
CHPM6.1A	250	250	250	29	
CHPM6.2A	250	250	250	31	
CHPM6.3A	250	250	250	32	
CHPM6.4A	250	250	250	32	
CHPM12.1	200	230	240	45	
CHPM12.2	200	240	248	52	
CHPM12.3	200	273	297	38	
CHPM12.1A	250	270	270	27	
CHPM12.2A	250	270	270	56	Pump stopped and pressure dropped during measurement
CHPM12.3A	250	270	270	24	
CHPM12.4A	250	270	270	26	Smells like sulphur, strange color
CHPM14.1	200	221	230	35	Sample destroyed during transportat
CHPM14.2	200	247	255	38	

Sample number	Temperature (°C)	Pressure minimum (bar)	Pressure maximum (bar)	Residence time (min)	Comments
CHPM14.3	200	257	268	40	
CHPM14.1A	250	230	238	30	
CHPM14.2A	250	238	250	30	
CHPM14.3A	250	250	250	30	
CHPM14.4A	250	250	250	44	
CHPM29.1	200	220	230	30	Powdered sample smells like sulphur
CHPM29.2	200	250	270	30	Powdered sample smells like sulphur
CHPM29.3	200	236	250	30	Powdered sample smells like sulphur
CHPM29.4	200	250	250	30	Powdered sample smells like sulphur
CHPM29.1A	250	250	250	38	
CHPM29.2A	250	250	250	45	
CHPM32.1	200	199	256	29	
CHPM32.2	200	200	200	31	Pressure dropped during experiment
CHPM32.3	200	200	260	30	
CHPM32.4	200	260	280	38	Experiment stopped after 20 ml
CHPM32.1A	250	198	200	32	Leaking
CHPM32.2A	250	200	250	33	
CHPM39.1	200	250	260	64	Clayey smell
CHPM39.2	200	250	260	37	Clayey smell
CHPM39.3	200	250	260	15	Clayey smell
CHPM39.4	200	250	260	30	Clayey smell
CHPM39.1A	250	225	250	48	
CHPM39.2A	250	250	260	34	Smells like black powder
CHPM40.1	200	244	255	41	Pump stopped and pressure dropped during measurement
CHPM40.2	200	250	250	30	
CHPM40.3	200	250	250	30	
CHPM40.4	200	250	250	30	
CHPM40.1A	250	210	218	30	
CHPM40.2A	250	218	250	36	
CHPM40.3A	250	250	260	30	
CHPM40.4A	250	284	297	47	
CHPM42.1	200	230	250	32	Smells like sulphur
CHPM42.2	200	240	260	35	
CHPM42.3	200	240	260	30	
CHPM42.4	200	240	260	30	
CHPM42.1A	250	190	250	37	
CHPM42.2A	250	250	250	35	
CHPM43.1	200	230	260	47	Smells a little like sulphur
CHPM43.2	200	250	260	54	Smells a little like sulphur
CHPM43.3	200	250	260	54	Smells a little like sulphur
CHPM43.4	200	250	260	46	Smells a little like sulphur
CHPM43.1A	250	214	250	35	

Sample number	Temperature (°C)	Pressure minimum (bar)	Pressure maximum (bar)	Residence time (min)	Comments
CHPM43.2A	250	250	250	34	

6.4. Results

All the samples were sent to chemical analysis to an accredited laboratory, for ICP-MS analysis. Surface and groundwater surveys are an effective means for exploration of remote and blind ore deposits. Analysis by ICP-MS provides the low detection limits needed to define background and anomalous levels of cations in natural water. For this analysis all water samples must have less than 0.1% total dissolved solids (TDS). Analysis of water geochemical parameters including pH, electrical conductivity, alkalinity, and anions provides the necessary parameters for complete characterization of water samples. Complete water characterization allows for the determination of not only the type of water (i.e., Ca-SO₄ or Na-Cl), but how the type of water relates to ore deposit marker elements. A detailed, thorough table of the analysis can be found in Appendix 11.3, in the following section processed data are visualized to understand the outcomes. Figure 76-82 shows spider plot of the elemental composition of the most abundant elements in each leachate. For comparability, the format of the graphs is the same as in D2.2 (report on metal content mobilisation using mild leaching). The units on each graph are in PPB, on a logarithmic axis. On the outside of each graph, the chemical symbol of the most interesting elements can be found, with the concentration value marked with green dot.

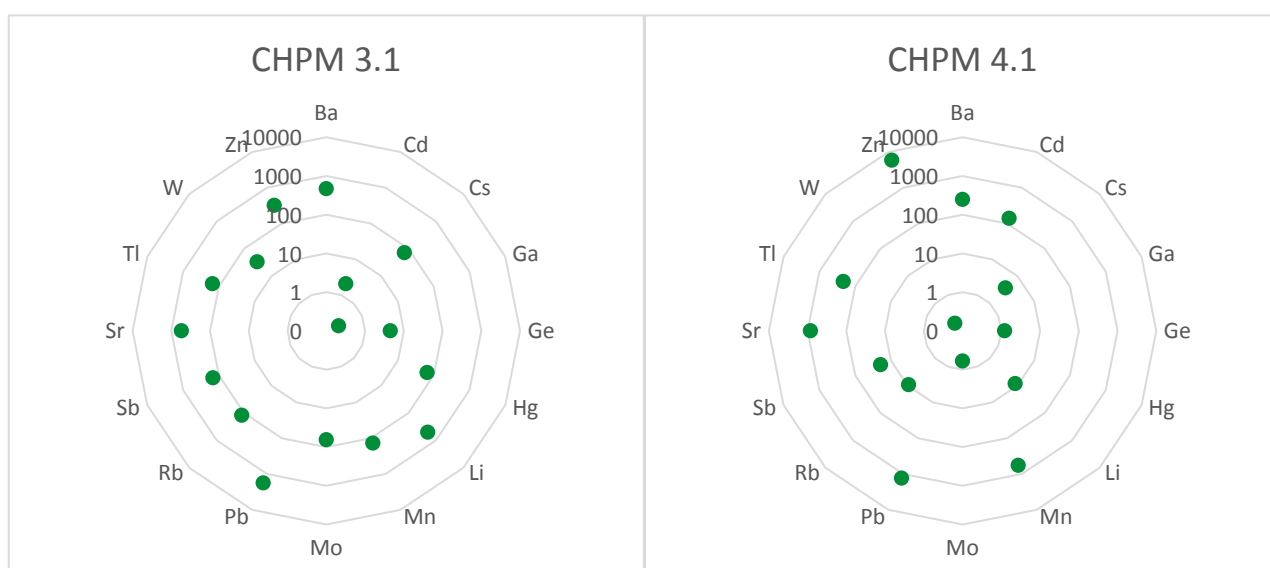


Figure 76: Chemical composition (ICP-MS) of samples CHPM3.1 and CHPM4.1

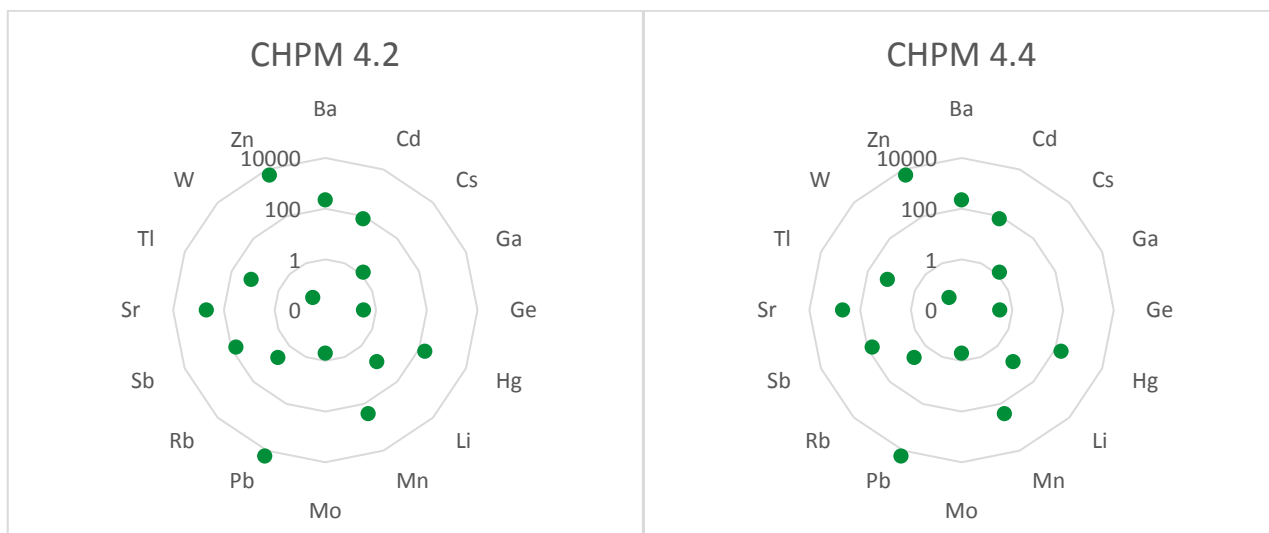


Figure 77: Chemical composition (ICP-MS) of samples CHPM4.2 and CHPM4.4



Figure 78: Chemical composition (ICP-MS) of samples CHPM5.1 and CHPM6.1

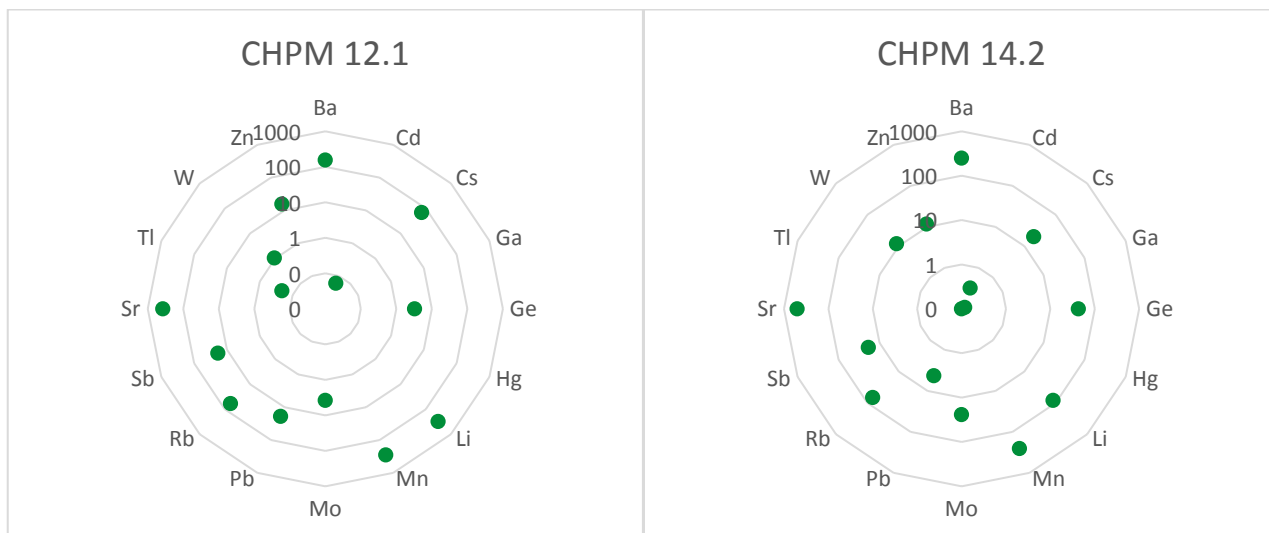


Figure 79: Chemical composition (ICP-MS) of samples CHPM12.1 and CHPM14.1

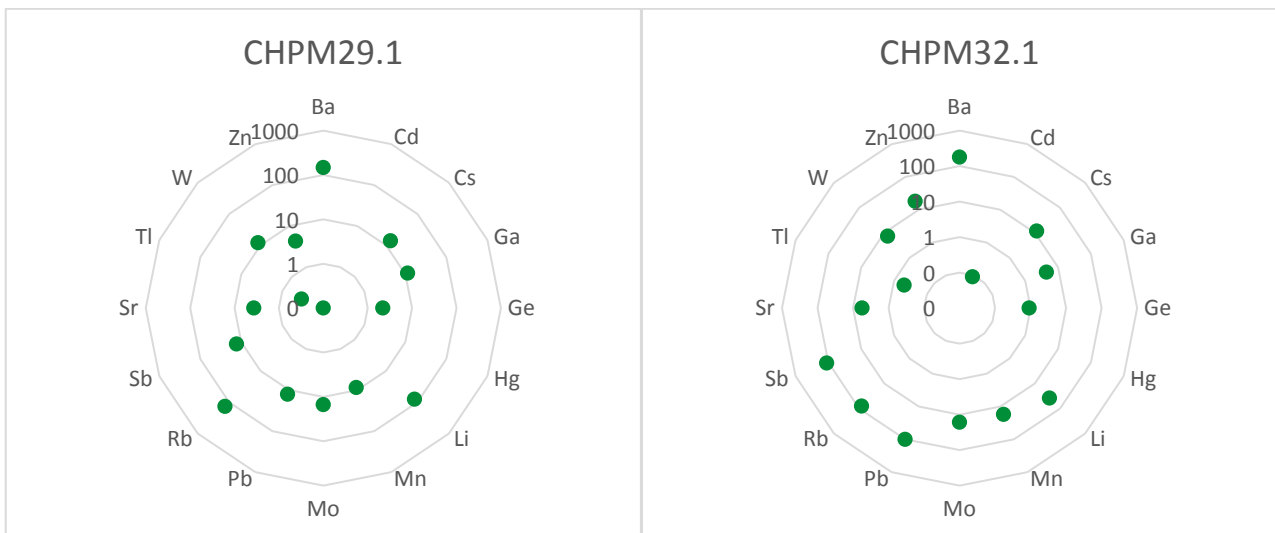


Figure 80: Chemical composition (ICP-MS) of samples CHPM29.1 and CHPM32.1

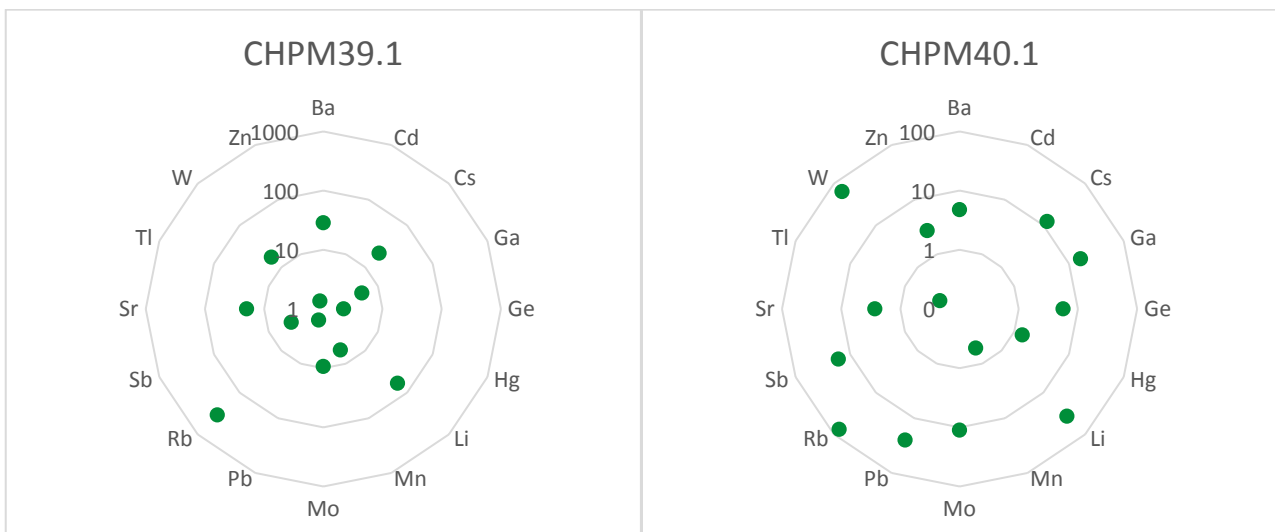


Figure 81: Chemical composition (ICP-MS) of samples CHPM39.1 and CHPM40.1

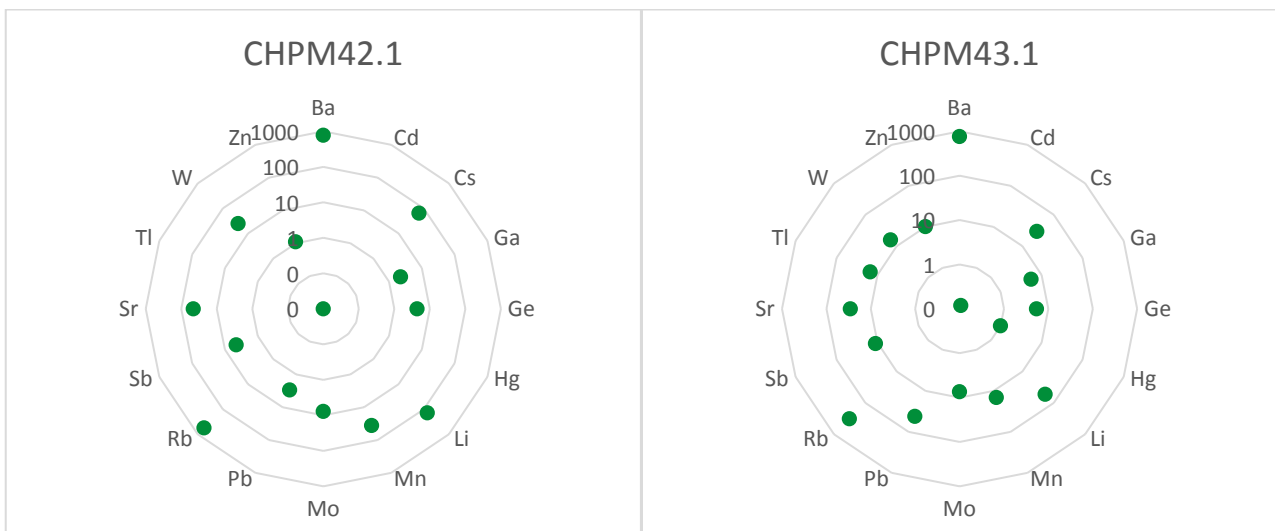


Figure 82: Chemical composition (ICP-MS) of samples CHPM42.1 and CHPM43.1

6.5. Discussion

It is important to note that the samples and results above are from rocks reacted with deionized water at the given temperature and pressure. Measurements were made, and samples were collected with 0.1 M acetic acid as well, however despite sending those samples to chemical analysis (ICP-MS) in November, the results of those analyses have not arrived as of now (2017. December 15). We have been informed that the reason for the delay was a logistical problem within the analysis company. Therefore, in this report the composition of leaching fluids, the comparison of rock and fluid composition and the composition of all the samples which originate from the reaction of rock and acetic acid, cannot be included. Those results and the conclusions from the measurements will be included in the work conducted under the framework of WP3.

6.6. Conclusion

The laboratory leaching tests were run at 200-250°C temperature under 250-300 bar pressure, which represents an average geothermal reservoir at 3 km depth. During the reaction in laboratory, there is some enhanced Pb release. However, compared to the experiments of NERC-BGS the concentration is lower. The reason for this is that the reaction time is different in the two types of experiments. A visible amount of Zn is also present in the leachate, which corroborates the enhanced dissolution progress. It is interesting that in the rock sample and CHPM3 sample there was no lithium found, however in the leachate the lithium content was the highest of all measurements. To be sure, the composition of the solid sample was measured with XRD, shown on Figure 83, however lithium still could not be found in the solid rock sample.

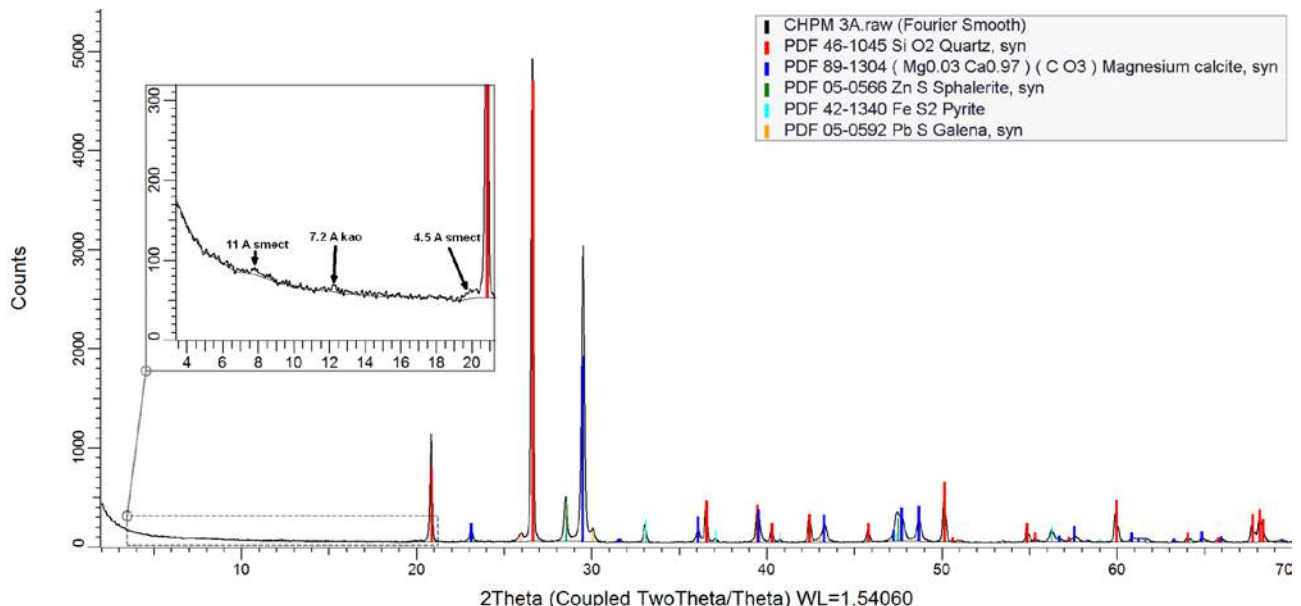


Figure 83: XRD diagram of CHPM3 sample

The reason behind this is that the lithium element is so small, it can “hide” in the crystal structure of other minerals thus avoiding detection. Also, in the laboratory tests significant Al and Si were found. This could be desirable in terms of opening flow paths, but if concentrations get too high there is an increased risk of precipitation of clay minerals, which could clog fractures and inhibit the fluid flow.

7. Three-dimensional stochastic fracture model

7.1. Introduction

Fracture systems play an essential role in fluid flow and heat transport processes in hard rock bodies. Over the last few decades (e.g., Maros et al., 2004, 2010), a detailed structural geological evaluation of the faults and fault systems in the Mórágý Granite in SW Hungary has been completed; the most important deformation zones are well-known and have been published on high-resolution maps. Nevertheless, fracture networks at micro- and meso-scales, which play a significant role in hydrodynamic behaviour of the hard rock body (Anders et al., 2014), are basically unknown and are studied in the framework of the present project. The most essential questions are whether the single fractures form a communicating network or not, how large the communicating subsystems are and how do fracture networks behave when heating and re-opening by laser treatment. To answer these questions, fracture networks are simulated based on measurable geometric parameters determined at tunnel ends of an underground storage system. Fracture networks are usually handled as scale invariant geometrical objects (e.g., Korvin, 1992, Turcotte, 1992, Long, 1996, Weiss, 2001). Modelling requires geometric data regarding fracture size distribution, spatial density and orientation. Simulated models are afterwards available to understand features of the fractured rock body concerning hydrodynamic behaviour, such as connectivity, porosity and permeability.

7.2. Geological background

The studied granitoid body (Mórágý Granite Formation – MGF) is located in the south-western part of Hungary. Petrographically the MGF was described by Király and Koroknai (2004) as a porphyritic monzogranite intercalated with a more mafic variety of monzonitic composition without a sharp contact (Figure 84). Two major deformation events developed the ductile structure of the MGF. The magma-mixing process coincided with formation of a generally NE-SW striking igneous foliation mostly with a steep NW dip. During the next phase, deformation resulted in steeply foliated mylonitic zones, basically with a NE-SW strike again. The upper several tens of metres of the granitoid body are strongly altered and weathered and are covered by Miocene, Pliocene and Quaternary sediments with a thickness of approximately 50 m on the hilltops and thinning towards the valleys. As a consequence, only a few surface outcrops exist that are available for petrological and structural study. Many details of mineralogical, geochemical and petrological circumstances of the MGF, not directly concerning the present project, are presented in Király (2010) and references therein.

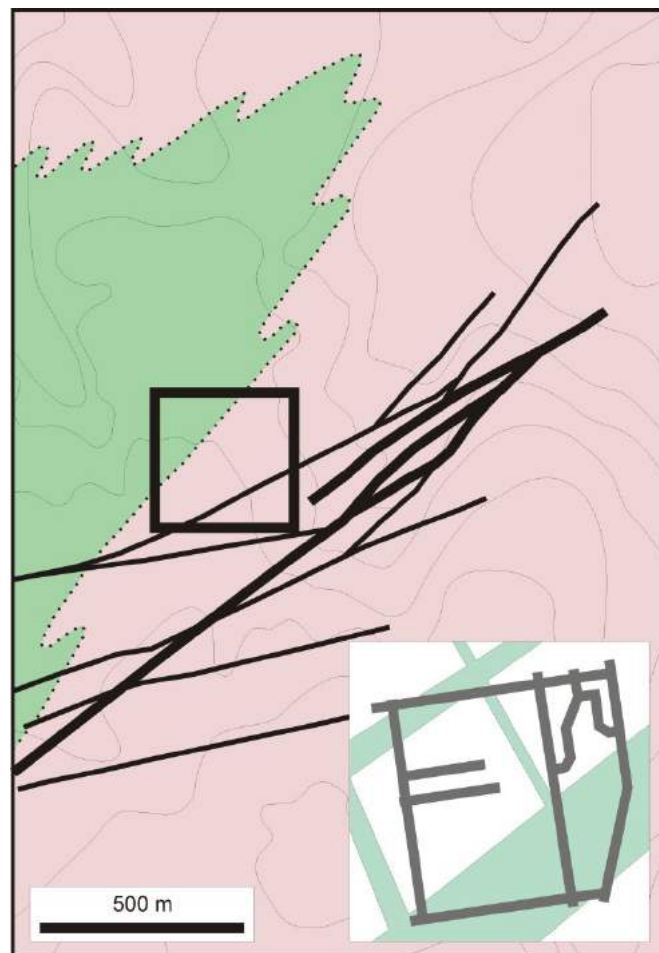


Figure 84: Simplified geological map of the study area (after Balla, 2004). Pink: monzogranite-dominated realm, green: monzonite-dominated realm. Bold lines denote proven major shear zones. Inset: sketch map of the underground site

The brittle deformation history of the area and the mechanisms of different structural events are discussed in detail by Maros et al. (2004). Most structures exhibit two typical orientations: NE-SW (the dominant set) and perpendicular to this (NW-SE) (Figure 84). Small-scale fracture orientations are very similar to those appearing at large-scale zones (Benedek and Molnár, 2013). When studying fracture networks from a geometric aspect, fracture size appears to be related to the distance from major fault zones; larger fractures appear to cluster preferentially around them (Benedek and Molnár, 2013). Nevertheless, length exponents were found varying within a very narrow range (2.15–2.44) at different scales (outcrop scale: 0.4–7 m trace length, vertical seismic profile measurements: 6–40 m trace length, seismic line measurements: 100–400 m trace length, Benedek and Dankó, 2009).

Generally, a fractured reservoir system can be divided into two subsystems; more permeable discontinuities surround a less permeable matrix (Neuman, 2005). This theoretical model is the basis of the hydrostructural concept of the MGF as well (Molnár et al., 2010). Benedek and Molnár (2013) distinguish two hydraulic domains inside the fractured granitoid body; less transmissive blocks and more transmissive zones (LTBs and MTZs, respectively). Nevertheless, the definition of the boundaries between these two domains is highly subjective. The MTZs follow both NE-SW and NW-SE directions, with the most significant flows observed along the NE-SW zones. Fractures inside an LTB, on the other hand, cannot be represented by any single

characteristic orientation. Although hydraulically active fracture zones are frequent in the study area, fracture clusters are not entirely interconnected. As a consequence, there is no hydraulic connectivity between all points of the studied region (Benedek and Dankó, 2009). According to Benedek et al. (2009) such a compartmentalization is not exclusively the result of fracture geometry, but in part the consequence of intensive secondary mineralization of certain fracture zones. The resulting strongly compartmentalized character of the fracture system causes the high complexity of the flow pattern as well. Neighbouring compartments usually have slightly different heads (1–5 m), while hydraulic jumps at compartment boundaries defined by sealed faults may be as great as 5–25 m. In general, hydrodynamic behaviour and especially the calculated transmissivity is significantly different for the two differently deformed regions, varying being 10^{-12} and 10^{-6} m²/s for the fresh granite of the LTBs and $8 \cdot 10^{-6}$ and $2 \cdot 10^{-5}$ m²/s for the MTZs (Balla et al. 2004).

7.3. Samples

In this study of the brittle structures of the Mórág granite body, 2D fracture network data were derived from tunnel ends representing the ground level of the underground repository site (Figure 84). Altogether 120 JointMetriX3D (Gaich et al., 2005, Deák and Molnos, 2007) images were handled with an equal 20 m lag between the neighbouring sampling points. At least 300 single fractures were digitized and evaluated in each JointMetriX3D image.

7.4. Methods

Fracture networks can be characterized from numerous structural geological points of view and by diverse measurable geometric parameters. In the latter approach, each single fracture must be represented by an appropriate geometric shape. In most approximations a polygon or a circle is used for this reason (Neuman, 2005). Hereafter, this last approach is followed, and so the most important geometric parameters to define a fracture are length (diameter), spatial position of the centre and orientation. To calculate porosity and permeability data for the fracture network, the fractures must have positive volume, so instead of pure circles, each fracture is represented by a flat cylinder geometrically. Furthermore, in order to understand spatial behaviour of fracture networks, a large set of discrete fractures should be studied simultaneously, and distributions of length, aperture, orientation (strike and dip) and spatial density of fracture midpoints are used. Abbreviations of the geometric parameters applied are summarized in Table 18.

Table 18: Abbreviations used in fracture network modelling

Abbreviation	Meaning
L	length of a fracture in 3D
l	trace length of a fracture in 2D
a	aperture of a fracture
α	dip direction of a fracture
β	dip angle of a fracture

N	number of fractures
D	fractal dimension in general
E, F	parameters of the length distribution function ($N(L) = F * L^{-E}$)
A, B	parameters of the aperture function ($a = A * L + B$)
Φ	fractured porosity

During the fracture network modelling process three sets of methods are used. 1) The first of them deals with determination of fracture network geometric parameters. 2) Prior to fracture network simulation using the above parameters, they should be interpolated for the studied area. 3) Finally, appropriate simulation software should be applied for 3D fracture network modelling.

7.5. Geometric parameters of fractures

Length distribution

Length distribution is an essential parameter of fracture networks concerning conductivity and fluid storage alike. According to numerous previous studies, fracture lengths follow a power law distribution (Yielding et al., 1992, Min et al., 2004), that is $N(L) = F * L^{-E}$. Using an appropriate number of single fractures on any 2D surface, the parameters of E (the length exponent) and F can be determined by image-analysis methods on digital photos. First, the frequency distribution function of fracture trace lengths measured on any photo were plotted. When computing the histogram, the number of classes (k) was determined so that $k = 2 * \text{INT}(\log_2(N(L)))$. Length exponent is afterwards the slope of the best fit line on the $\text{Log}(L)$ - $\text{log}(N(L))$ plot. Due to representativity defects, the smallest and longest fractures usually do not fit to this line and thus they should be left out of the analysis. This approach was followed when evaluating data of the tunnel ends.

Spatial density of fracture midpoints

Numerous previous studies proved that fracture systems behave geometrically, in a fractal-like pattern (Barton and Larsen, 1985, La Pointe, 1988, Hirata, 1989, Matsumoto et al., 1992, Kranz, 1994, Tsuchiya and Nakatsuka, 1995, Roberts et al., 1998, among others). Consequently, the spatial distribution of single fractures can be characterized by the fractal dimension of the fracture midpoints. Fractal dimension is computed using the box-counting method, applied to fracture network analysis by numerous authors previously (Mandelbrot, 1983, Mandelbrot, 1985, Barton and Larsen, 1985, Barton, 1995). Here, a non-overlapping regular grid of square boxes was used during the box-counting analysis. In the algorithm, the number of boxes ($N(r)$) required to cover the pattern of fracture seeds is counted. Fractal dimension is calculated by computing how this number changes in making the grid finer, afterwards: $N(r) \sim r^{-D}$. For box-counting calculations, the Benoit 1.0 software was used.

Fracture orientation

In the near-well fracture network modelling procedure, orientation data (dip direction and dip angle) of individual fractures obtained by BHTV interpretation were used (Szongoth et al., 2004). For modelling the underground site, orientation data measured in the closest well were used.

7.6. Fracture network modelling

Hereafter, for simulating fracture networks in 3D, the RepSim code was used (M. Tóth, 2010, M. Tóth and Vass, 2011, Bauer and M. Tóth, 2016). In this DFN (discrete fracture network) software penny-shaped single fractures are generated in a stochastic manner with a given parameter set of (D, E, F, α, β) measured in the real fractured rock body. Thanks to the stochastic approach in the fracture system generation, numerous equally probable networks can be simulated and evaluated. Aperture is calculated for each discrete fracture in a deterministic manner assuming the aforementioned length-aperture relationship (Odling, 1993). One of the most essential features of a simulated fracture network is the size and spatial position of its communicating subsystems. In the applied software, they can be found using a properly optimized trial-and-error algorithm (M. Tóth and Vass, 2011).

Fractured porosity can be defined as

$$\Phi = \frac{V_f}{V}, \quad (6)$$

In the case of cubic cells $V = r^3$, the total volume of the fractures inside a certain cube (V_f) can be approximated well by the lower Riemann sum, that is,

$$V_f = \sum_{i=1}^n \sum_j \frac{l_{ij} \cdot a_{ij} \cdot r}{n}, \quad (7)$$

and the porosity is in the form of

$$\Phi = \frac{1}{n \cdot r^2} \sum_{i=1}^n \sum_j l_{ij} \cdot a_{ij}, \quad (8)$$

The permeability of a fractured rock mass can be represented by a 3×3 permeability tensor. In the RepSim code, it is calculated using the slightly modified algorithm of Oda (1985). Thus, under Darcy's law,

$$v_i = \frac{g}{\mu} \cdot \rho \cdot k_{i,j} \cdot J_i \quad (9)$$

where v is the specific flow rate, μ is the dynamic viscosity, ρ is the density of the fluid, and J is the hydraulic gradient. On the other hand, as fluid can percolate only along fractures, over a given volume,

$$v_i = \frac{1}{V} \cdot \int v_i^f \cdot dV^f \quad (10)$$

where v_i^f is the flow velocity in a discrete fracture. This is approximated ad libitum by

$$v_i = \frac{1}{V} \cdot \sum_f v_i^f \cdot V^f \quad (11)$$

Under the cubic law, where assuming laminar flow within a fracture (parallel plate model, Witherspoon et al., 1980, Neuzil and Tracy, 1981), the specific flow rate is proportional to the square of the fracture aperture, and

$$v_i^f = \frac{1}{12} \cdot \frac{g}{\mu} \cdot \rho \cdot a^2 \cdot J_i^f \quad (12)$$

where J_i^f is the i th component of J projected onto the f fracture, that is, as

$$J^f = J - (n \cdot J) \cdot n \quad \text{and} \quad (13)$$

$$J_i^f = \sum_j (\delta_{ij} - n_i n_j) \cdot J_j \quad (14)$$

where δ_{ij} is the Kronecker symbol. Thus, finally comparing (4) and (6) according to Oda (1985),

$$k_{i,j} = \frac{1}{12} \cdot (P_{kk} \cdot \delta_{ij} - P_{ij}) \quad (15)$$

and under the discretization solution of Koike and Ichikawa (2006), considering that in the case of cubic cells $V = r^3$,

$$P_{ij} = \frac{1}{r^3} \cdot \sum_f a^3 \cdot l \cdot n_i \cdot n_j, \quad (16)$$

Finally, using the lower Riemann sum approximation

$$P_{ij} = \frac{1}{k \cdot r^3} \cdot \sum_k \sum_f a^3 \cdot l \cdot n_i \cdot n_j, \quad (17)$$

and

$$P_{kk} = P_{11} + P_{22} + P_{33}, \quad (18)$$

where n_i and n_j are the normal vector projections of the given fracture on the particular axes.

For modelling the underground site, the size of the whole modelled block is $300 \times 300 \times 150$ m, that is both above and under the repository site a 75 m-thick rock body was involved. As there are reliable data exclusively from the shafts themselves, input geometric data were assumed identical vertically. The aim for modelling a significant volume instead of only the horizon of the repository site itself is to let fractures combine communicating systems in 3D. For simulation, the whole modelled block was divided into $10 \times 10 \times 15$ parts of cells. Finally, the results of 10 independent runs were evaluated and compared. In each case, fracture models were evaluated concerning size and spatial position of the communicating subsystems, and typical values for fracture porosity and elements of the permeability tensor were computed.

7.7. Fracture network of the underground site

E and D data detected in the tunnel ends vary in a range of 1.03–2.27 and 1.50–1.86, respectively. Variography, fulfilled for spatial interpretation of these data around the underground site, proves that both variables (E , D) are regionalized variables and so are able to be extended spatially.

Based on the computed variograms both D and E were interpolated for the whole studied area using a grid of cells with 30×30 m in size. Using these maps, 10 independent fracture networks were simulated using the RepSim code. When evaluating all realizations, conspicuous differences appear in addition to the obvious similarities (Figure 85). A mutual, communicating fracture system with a NE-SW strike appears in each model in the SE part of the area. The N-S oriented network in the western end also becomes rather stable. Each model agrees that these two large fracture subsystems do not communicate with each other. Evaluation of the role of the third-largest system in the north is, nevertheless, much less obvious. Some models suggest that it communicates with that in the SE, while other realizations find connection improbable (Figure 85). The reason for the virtual controversy of these models must be that the northern subsystem is close to the percolation threshold. In the case of this class of fracture networks connectivity cannot be predicted; there is a possibility to develop both communicating and non-communicating fracture systems within the given geometrical circumstances. An identical situation appears in the SW part of the area, where the role of

numerous small subsystems becomes obscure. There is no way to decide whether they are linked with the neighbouring systems or not. It is essential that, in harmony with the suggestions of the parameter maps, a hardly fractured block appears in the middle of the studied underground site.

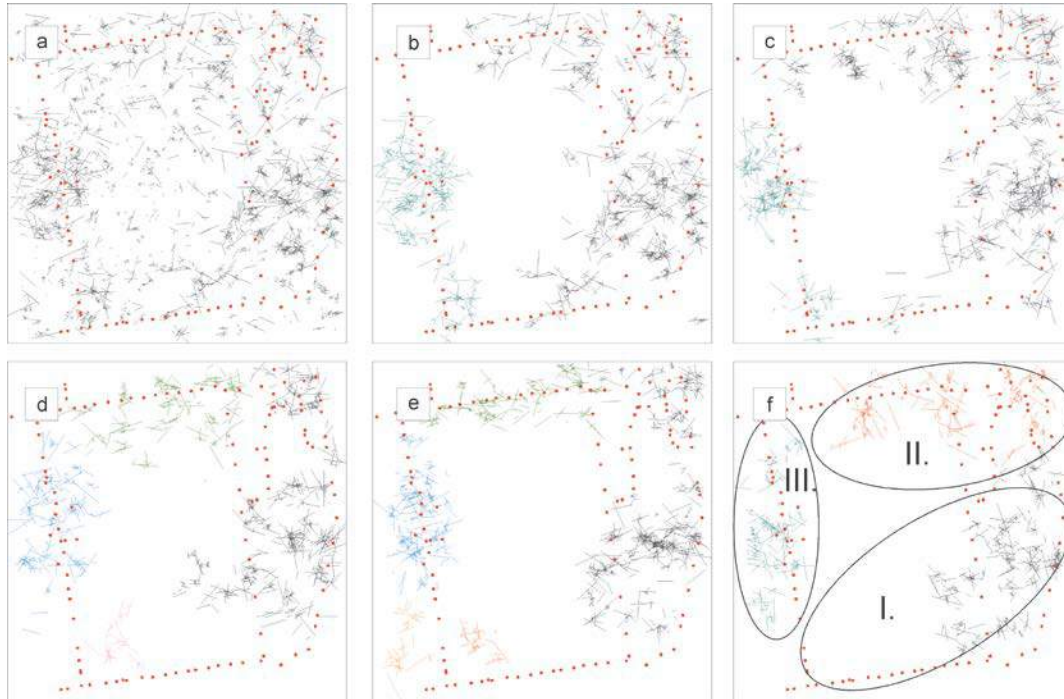


Figure 85: Alternative fracture network models simulated for the underground site. Figures show results of different runs. Colours denote interconnected subsystems. a) Total fracture network of a selected run. b) Communicating subsystems of the same run. c-f) Communicating subsystems resulting from different runs

It is also suggested that the fracture system in this middle zone represents a network well below the percolation threshold, that is, the fracture network remains unconnected even if D value is significantly underestimated, while E is overestimated. This image is very well in agreement with the general structural concept of the presence of a “less transmissive block” surrounded by NE-SW- and NW-SE-oriented, more transmissive zones, characteristic of the Mórággy Granite body. This connectivity pattern does not change at all if each fracture shorter than 1 m is deleted in the model simulating the role of vein cementation. Such pattern stability argues for the results of Benedek et al. (2009) and suggests that the compartmentalized appearance of the fracture system is rather the result of geometry *versus* vein cementation.

7.8. Effect of enhancing

The effect of enhancing by high power laser and fracking on the fractured granite body was simulated using the RepSim software as well, based on measured fracture geometry parameters.

Concerning fracture network connectivity relations, the granite mass can be classified into three basic groups. In some part of the body single fractures combine to form a communicating fracture network. The SE part of the modelled underground area is a typical example. In another parts of the body only a few fractures form small connected networks, so the fracture system is classified as unconnected. A typical example is the middle zone of the modelled area. Finally, in some parts of the rock body the fracture system is close to the percolation threshold, the transition stage between the other two extremes. In this case the whole system is very sensitive to tiny change in fracture geometry parameters; a little increase in either fracture density or length may modify unconnected character to a well-connected one and *vice versa*. A typical example is the SW part of the modelled rock body.

Connectivity behaviour of fractures in a granitoid body as a potential object for petrothermal utilization is a key parameter. Realms with a very well connected fracture system should not be a desirable choice, because of the potential waste of injected water in a highly permeable fracture network. Neither regions with fracture systems significantly below percolation threshold should be aimed, because of the negligible permeability in these regions. As the above model suggests, regions with different percolation characteristics co-exist inside an actual rock body.

In the present model a rock body with a fracture network close to the percolation threshold is evaluated. Using the RepSim code the effect of complex enhancing is modelled so that only the lengths of the single fractures are increased. Previous experiments (e.g. Stoeckhert et al, 2015; Hoek and Martin, 2014) clearly proved that in most rock types new fractures do not form, rather the lengths of the original fracture set increase due to artificial fracture propagation. The main question of the simulation is whether only a slight increase in lengths (that is no change in fracture density) in the case of a fracture network close to the percolation threshold may modify connectivity, effective porosity and permeability or not. For modelling, fracture parameters of the SW part of the modelled region were chosen. We used average D and E parameters of 6 neighbouring cells; the used values are $D = 1.74$, $E = -1.64$. Orientation data were measured in the nearby well that penetrated the MGF. To simulate the effect of fracture propagation, E was increased with a lag of 0.1 up to -1.14, all other parameters were not modified. For porosity and permeability calculations $a/L = 3 \cdot 10^{-3}$ was chosen in harmony with literature data and previous measurements on the MGF rocks (see above). For each case 5 independent models were computed; typical horizontal cross sections of the fracture network models are shown in Figure 86.

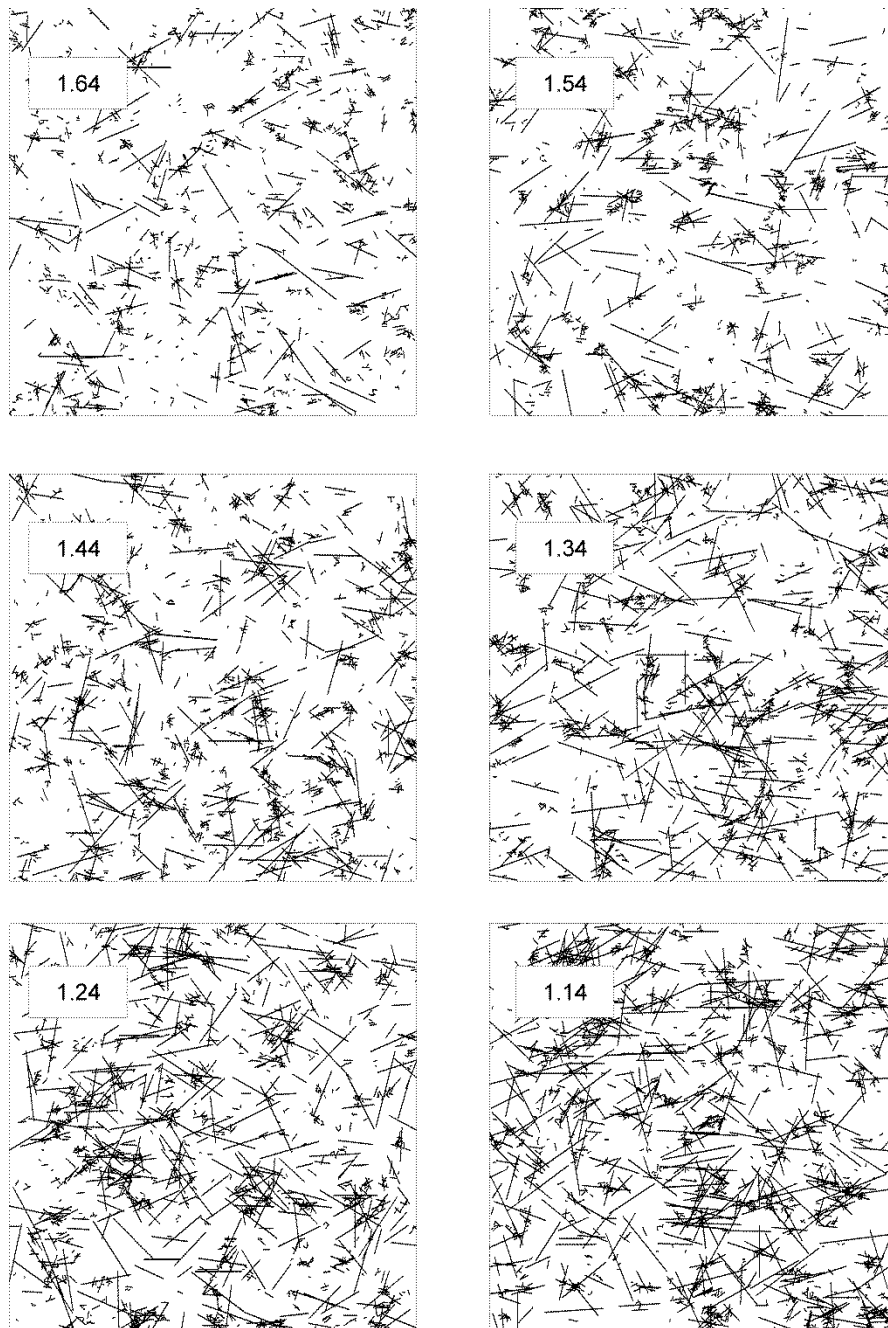


Figure 86: Horizontal sections of fracture network models from $E = -1.64$ up to -1.14

When plotting the size of the largest connected subsystem (P_{max}) as a function of the E parameter, a monotonous increase becomes typical as E changes from -1.64 to -1.14 . Moreover, while at the percolation threshold different runs resulted in significantly different P_{max} values (9.7% – 23.5%, Figure 87), when increasing E , this value becomes rather stable (Figure 87). This result of the simulation suggests that even a slight increase of the fracture lengths may increase the size of communicating subsystem.

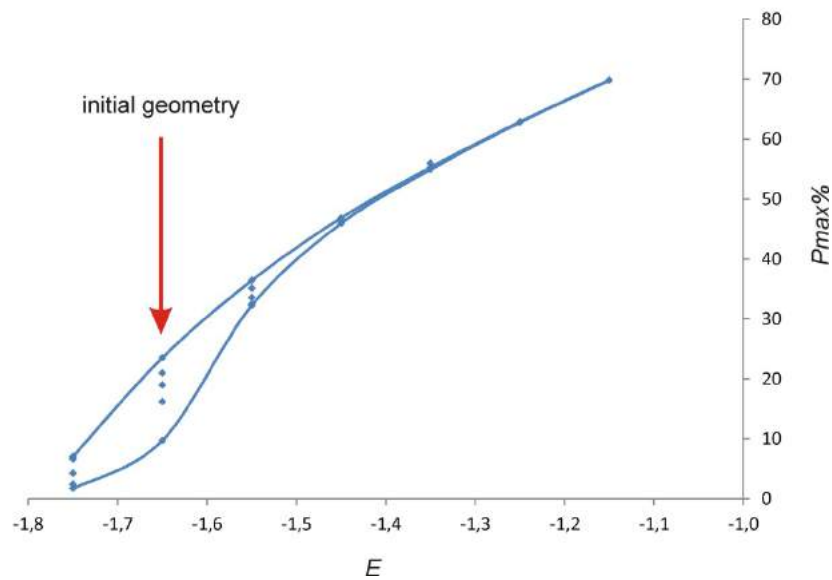


Figure 87: Change of the size of the largest connected fracture system when increasing E between -1.64 and -1.14. For each case 5 independent models were computed

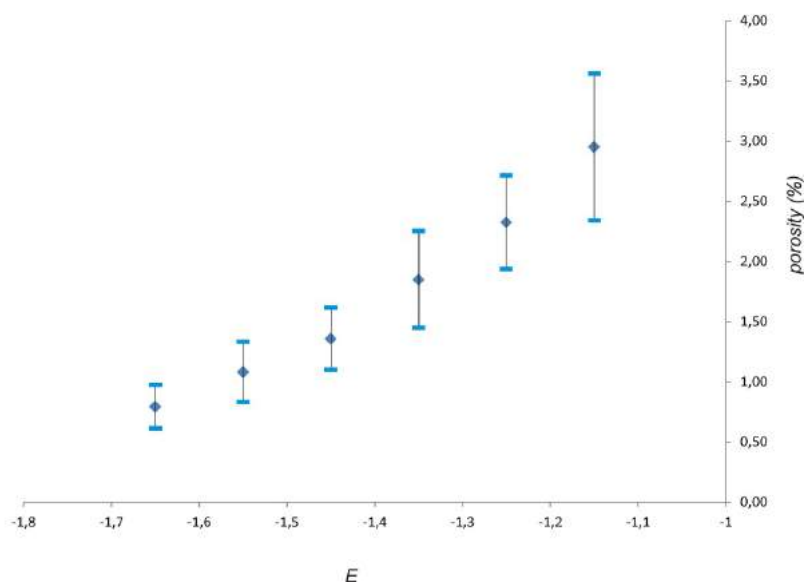


Figure 88: Calculated effective fracture porosities. (Range shows $\pm 1\sigma$)

Concerning porosity, while at the initial parameter set <1% values are computed, for the network with $E = -1.15$ effective porosity becomes as large as $\sim 3\%$ (Figure 88). Interestingly, standard deviations of the calculated porosities (based on 160 cells in each case) increase with increasing E values. Although porosities increase with a factor of ~ 4 due to increase in fracture lengths, this change modifies permeabilities (Figure 89); calculated average values vary in around one order of magnitude increasing from $\sim 1.5E-13 \text{ m}^2$ up to $6E-13 \text{ m}^2$. Nevertheless, a coupled increase of the two hydrodynamic parameters is proved by the models.

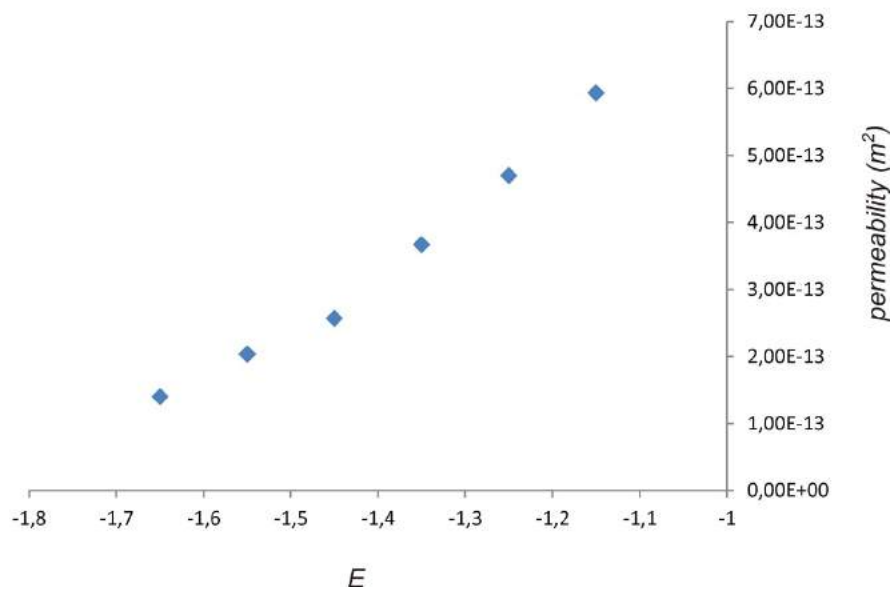


Figure 89: Calculated permeabilities when increasing E from -1.64 up to -1.14. Data are given as the average of the diagonal of the intrinsic permeability tensor (16 independent calculations)

Accepting that for petrothermal utilization rock bodies with a fracture network close to the percolation threshold are worth choosing, the following consequences may be drawn. Inside the rock volume where enhancing may increase lengths of the pre-existing fractures, a significant increase in the size of the connected fracture system and in porosity can be expected. Simultaneously, permeability will possibly change about an order of magnitude. To change permeability more significantly, new fractures should be developed, that is fracture density (D value) should be increased.

8. Three-dimensional fluid, heat- and mass-transport model to define the extractable amount of heat and metallic minerals regarding different scenarios

Reservoir enhancing is a very complex procedure, which requires adequate qualifications to develop a desirable fracture system. The main risks associated with the developing of an EGS are the hydraulic fracturing itself and the quality of the generated fractures. The information available about the fracture and its flow regime in such depths is very limited.

The model system and its behavior may be very complex, depending on the amount of details we wish to include. Many times, we need to simplify the description of the system and its behavior somewhat so that it may be used to solve a given problem. In order to compare the original (intact) and complex enhanced reservoir (laser treatment and fracking), regarding fluid flow and exploitable amount of heat, FeFlow, a finite element modelling system was applied. (Finite element code FEFLOW v7.0 is generally accepted for fluid flow and heat transport simulation).

8.1. Model domain

Lacking a well-explored study area an abstract reservoir was chosen, whose area is 50x60 km with 10 km depth (Figure 90). The target layer is situated around 5000 m below surface (Figure 91). We chose such a big area (semi-regional scale) so that the model would not be sensitive to the boundary conditions. The igneous basement complexes can be found in similar disposition in Hungary for example (M. Tóth et al, 2000).

Model boundaries:

- saturated flow,
- no flow horizontal boundaries, (water flow from the upper porous layers are not investigated)
- the model boundary follows the geological settings,
- 3D elements with mesh refinement in the target area; (1D, 2D element were not used)

For modelling purposes, the above structure was divided into 15 layers including 1993 grid points in each slice (Table 19). The basement dome consists of granite rock types with hydraulically different parameters which were reduced with depth inside the crystalline body, due to increased pressure. It is covered with pebbly sediments in the deep basins and thick, lacustrine clayey marl. The top of the section consists of sandstone throughout the model block (Figure 92). The hydrodynamic parameters are taken from previous RepSim simulations (Table 20). The initial hydraulic heads were calculated based on hydrostatic pressure. The upper and lower boundaries were defined by constant hydrostatic head. Due to boundary conditions and hydraulic parameters the model represents a gravity driven flow system. To set up the initial heat transport parameters for the model, 120 mW/m² constant heat flux was used at the bottom of the model (Table 21). This is based on the assumptions that lateral change of the lithology can be neglected at deeper horizons and the heat flow from the mantle is uniform within our bounded area. The upper and side boundaries, where lateral inflow is allowed are characterized by constant temperature. In the case of thermal conductivities, we used the measurement results taken on core samples with temperature correction applied for these values.

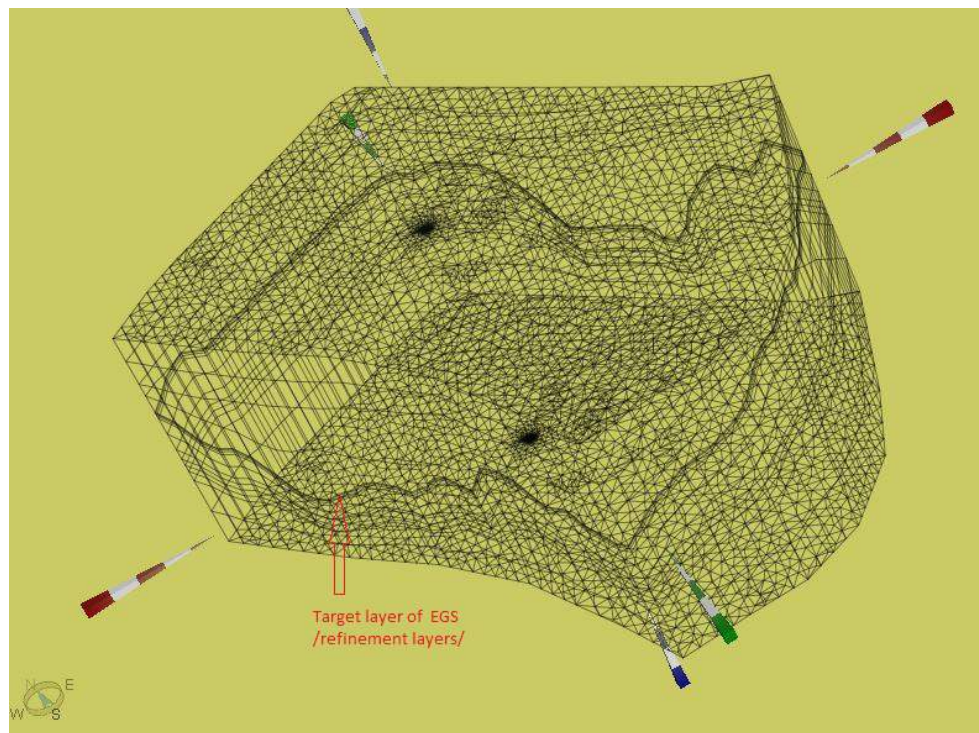


Figure 90: Hull of model domain

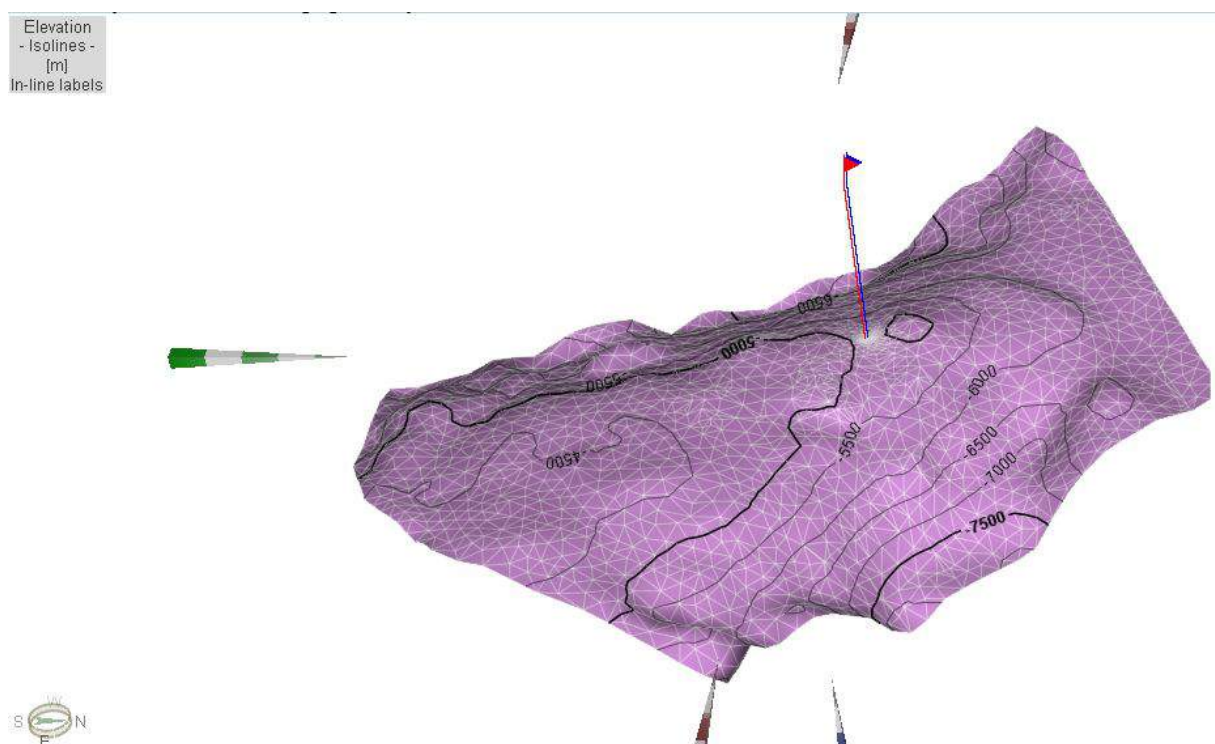


Figure 91: Target layer of EGS with elevation isolines (flag symbolises the centre of enhanced zone)

Table 19: Characteristic data of the model

Problem Class	
Description	Combined flow and heat process
Type	Saturated
Projection	3D confined aquifer
Time Class	Transient flow / transient transport
Time Stepping	Adams-Bashforth/Trapezoid rule (AB/TR) predictor-corrector
Mesh	
Number of Dimensions	3
Nodes per Element	6
Element Type	Triangular prism
Mesh Elements	57,960
Mesh Nodes	31,888
Problem geometry	
Number of Layers	15
Number of Slices	16
Elements per Layer	3,864
Nodes per Slice	1,993

Table 20: Hydrodynamic parameters in the model domain

Layers	Stratigraphic units	Lithology	Porosity	Hydraulic conductivity
1. 2. 3. 4.	Topography, Quaternary Upper Pannonian Lower Pannonian	gravel, sand (coarse, fine) sand, clayey sand sandy clay clay /basin fill sediments/	Depth dependent expression: 0.22-0.004	Highly anisotropic media $K_{xx} = K_{yy} = 35 - 0,1 * e^{-4} \text{ m/s}$ $K_{zz} = 0.35 - 0.0001 * e^{-4} \text{ m/s}$
5-16.	Granitic sequence basement	crystalline and siliciclastic rocks of highly different permeability (weathered zone, altered zone, intact zone)	Depth dependent expression: 0.16-0.0003 fracking volume= 0.04	Isotropic $K_{xx} = K_{yy} = K_{zz} = 0.002 - 0.00025$ $* e^{-4} \text{ m/s}$

Table 21: Heat transport parameters in the model domain

Initial temperature (by layers):	11,5-429 °C
Porosity:	0,00031-0,22
Volumetric heat capacity of fluid:	4,2 MJ/m ³ K
Volumetric heat capacity of solid:	2,52 MJ/m ³ K
Thermal conductivity of fluid	0,65 J/m/s/K
Thermal conductivity of fluid	1,8 – 3,48 J/m/s/K
Longitudinal dispersivity	5 m
Transverse dispersivity	0,5 m
Heat transport:	
Temperature BC – 1 st slice	11,5 °C
Heat flux BC – bottom slice	10368 J/m ² /d = 120 mW/m ²

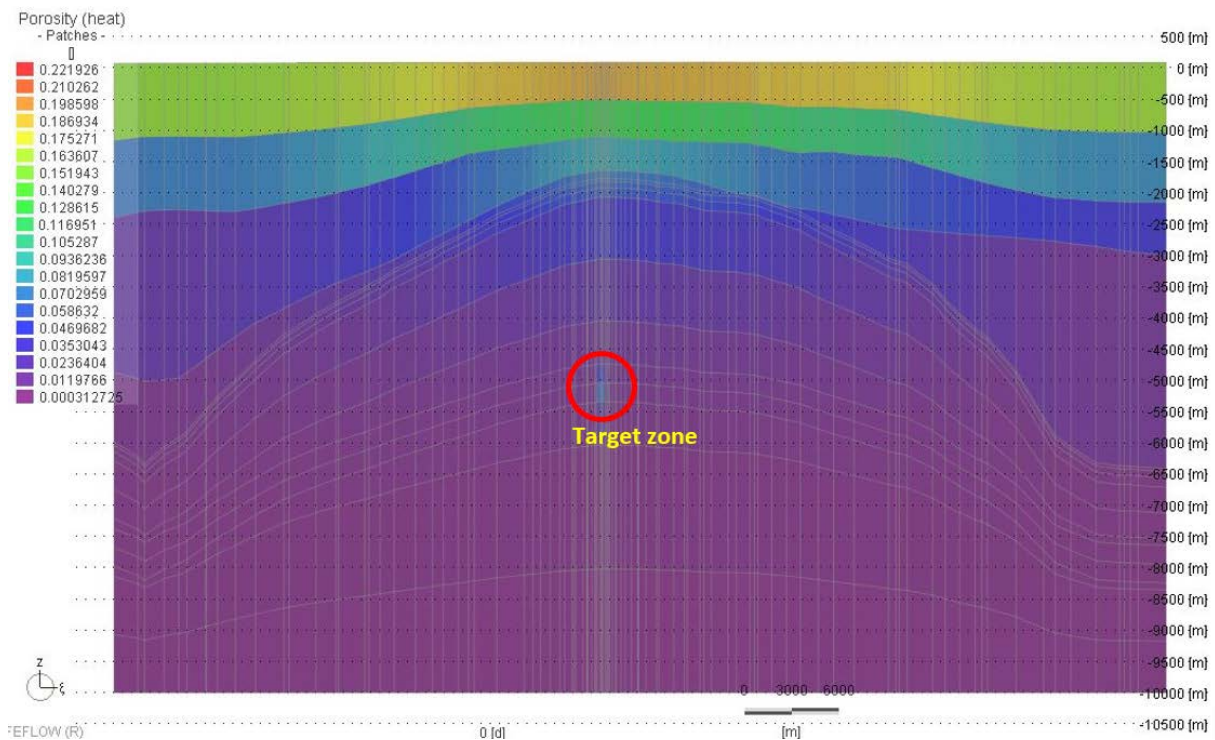


Figure 92: Distribution of porosity along the SW-NE section in different layers

8.2. Scenarios

We investigated 2 scenarios:

- 1.) doublet production in case of enhanced (laser + fracking) fracture network
- 2.) doublet production in case of original fracture network;

Both producing and injecting wells are situated in the center of granitic zone. The distance of planned production and injection wells is 605 m along mesh edges (Figure 93). The reinjected water temperature was 80°C. In the first case, there is a more permeable “pocket” in a less permeable matrix thanks to enhancing of granite between 11 -13 layers (Table 22). This pocket was evolved by laser treatment and fracking. First, we run the model without wells for 200 000 years to obtain stationary water pressure and temperature data (Figure 94).

In the case of enhanced reservoir, we injected and produced 3500 m³ fluid per day (40 l/s). We calculated depression in the model and in the second scenario we calculated how much production volume belongs to this depression in the case of untouched reservoir conditions.

Table 22: Hydraulic parameters of enhanced granitic layers

Layers	Stratigraphic units	Lithology	Porosity	Hydraulic conductivity
11.	Enhanced Granitic sequence basement	crystalline and siliciclastic rocks	0.02	$K_{xx} = K_{yy} = K_{zz} = 0.0075 * e^{-4} \text{ m/s}$
12.			0.04	$K_{xx} = K_{yy} = K_{zz} = 0.015 * e^{-4} \text{ m/s}$
13.			0.02	$K_{xx} = K_{yy} = K_{zz} = 0.0075 * e^{-4} \text{ m/s}$

8.3. Results of water and heat flow simulation

In the first case scenario, the extraction of 3500 m³/day fluid results a roughly 150 m depression in the water table (Figure 95). To achieve a similar depression 300 m³/day fluid production is enough in the original (intact) case (Figure 96). During injection, the cold water will advance along the fractures, gradually extract heat from the adjacent rock matrix, and eventually arrive at the production wells. If the injected water is not fully heated up by then, detrimental effects on energy production from decreasing fluid enthalpies may result (this phenomenon is known as thermal breakthrough). To check the cooling effect temperature distribution presented along a 100 years' time in the production well in the case of scenario 1.) and 2.) which were similar, except for the missing thermal breakthrough in the case of intact granite (Figure 97 and Figure 98). The thermal breakthrough manifested after 70 years in the first case scenario. Thus, this production rate is sustainable. To show the cooling effect around the injection well in the enhanced case, we figured the calculated temperature distribution after 5, 20, 50, 70 and 100 years (Figure 99-103).

8.4. Mass transport calculation

The amount of metal that can be extracted with the fluid can be calculated by multiplying the concentration determined by the release experiments by the amount of fluid produced. Since the experiments resulted in the release of Pb, Zn and Li in amounts close to ppm these may be recovered in quantities close to 3kg / day. This calculation does not take into account the fact that during the operation of the geothermal system the concentration may change (it may increase due to new fractures in the system caused by the injection of cold water, or, it may decrease over time due to continuous release). Details of this process will be addressed in WP5.

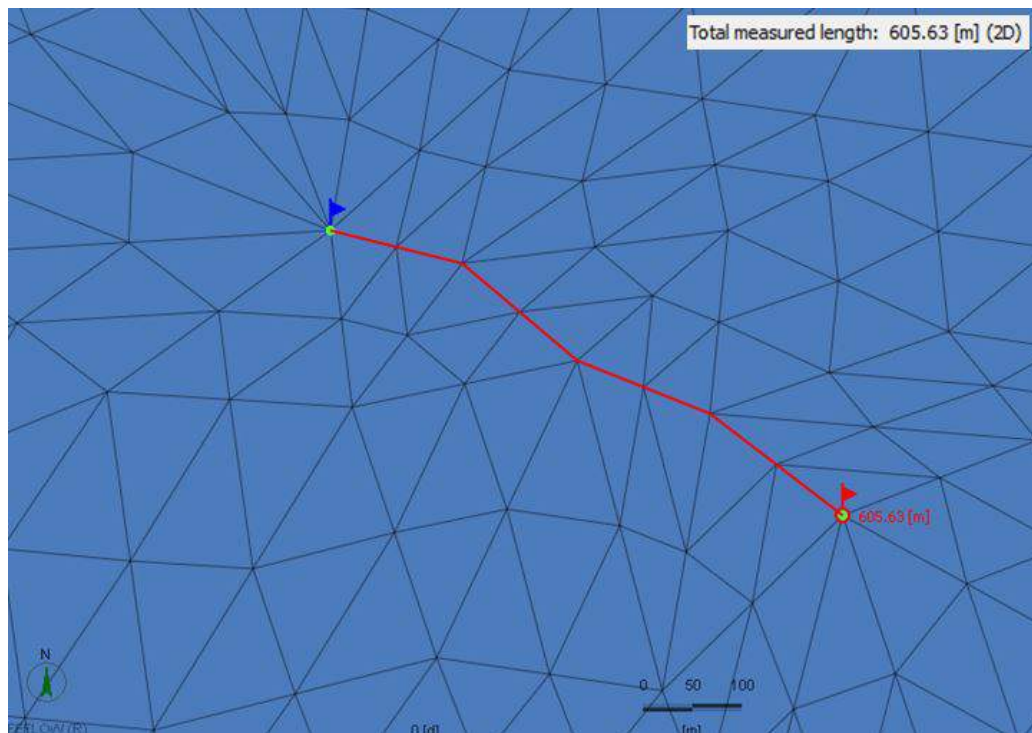


Figure 93: Location of planned EGS system's wells (Distance between the wells is 605 m along mesh edges; blue flag: production well, red flag: injection well)

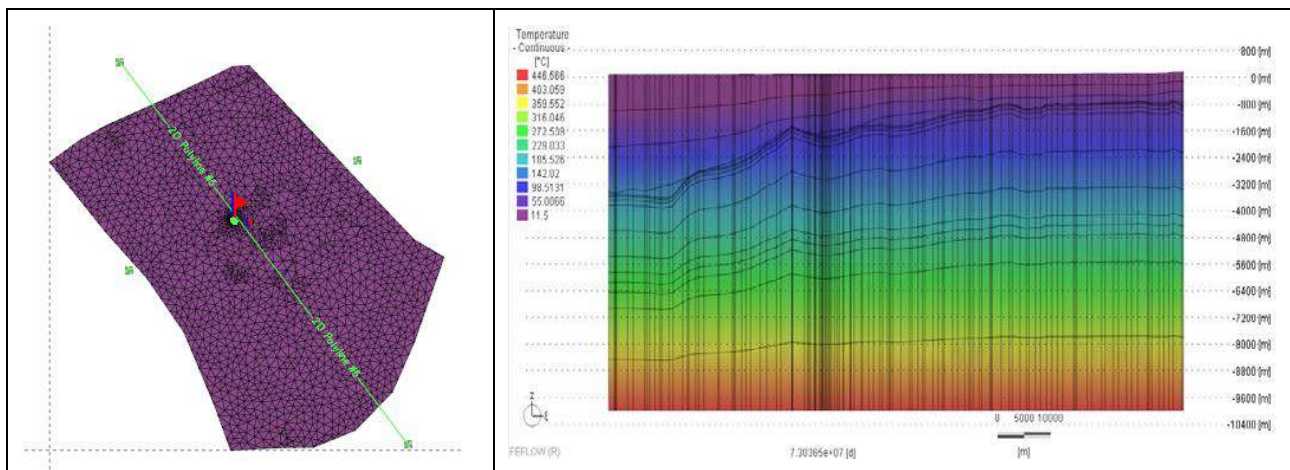


Figure 94: Modelled steady state temperature distribution (°C) in a cross section after 200000 years model run

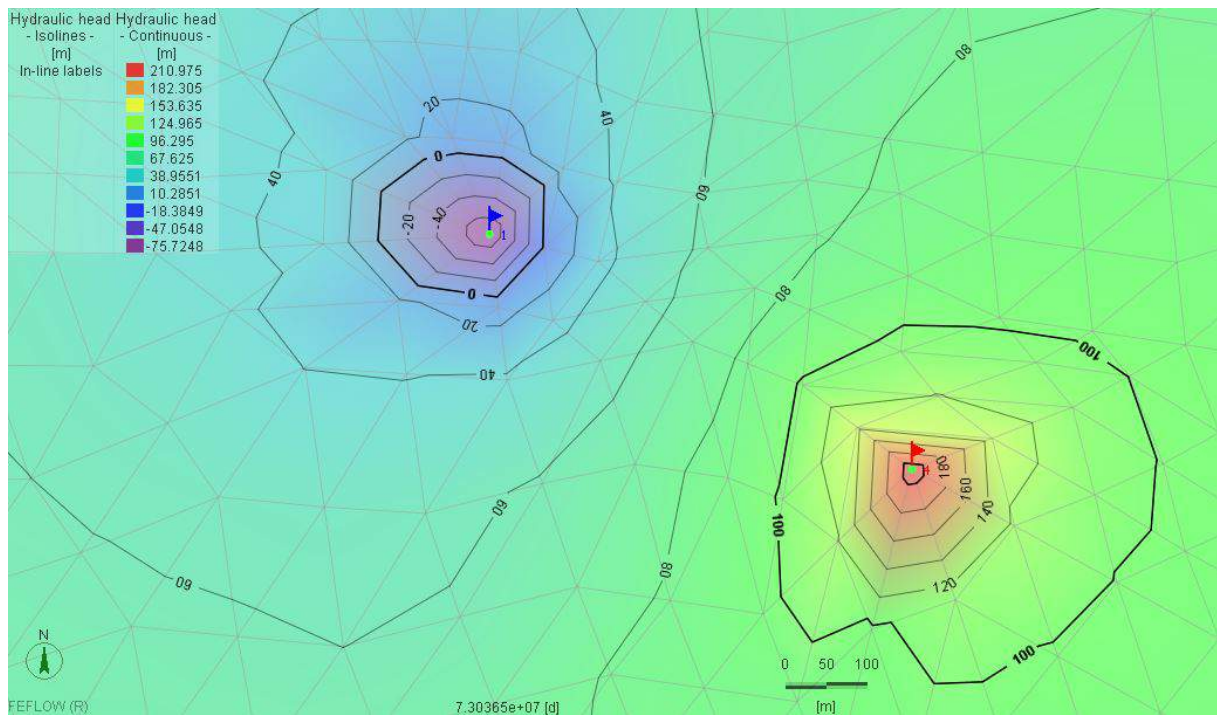


Figure 95: Hydraulic head (m) after 100 years operation (yield is 3500 m³/day) in case of enhanced granite (the initial head was around 80 m)

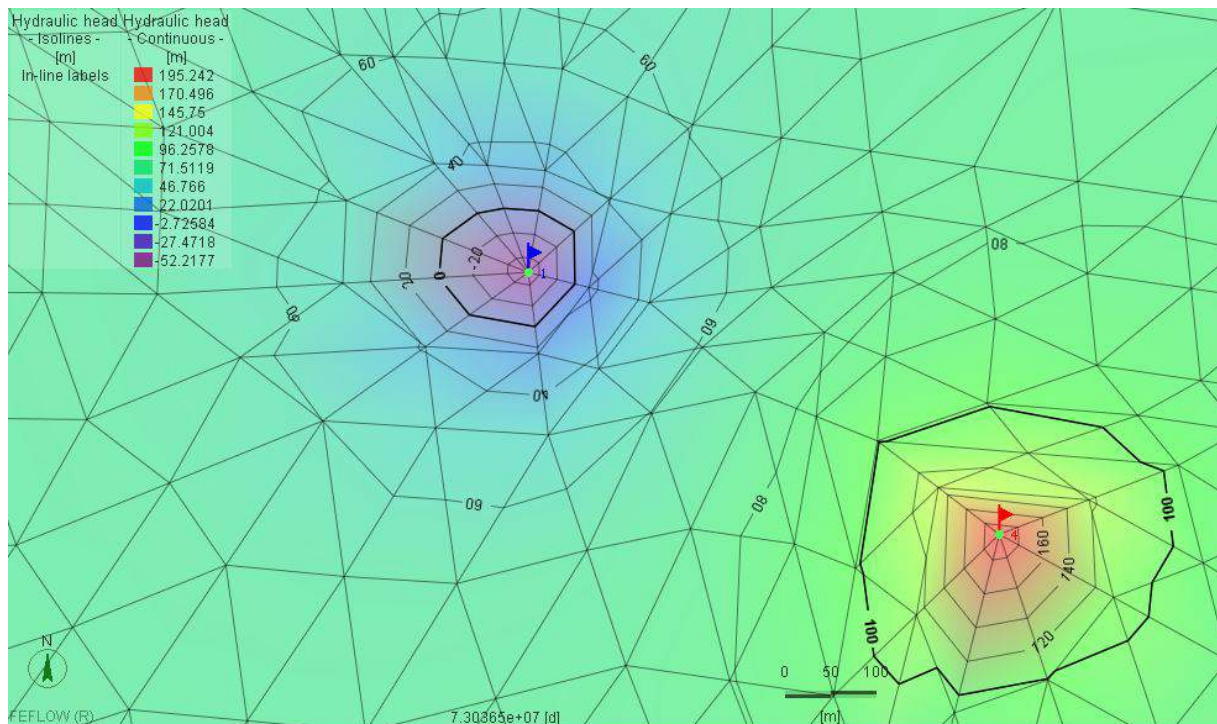


Figure 96: Hydraulic head (m) after 100 years operation (yield is 300 m³/day) in case of intact granite (the initial head was around 80 m)

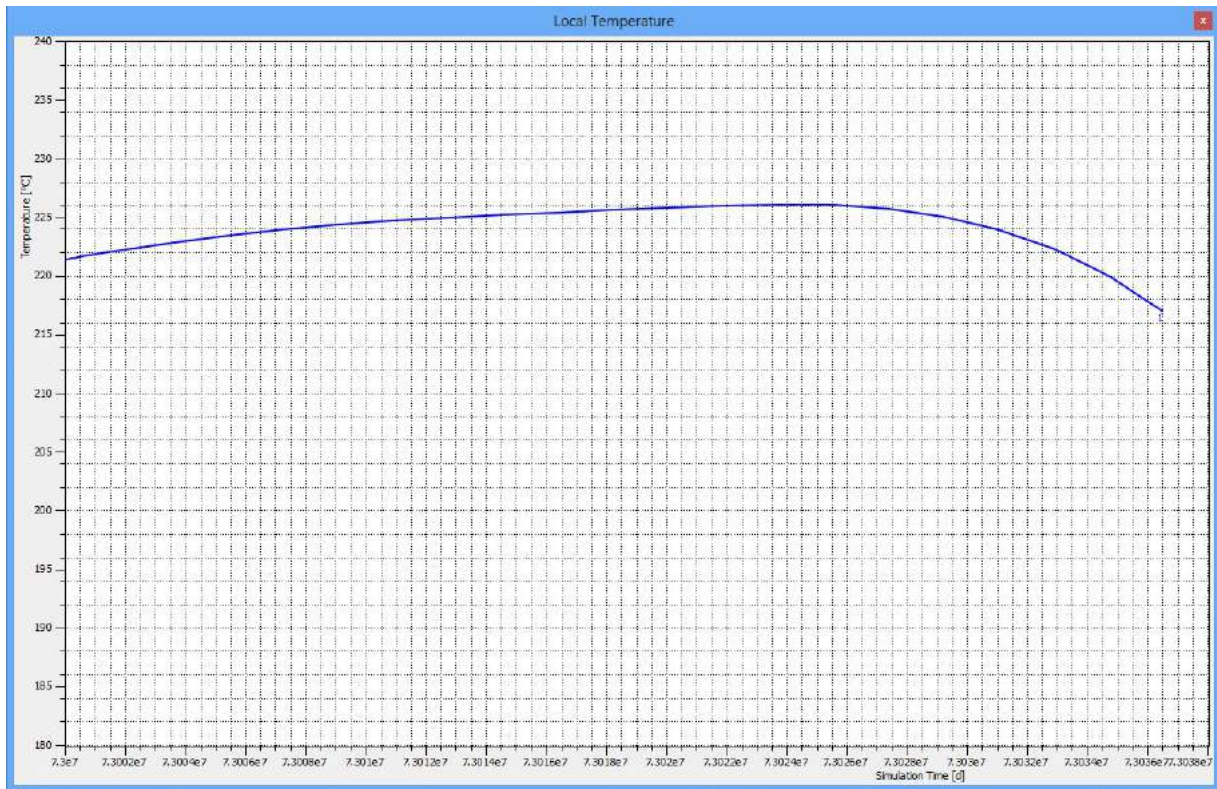


Figure 97: Modelled temperature-time graph in production well (3500 m³/day) during 100 years operation in case of enhanced granite

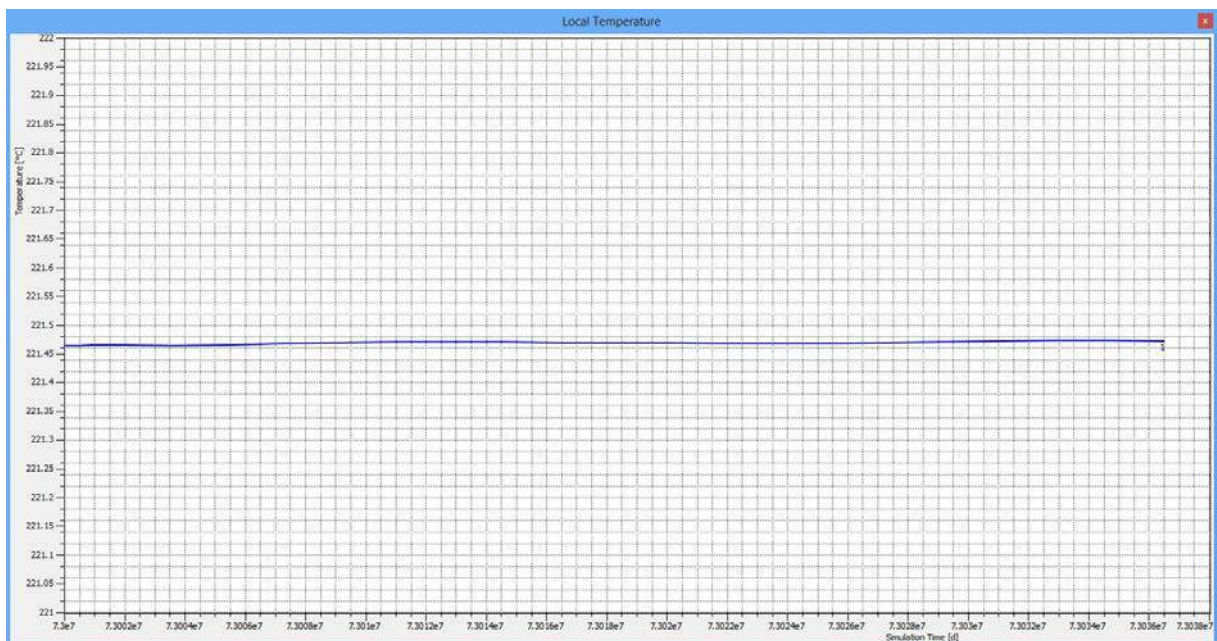


Figure 98: Modelled temperature-time graph in production well (300 m³/day) during 100 years operation in case of intact granite

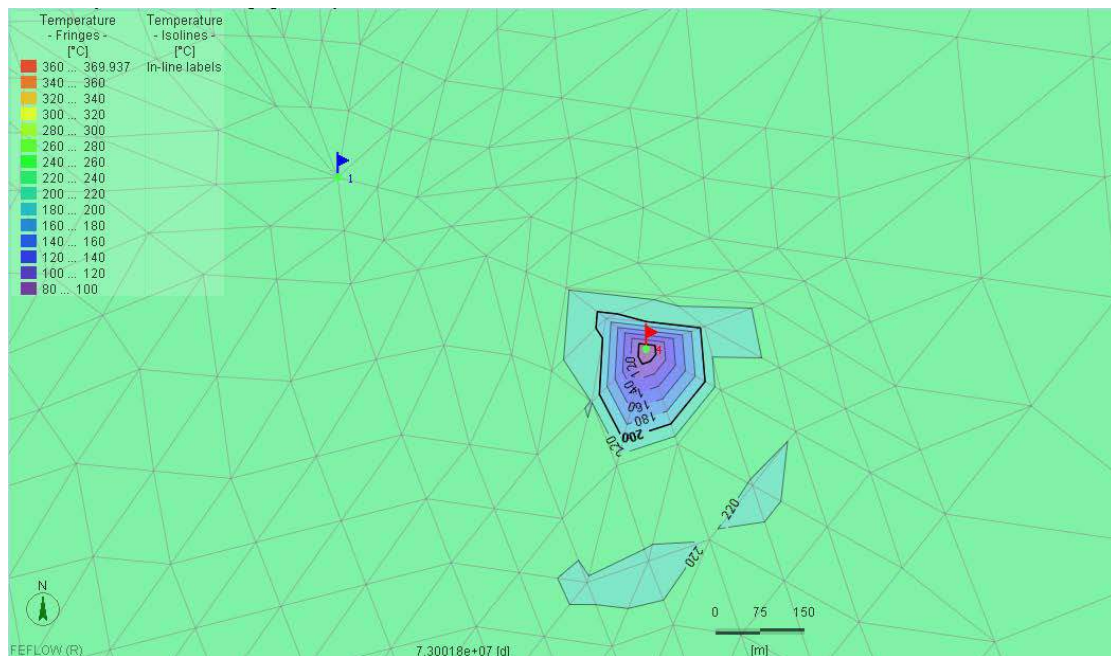


Figure 99: Temperature distribution after 5 years injection in case of enhanced granite

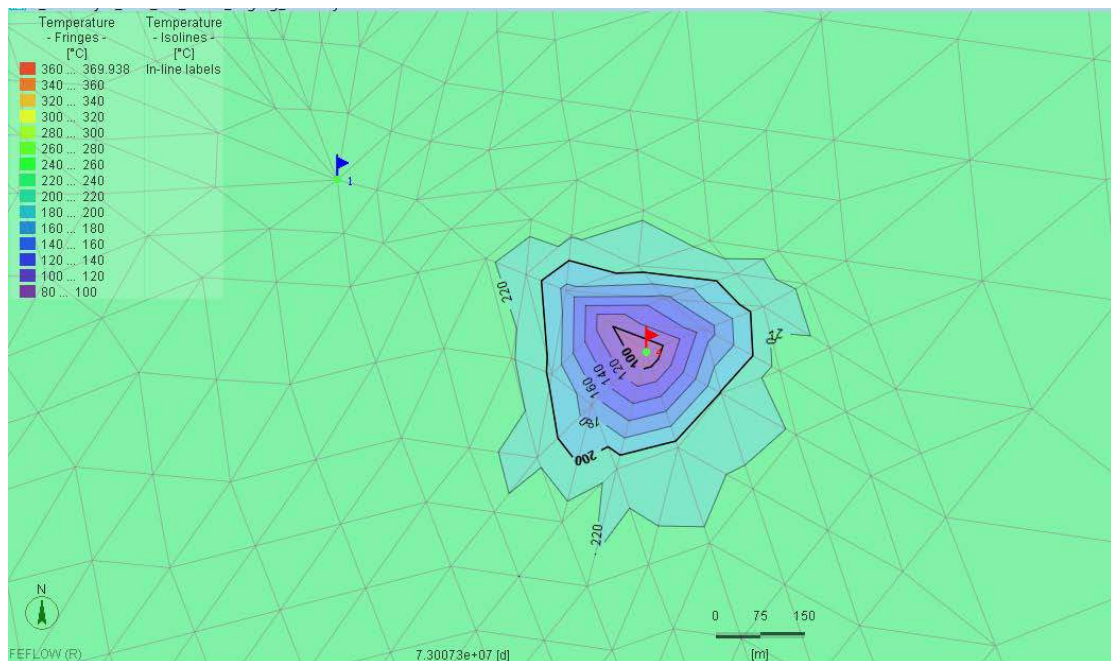


Figure 100: Temperature distribution after 20 years injection in case of enhanced granite

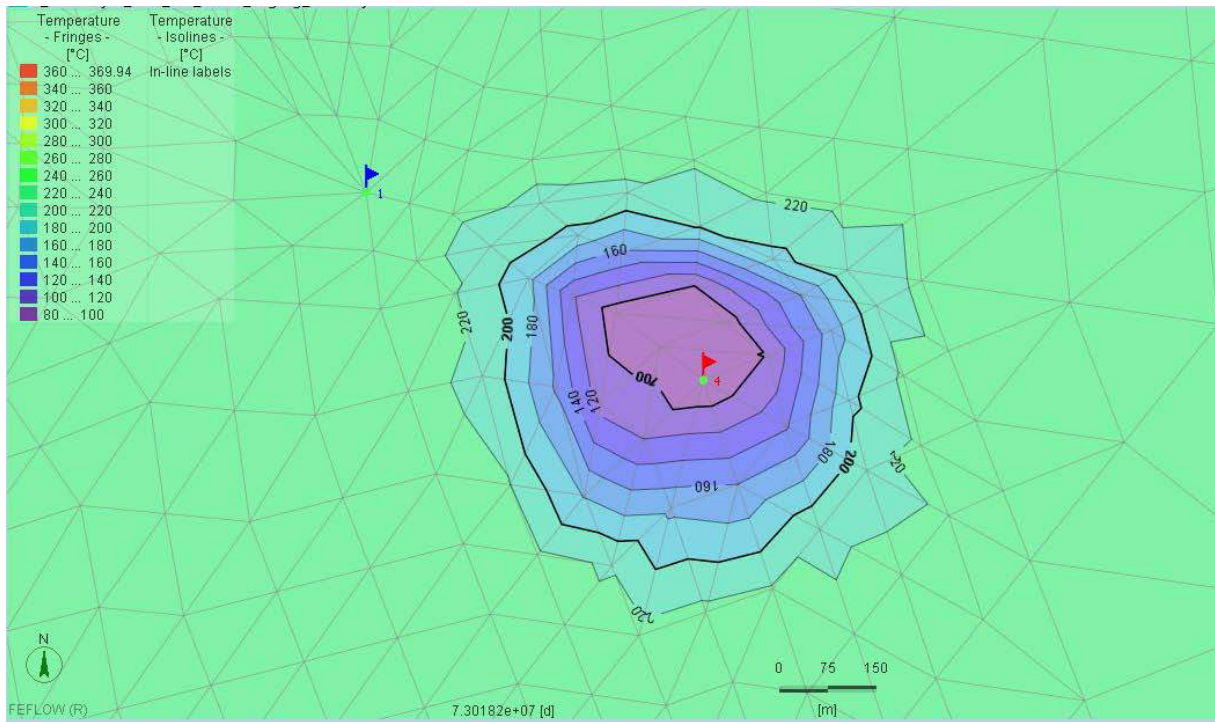


Figure 101: Temperature distribution after 50 years injection in case of enhanced granite

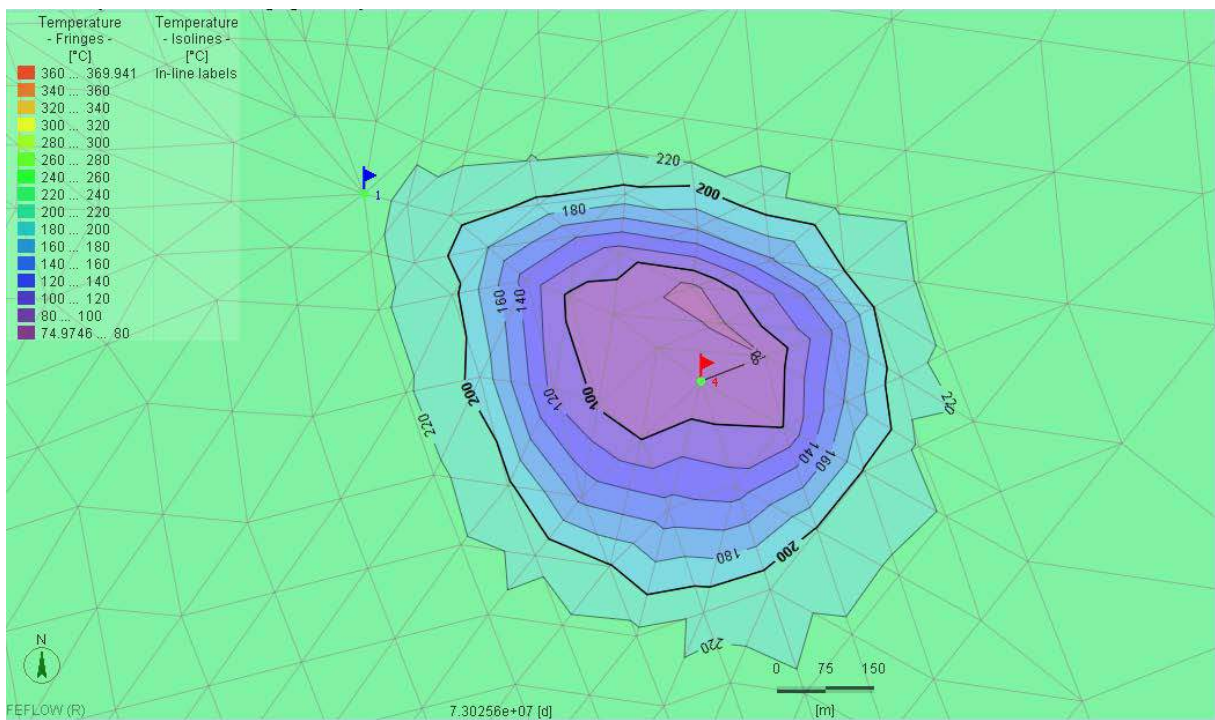


Figure 102: Temperature distribution after 70 years injection in case of enhanced granite

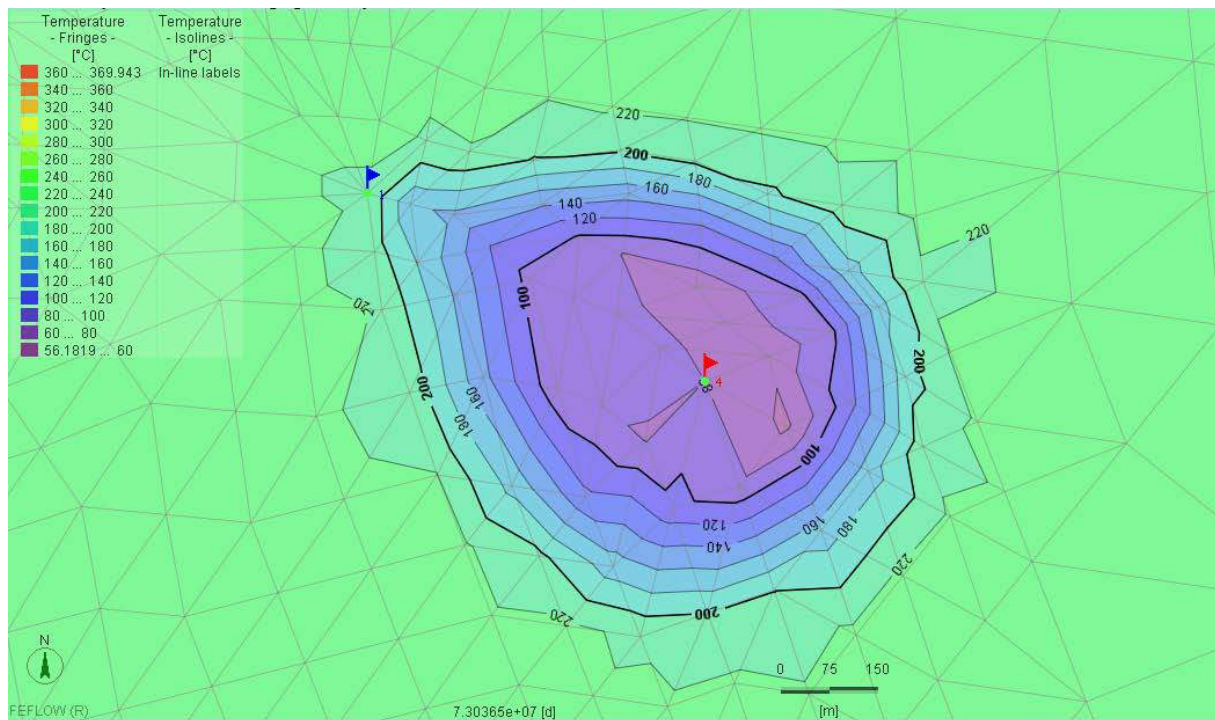


Figure 103: Temperature distribution after 100 years injection in case of enhanced granite

8.5. Conclusions

With the parameters defined in the previous sub-tasks we prepared the intact and fractured granite storage model. The modeling has clearly demonstrated that under the defined boundary conditions, due to laser intervention and hydraulic fracture, a near even increase of the storage permeability in the order of approx. 1 scale is sufficient to produce a fluid at a temperature of at least 200 °C with a yield of 40 l / s, during which the thermal breakthrough will occur with a significant delay (in approx. 70 year).

Although any model is only a simplified copy of the reality, it has some unsurpassable advantages in theoretical and practical exploration. Modeling provides an inexpensive and fast tool to reproduce situations of unlimited variant numbers. Any new data, which are in contradiction with this knowledge, require the restructuring of the model and restarting the calibration and simulation process. The results can only be accepted if the input data are free of contradiction and suit the reality on the level our actual knowledge.

9. Conclusions

During laboratory measurements heat conductivity of 14 different rock samples was measured with a TK04 thermal conductivity meter. During the laser treatment of the rock it was realized that the heating effect of the laser beam can be used for heat conductivity determination. With this method, 3 igneous rock samples were measured.

Information about the stress field of 19 CHPM related rocks were measured by uniaxial and triaxial compressive sets and indirect tensile strength by Brasil tests. Rock mechanical information, such as Young's modulus, angle of internal friction and hyperbolic failure curve were calculated.

The possibility of fracture enhancement by a novel laser technology (1.5 kW performance) was also investigated in 10 andesite and 3 granite samples. Findings indicate that rock failure may occur at lower stress level during destructive rock mechanical tests that include laser shock. This implies that rigid rocks can be broken up to several smaller samples, and a number of new ruptures can be developed.

To investigate the effectiveness of leaching of metals, a custom-built fluid flow reactor was used, to provide the physical parameters (250°C temperature and 250 bar pressure) of a neutral reservoir in artificial environment. A fluid flow range from 0.1 ml/min to 5 ml/min was maintained in the pipe reactor. The main findings were enhanced Pb, Zn and Li release. The best result achieved around 500 ppb Li mobilization during cca. 1/2-hour contact time.

A three-dimensional stochastic fracture model (RepSim) was built on the data of granite rocks to compare the fracture network systems of natural and enhanced conditions. Our main findings include permeability increase of 1 order of magnitude and porosity increase of 3-5 times as a result of rock stimulation.

Finite element fluid flow and heat transport (Feflow) modeling, based on data from the aforementioned sub-tasks, resulted in 3500 m³/day (40 l/s) fluid production in the case of an enhanced reservoir. Assuming a 120 mW/m² average heat flux at the bottom of the reservoir modelled the temperature of the fluid produced from 5 km depth was above 200°C. Projecting these parameters to a pilot site we concluded that metal production may reach magnitudes in the order of kg/day.

When dealing with such a complex task, many difficulties arise. In our case the first of these is data availability, or rather the lack thereof. Even though rock samples are available from the four pilot sites in the project, no rock mechanical nor hydrological data is available. To solve this, an abstract system based on real rock type and actual rock stress data was created. Data obtained from this abstract system was derived and processed for three-dimensional fracture, fluid-, heat and mass transport models. Another difficulty was the limitation of time. Scientifically and logically it makes sense to conduct one measurement after another on the same sample, however, due to the limitation of time, some experiments and simulations had to be carried out parallel. With such boundary conditions present our results are to be interpreted as possible realizations. The possibility to use our methodology on a larger scale and to upscale the parameters were in the focus during the abstraction of this system. The large-scale use of the novel laser reservoir enhancing technology is under development, while a piloting test applicability is expected within ten years.

10. References

- ANDERS, M. A.; LAUBACH, S. E.; SCHOLZ, C. H. 2014: Microfractures: A review. *Journal of Structural Geology* **69**, 377–394.
- BALLA, Z. (ED.) 2004: Annual report of the Geological Institute of Hungary, 2003.
- BALLA, Z.; HORVÁTH, I.; TÓTH, GY.; BENEDEK, K.; MEZŐ, GY.; MOLNÁR, P. 2004: Hydrogeological pattern of the Bátaapáti (Üveghuta) site. Ann. Report Geol. Inst. Hung., 449–472.
- BARABÁS, E. 2015: Determining thermal conductivity of volcanic rocks from the Tokaj mountain and heat transport simulations with GMS software. Thesis work, University of Miskolc (in Hungarian).
- BARTON, C. C.; LARSEN, E. 1985: Fractal geometry of two-dimensional fracture networks at Yucca Mountain, Southwestern Nevada. In: Stephanson, O. (ed.): *Proc. Int. Symp. on Fundamentals of Rock Joints*, 77–84.
- BARTON, C. C. 1995: Fractal analysis of scaling and spatial clustering of fractures. In: Barton, C. C., La Pointe, P. R. (eds.): *Fractals in the Earth Sciences*. Plenum Press, New York, pp. 168.
- BAUER, M.; M. TÓTH, T. 2016: Characterization and DFN modelling of the fracture network in a Mesozoic karst reservoir: Gomba oilfield, Paleogene Basin, Central Hungary. *Journal of Petroleum Geology*, 40/3, 319–334.
- BENEDEK, K.; DANKÓ, GY. 2009: Stochastic hydrogeological modelling of fractured rocks: a generic case study in the Mórággy Granite Formation (South Hungary). *Geologica Carpathica*, 60, 4, 271–281.
- BENEDEK, K.; MOLNÁR, P. 2013: Combining structural and hydrogeological data: Conceptualization of a fracture system. *Engineering Geology*, **163**, 1–10.
- BENEDEK, K.; BÓTHI, Z.; MEZŐ, GY.; MOLNÁR, P. 2009: Compartmented flow at the Bátaapáti site in Hungary. *Hydrogeology Journal*, **17**, 1219–1232.
- BIENIAWSKI, ZT. 1967: Mechanism of brittle fracture of rock, parts I, II and III. *Int J Rock Mech Min Sci Geomech Abstr*, **4(4)**: 395–430.
- CAI, M. 2010: Practical estimates of tensile strength and Hoek–Brown strength parameter m_i of brittle Rocks. *Rock Mech Rock Eng*, **43(2)**: 167–184.
- DEÁK, F.; MOLNOS, I. 2007: Application of JointMetriX3D in geotechnical documentation of the Bátaapáti shafts. Török Á., Vásárhelyi B. (eds): *Mérnökgeológia-Kőzetmechanika 2007*, 11–18. (in Hungarian).
- EGERER, F.; KERTÉSZ, P. 1993: Bevezetés a kőzetfizikába; Akadémiai Kiadó, Budapest
- GAICH, A.; SCHUBERT, W.; PÖTSCH, M. 2005: Three-dimensional rock mass documentation in conventional tunnelling using JointMetriX3D. *Underground Space Use: Analysis of the Past and Lessons for the Future*, Taylor & Francis Group, London, 59–64.
- HIRATA, T. 1989: Fractal dimension of fault system in Japan: fracture structure in rock fracture geometry at various scales. *Pure and Applied Geophysics*, **131**, 157–170.
- HOEK, E.; MARTIN, C. D. 2014: Fracture initiation and propagation in intact rock – A review. *Journal of Rock Mechanics and Geotechnical Engineering*, **6**, 287–300.
- ISRM 2006: The Complete ISRM Suggested Methods for Rock Characterization, Testing and Monitoring: 1974–2006. Edited by R. Ulusay and J.A. Hudson.

- KIRÁLY, E. 2010: Magmatic evolution of the Mórággy Granite (SE Transdanubia, Hungary). Annual Report of the Geological Institute of Hungary 2009, pp. 41–45.
- KIRÁLY, E.; KOROKNAI, B. 2004: The magmatic and metamorphic evolution of the north-eastern part of the Mórággy Block. Annual Report of the Geological Institute of Hungary 2003, 299–300.
- KOIKE, K.; ICHIKAWA, Y. 2006: Spatial correlation structures of fracture systems for deriving a scaling law and modeling fracture distributions. *Computers and Geosciences*, **32/8**, 1079–1095.
- KORVIN, G. 1992: Fractal Models in the Earth Sciences. Elsevier, pp. 396.
- KOVÁCS, B.; CZINKOTA, I.; SZANYI, J.; BOZSÓ, T.; TÓTH, M.; SIMON, A.; BUSUTTIL, L. 2016: The permeability of laser drilled laterals in sandstone reservoirs. *Geosciences and Engineering*, **Vol. 3, No. 5** (2014), pp. 83–91.
- KRANZ, R. L. 1994: Fractal point patterns and fractal fracture traces. In: Nelson, Laubach, (eds.): *Rock mechanics*. Balkema, Rotterdam, 793–800.
- LA POINTE, P. R. 1988: A method to characterize fracture density and connectivity through fractal geometry. *International Journal of Rock Mechanics and Mining Sciences, Geomech. Abstr.*, **25**, 421–429.
- LONG, J. C. S. (ED.) 1996: Rock fractures and fluid flow: contemporary understanding and applications. National Academy Press, Washington D. C., pp. 551.
- M. TÓTH, T. 2010: Determination of geometric parameters of fracture networks using 1D data. *Journal of Structural Geology*, **32**, 878–885.
- M. TÓTH, T.; SCHUBERT, F.; ZACHAR, J. 2000: Neogene exhumation of the Variscan Szeghalom dome, Pannonian Basin, E. Hungary. *Journal of Geology*, **35/3-4**, 265–284.
- M. TÓTH, T.; VASS, I. 2011: Relationship between the geometric parameters of rock fractures, the size of percolation clusters and REV. *Mathematical Geosciences*, **43**, 75–97.
- MANDELBROT, B. B. 1983: The Fractal Geometry of Nature. Freeman, New York, pp. 468.
- MANDELBROT, B. B. 1985: Self-affine fractal dimension. *Physica Scripta*, **32**, 257–260.
- MAROS, GY.; KOROKNAI, B.; PALOTÁS, K.; FODOR, L.; DUDKO, A.; FORIÁN-SZABÓ, M.; ZILAHÍ-SEBESS, L.; BÁN-GYÖRÝ, E. 2004: Tectonic analysis and structural evolution of the north-eastern Mórággy Block. Annual Report of the Geological Institute of Hungary 2003, 370–386.
- MAROS, GY.; KOROKNAI, B.; PALOTÁS, K.; MUSITZ, B.; FÜRI, J.; BORSODY, J.; KOVÁCS-PÁLFY, P.; KÓNYA, P.; VICZIÁN, I.; BALOGH, K.; PÉCSKAY, Z. 2010: Brittle fault zones in the Mórággy Granite (South Transdanubia): new structural and K-Ar data. Annual Report of the Geological Institute of Hungary 2009, pp. 91–112.
- MARTIN C. D. 1993: The strength of massive Lac du Bonnet granite around underground opening. PhD Thesis, p 278.
- MATSUMOTO, N.; YOMOGIDA, K.; HONDA, S. 1992: Fractal analysis of fault systems in Japan and the Philippines. *Geophysical Research Letters*, **19/4**, 357–360.
- MIN, K. B.; JING, L.; STEPHANSSON, O. 2004: Determining the equivalent permeability tensor for fractured rock masses using a stochastic REV approach: Method and application to the field data from Sellafield, UK. *Hydrogeology Journal*, **12/5**, 497–510.
- MOLNÁR, P.; SZEBÉNYI, G.; KOVÁCS, L. 2010: Preliminary geological interpretation of the Bátaapáti Site. Manuscript, PURAM, Paks, RHK-K-108/10. (in Hungarian).

- NAGY, Á.; M. TÓTH, T.; VÁSÁRHELYI, B.; FÖLDES, T. 2013: Integrated core study of a fractured metamorphic HC-reservoir; Kiskunhalas-NE, Pannonian Basin. *Acta Geod Geophys*, **48**:53–75.
- NEUMAN, S. 2005: Trends, prospects and challenges in quantifying flow transport through fractured rocks. *Hydrogeology Journal*, **13**, pp. 124–147.
- NEUZIL, C. E.; TRACY, J. V. 1981: Flow through fractures. *Water Resources Research*, **17/1**, 191–199.
- ODA, M. 1985: Permeability tensor for discontinuous rock masses. *Geotechnique*, **35**, 483–495.
- PALCHIK, V. 2011: On the ratios between elastic modulus and uniaxial compressive strength of heterogeneous carbonate rocks. *Rock Mech. Rock Engng.*, **44**: 121-128.
- PALCHIK, V. 2013: Is there link between the type of the volumetric strain curve and elastic constants, porosity, stress and strain characteristics? *Rock Mech. Rock Engng.*, **46**: 315-326.
- PALMSTRÖM A.; SINGH R. 2001: The deformation modulus of rock masses - comparisons between in situ tests and indirect estimates. *Tunnelling and Underground Space Technology*, **16**: 115-131.
- RAMAMURTHY, T.; MADHAVI, LATHA, G.; SITHARAM T. G. 2017: Modulus ratio and joint factor concepts to predict rock mass response. *Rock Mech. Rock Engng.* (in print)
- PETHŐ, G.; VASS, P. 2011: Geofizika alapjai, Miskolci Egyetem
- ROBERTS, S.; SANDERSON, D. J.; GUMIEL, P. 1998: Fractal analysis of the Sn-W mineralization from central Iberia: Insights into the role of fracture connectivity in the formation of an ore deposit. *Economic Geology*, **93**, 360–365.
- STOECKERT, F.; MOLENDÁ, M.; BRENNE, S.; ALBER, M. 2015: Fracture propagation in sandstone and slate – Laboratory experiments, acoustic emissions and fracture mechanics. *Journal of Rock Mechanics and Geotechnical Engineering*, **7**, 237–249.
- SUGGESTED METHODS FOR DETERMINING THE UNIAXIAL COMPRESSIVE STRENGTH AND DEFORMABILITY OF ROCK MATERIALS, *International Journal of Rock Mechanics and Mining Sciences & Geomechanics Abstracts*, **Vol. 16**, No. 2, pp.135-140.
- SUGGESTED METHODS FOR DETERMINING THE STRENGTH OF ROCK MATERIALS IN TRIAXIAL COMPRESSION: REVISED VERSION, *International Journal of Rock Mechanics and Mining Sciences & Geomechanics Abstracts*, **Vol. 20**, No. 6, pp.285-290.
- SUGGESTED METHODS FOR DETERMINING TENSILE STRENGTH OF ROCK MATERIALS, *International Journal of Rock Mechanics and Mining Sciences & Geomechanics Abstracts*, **Vol. 15**, No. 3, pp.99-103.
- SZONGOTH, G.; ZILÁHI-SEBESS, L.; SZÜCSI, P. 2004: Well logging at the Bátaapáti (Üveghuta) site. Annual Report of the Geological Institute of Hungary 2003, 119–134.
- TSUCHIYA, N.; NAKATSUKA, K. 1995: A two-dimensional mono-fractal approach to natural fracture networks in rock. *Geotherm. Sci. Tech.*, **6**, 63–82.
- TURCOTTE, D. L. 1992: Fractals and chaos in geology and geophysics. Cambridge University Press, pp. 221.
- ULUSAY, R.; HUDSON, J.A. 2006: The Complete ISRM Suggested Methods for Rock Characterization, Testing and Monitoring: 1974-2006.
- VÁSÁRHELYI, B.; KOVÁCS, L.; TÖRÖK, Á. 2016: Analysing the modified Hoek–Brown failure criteria using Hungarian granitic rocks. *Geomech. Geophys. Geo-energ. Geo-resour.*, **2**:131–136.

- WEISS, J. 2001: Fracture and fragmentation of ice: a fractal analysis of scale invariance. *Engineering Fracture Mechanics*, **68**/17-18, 1975–2012.
- WITHERSPOON, P. A.; WANG, J. S. Y.; IWAI, K.; GALE, J. E. 1980: Validity of cubic law for fluid flow in deformable rock fracture. *Water Resources Research*, **16**/6, 1016–1024.
- YIELDING, G.; WALSH, J. J.; WATTERSON, J. 1992: The prediction of small scale faulting in reservoirs. *First Break*, **10**, 449–460.

11. Appendices

11.1. Summary table of SAM (Special Approximation Method) data

Sample ID	TC [W/mK]	LET [-]	Start [s]	End [s]	Length [s]	Number of Solutions [-]	CV [-]
T102	0,82	8904,2	40,0	66,0	26,0	51	13,59
T103	0,82	1236,8	40,0	76,0	36,0	8	13,59
T104	0,80	5834,3	39,5	68,5	29,0	4	13,52
T1_101	1,07	2712,6	35,5	79,0	43,5	105	12,27
T1_102	0,98	7135,7	34,5	76,0	41,5	305	12,11
T1_103	0,98	7081,5	33,0	78,5	45,5	331	12,11
T1_104	1,00	2604,3	35,5	70,0	34,5	370	12,11
T1_105	0,97	7180,4	35,5	77,5	44,0	367	12,11
T1_301	0,70	1459,9	28,0	59,0	31,0	174	13,79
T1_302	0,70	14173,9	30,5	79,0	48,5	1486	14,30
T1_303	0,70	6041,0	24,0	73,5	49,5	1085	14,22
T1_304	0,71	21552,2	21,0	52,5	31,5	534	14,24
T1_305	0,71	37731,4	26,0	59,5	33,5	313	13,98
T1_306	0,71	1774,1	37,5	66,0	28,5	455	13,91
T1_307	0,72	11981,8	35,0	69,5	34,5	247	13,83
T1_308	0,71	9146,3	25,0	56,0	31,0	232	13,91
T1_309	0,72	1301,3	34,5	68,0	33,5	399	14,06
T1_310	0,72	46324,6	28,5	67,0	38,5	196	13,79
T201	1,84	44324,3	33,0	68,5	35,5	583	11,91
T202	1,84	3912,0	35,0	77,0	42,0	1323	12,27
T203	1,86	5586,6	28,0	66,0	38,0	761	12,27
T204	1,87	195698,6	31,5	75,5	44,0	922	12,27
T205	1,89	5320,8	28,5	69,0	40,5	459	12,27
T206	1,89	10734,9	30,0	73,5	43,5	514	12,27
T207	1,88	16168,2	24,0	74,5	50,5	692	12,27
T208	1,88	56382,4	20,0	59,5	39,5	633	12,27

Sample ID	TC [W/mK]	LET [-]	Start [s]	End [s]	Length [s]	Number of Solutions [-]	CV [-]
T209	1,90	89320,0	26,0	63,5	37,5	411	12,27
T210	1,87	16341,2	20,5	50,0	29,5	172	12,27
T301	0,75	279,6	29,5	68,0	38,5	891	11,48
T302	0,80	374,6	38,0	74,0	36,0	136	11,88
T303	0,78	73,9	40,0	71,5	31,5	2	11,72
T304	0,77	297,7	36,0	66,0	30,0	113	11,80
T306	0,78	385,9	39,0	66,5	27,5	35	11,88
T308	0,76	153,1	31,5	60,0	28,5	128	11,64
T309	0,77	924,2	31,0	59,0	28,0	43	11,72
T310	0,76	384,6	32,0	63,0	31,0	72	11,56
T401	0,78	137,4	36,0	67,5	31,5	169	12,27
T403	0,77	1854,9	34,0	71,0	37,0	274	12,19
T405	0,78	1687,3	37,5	63,0	25,5	59	12,34
T407	0,74	1497,3	24,0	59,5	35,5	335	12,19
T408	0,74	116,1	25,5	51,0	25,5	13	12,27
T410	0,80	1314,2	40,0	66,0	26,0	10	12,42
T501	1,17	14125,4	34,5	78,0	43,5	96	18,93
T502	1,16	1043,2	36,5	79,5	79,5	391	18,91
T503	1,16	22984,4	35,5	80,0	80,0	311	18,98
T504	1,18	13390,5	35,5	64,0	64,0	331	18,91
T505	1,15	6853,7	30,0	60,5	60,5	129	18,75
T506	1,15	13065,9	32,5	76,5	76,5	226	18,67
T507	1,14	357,7	35,5	68,5	68,6	64	18,44
T508	1,17	17375,8	34,5	68,0	68,0	389	18,75
T509	1,17	2664,4	34,5	74,0	74,0	359	18,83
T510	1,16	5152,8	31,5	77,5	77,5	339	18,83
T5_101	1,06	5543,7	38,5	75,0	36,5	123	11,56
T5_102	1,02	2897,8	30,5	56,5	26,0	104	11,48
T5_103	1,03	635,2	32,5	64,0	31,5	234	11,56

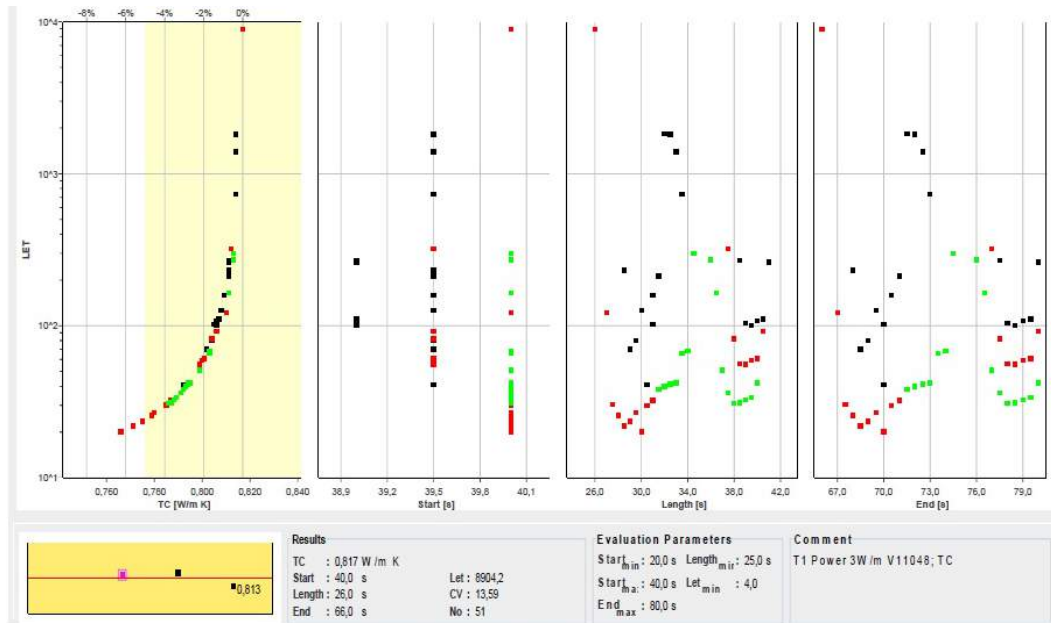
Sample ID	TC [W/mK]	LET [-]	Start [s]	End [s]	Length [s]	Number of Solutions [-]	CV [-]
T5_104	1,04	612,2	40,0	75,5	35,5	162	11,48
T5_105	1,02	36,3	31,5	56,5	25,0	1	11,48
T5_107	1,06	5335,0	39,0	78,0	39,0	29	11,56
T5_108	1,06	579,7	38,5	69,0	30,5	35	11,56
T5_109	1,05	14648,5	32,5	59,0	26,5	157	11,64
T5_110	1,02	279,8	22,5	57,5	35,0	212	11,64
T601	1,70	3163,9	33,0	66,0	33,0	1779	12,89
T602	1,67	242,3	29,5	60,5	31,0	2014	13,05
T603	1,71	3853,1	23,0	51,5	28,5	1782	12,89
T604	1,71	1000,0	32,5	74,0	41,5	1735	12,89
T605	1,71	1096,1	35,5	69,0	33,5	1638	12,89
T606	1,72	1804,6	24,0	59,0	35,0	1763	12,81
T607	1,71	18351,5	26,0	52,5	26,5	1799	12,89
T608	1,71	1873,1	26,5	61,5	35,0	1671	12,89
T609	1,72	11976,8	36,5	69,0	32,5	1589	12,89
T610	1,69	2446,0	36,0	80,0	44,0	1688	12,89
T6_101	1,64	5052,0	23,0	58,5	35,5	1079	12,11
T6_102	1,65	227690,3	31,0	69,5	38,5	1139	12,11
T6_103	1,65	36550,2	21,5	67,5	46,0	1406	11,95
T6_104	1,66	39945,2	30,5	77,5	47,0	843	12,11
T6_105	1,64	1825,9	20,0	56,5	36,5	400	12,03
T6_106	1,66	1847,0	25,0	62,5	37,5	623	12,11
T6_107	1,67	4612,9	33,0	69,0	36,0	673	12,03
T6_108	1,71	492,9	32,0	76,5	44,5	629	12,11
T6_109	1,67	18553,5	29,0	62,0	33,0	865	12,03
T6_110	1,65	624,2	20,5	58,0	37,5	409	12,03
T701	0,79	447,7	35,5	73,0	37,5	285	15,55
T702	0,77	497,9	39,0	70,5	31,5	6	15,70
T703	0,76	1003,6	33,0	73,5	40,5	481	15,55

Sample ID	TC [W/mK]	LET [-]	Start [s]	End [s]	Length [s]	Number of Solutions [-]	CV [-]
T704	0,77	3599,3	23,0	75,5	52,5	869	17,03
T706	0,74	612,3	25,5	60,0	34,5	176	15,63
T7_101	0,75	197,1	24,5	52,0	27,5	293	12,66
T7_102	0,79	5431,7	34,0	77,5	43,5	1541	14,14
T7_103	0,83	391,0	39,0	74,0	35,0	39	12,73
T7_104	0,82	95,3	39,5	70,0	30,5	1	12,73
T7_105	0,87	203,7	38,5	74,5	36,0	118	12,81
T7_106	0,82	3783,5	39,0	76,0	37,0	121	12,73
T7_107	0,76	316,4	22,5	49,5	27,0	137	12,66
T7_109	0,82	233,0	34,0	59,0	25,0	2	12,73
T7_110	0,83	1951,6	29,5	63,5	34,0	650	13,05
T801	1,60	3987,5	29,0	76,5	47,5	468	10,00
T802	1,65	389,9	31,0	79,5	48,5	579	10,08
T804	1,63	317,7	36,5	62,5	26,0	6	10,00
T805	1,65	370,3	39,0	69,5	30,5	33	10,00
T806	1,64	9802,0	29,5	56,6	27,0	70	10,08
T807	1,63	3504,0	29,5	58,5	29,0	36	10,00
T808	1,68	453,8	39,5	70,0	30,5	105	10,04
T809	1,60	22,1	30,5	56,0	25,5	2	10,04
T810	1,75	4140,3	35,5	60,5	25,0	500	10,16
T904	0,37	90,6	32,5	60,5	28,0	31	13,98
T905	0,38	610,3	40,0	66,0	26,0	1	14,06
T906	0,38	224,7	30,0	59,0	29,0	73	14,14
T907	0,38	390,0	31,0	57,0	26,0	15	13,98
T908	0,41	504,3	37,5	79,0	41,5	71	14,69
T909	0,38	4536,6	25,5	70,5	45,0	979	13,91
T910	0,36	1530,2	21,0	49,0	28,0	323	13,28
T9_102	0,43	184,4	40,0	66,0	26,0	25	14,41
T9_103	0,42	816,4	32,5	64,0	31,5	109	14,41

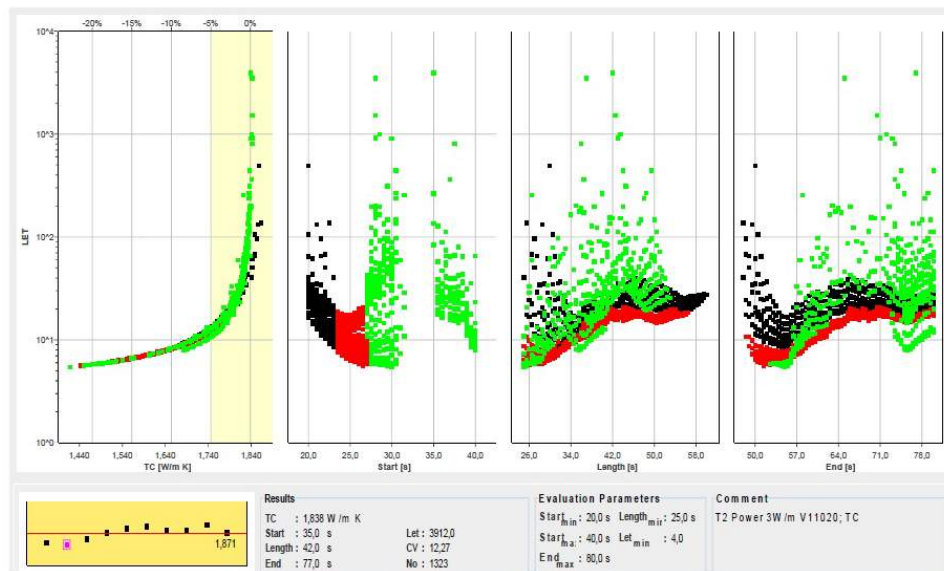
Sample ID	TC [W/mK]	LET [-]	Start [s]	End [s]	Length [s]	Number of Solutions [-]	CV [-]
T9_106	0,43	224,3	38,5	67,5	29,0	51	14,53
T9_107	0,43	72,0	40,0	72,0	32,0	72	14,45
T9_108	0,42	1697,1	34,0	65,0	31,0	55	14,45
T9_109	0,42	37,1	35,0	60,5	25,5	1	14,38
T9_110	0,42	843,1	25,0	76,5	51,5	449	15,23
T1001	1,49	335,7	34,0	60,5	26,5	52	10,00
T1002	1,46	1945,8	22,5	62,5	40,0	473	11,02
T1003	1,47	2719,4	30,0	76,5	46,5	677	10,94
T1004	1,46	7759,4	32,5	72,0	39,5	389	11,02
T1005	1,48	7008,8	32,0	71,5	39,5	319	10,86
T1006	1,48	649,5	30,0	73,0	43,0	670	10,86
T1007	1,44	4203,4	23,0	48,0	25,0	505	10,70
T1008	1,47	10278,2	25,5	60,0	345,0	294	10,55
T1009	1,47	4525,7	23,5	64,0	40,5	540	10,94
T1010	1,48	19713,8	31,5	69,0	37,5	379	10,39
T11_101	1,53	8192,7	24,0	57,0	33,0	1863	13,05
T11_102	1,57	8644,9	23,5	62,5	39,0	479	12,66
T11_103	1,58	4466,1	30,5	69,5	39,0	441	12,58
T11_104	1,56	2865,4	22,5	58,0	35,5	340	12,50
T11_105	1,59	1023,5	36,5	71,0	34,5	143	12,34
T11_106	1,57	1697,3	31,0	62,0	31,0	319	12,42
T11_107	1,57	907,7	39,5	75,5	36,0	431	12,34
T11_108	1,56	1185,5	26,0	58,0	32,0	256	12,42
T11_109	1,53	1907,7	26,0	56,0	30,0	302	12,34
T11_110	1,55	1596,8	26,5	58,5	32,0	563	12,27
T12_101	0,24	492,9	39,5	67,0	27,5	56	16,02
T12_105	0,26	149,1	36,5	61,5	25,0	12	16,29
T12_107	0,26	58,5	36,5	64,0	27,5	54	16,42
T12_108	0,26	1437,2	39,5	77,0	37,5	24	16,33

Sample ID	TC [W/mK]	LET [-]	Start [s]	End [s]	Length [s]	Number of Solutions [-]	CV [-]
T12_110	0,26	4026,3	34,5	60,5	26,0	35	16,33
T1304	0,37	105,1	40,0	70,5	30,5	9	16,09
T1305	0,37	11,7	35,5	62,5	27,0	17	16,09
T1306	0,38	636,5	39,0	66,0	27,0	26	16,17
T1401	1,73	2074,5	31,0	72,5	41,5	636	11,72
T1402	1,72	10469,6	36,5	79,5	43,0	1299	11,88
T1403	1,72	7761,6	27,5	64,0	36,5	851	11,80
T1404	1,73	6589,0	28,5	77,0	48,5	575	11,88
T1405	1,72	34542,8	20,0	63,0	43,0	898	11,80
T1406	1,71	4084,4	24,5	52,0	27,5	671	11,72
T1407	1,73	18753,4	32,0	63,0	31,0	710	11,72
T1408	1,73	186852,0	22,0	59,5	37,5	921	11,80
T1409	1,74	25863,5	32,0	79,0	47,0	717	11,72
T1410	1,73	9646,3	23,5	63,5	40,0	563	11,72

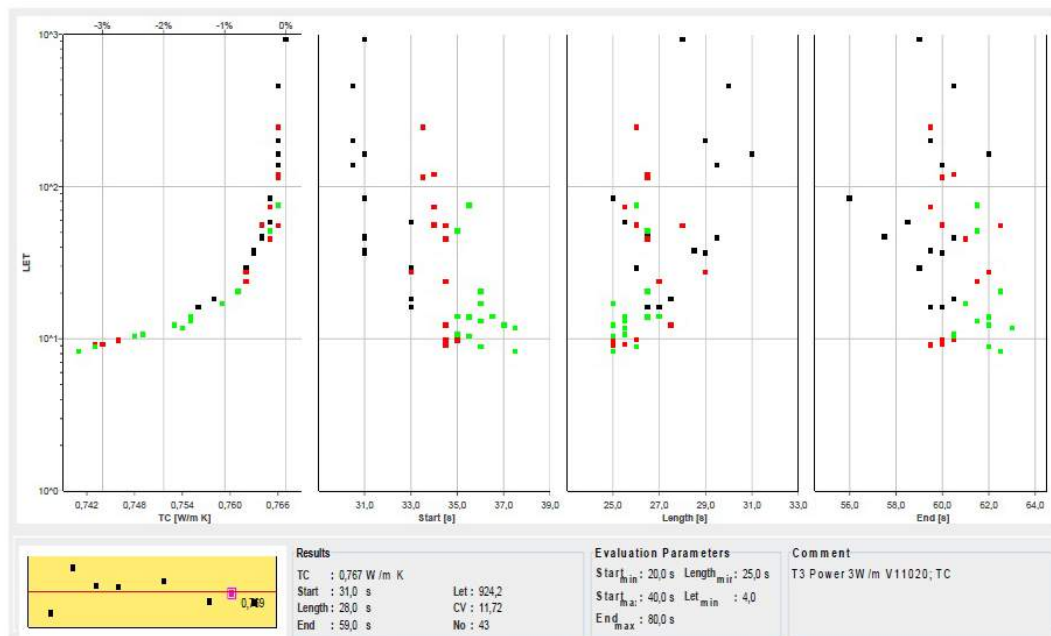
11.2. Data recordings of TC measurements



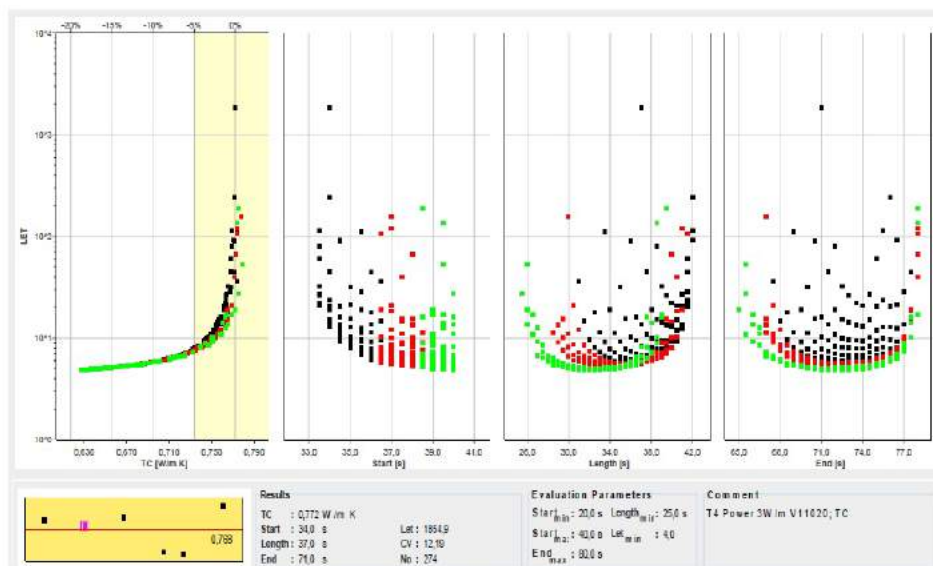
T1_T102



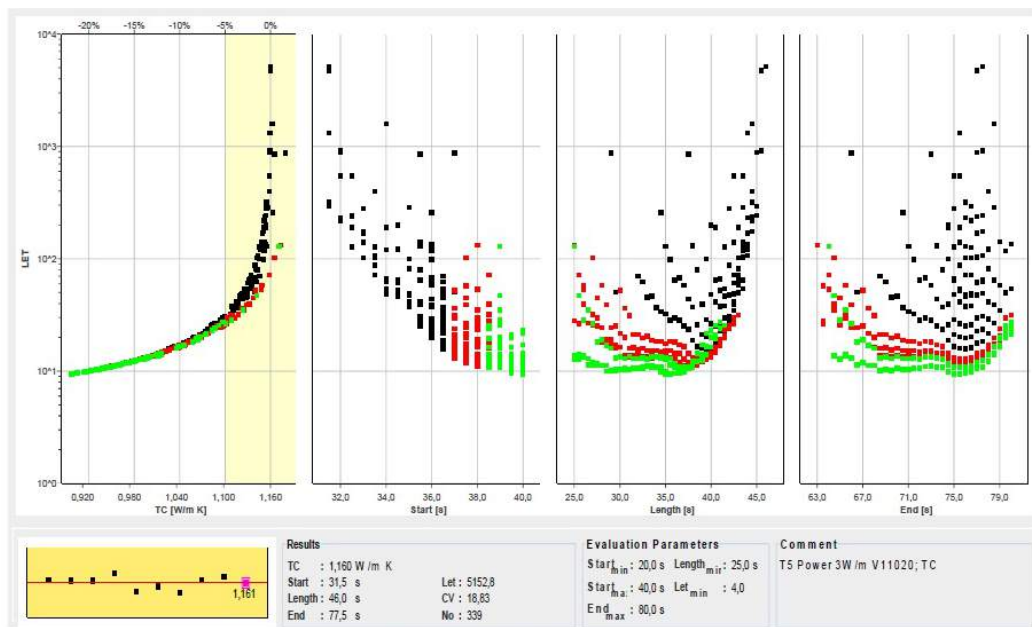
T2_T202



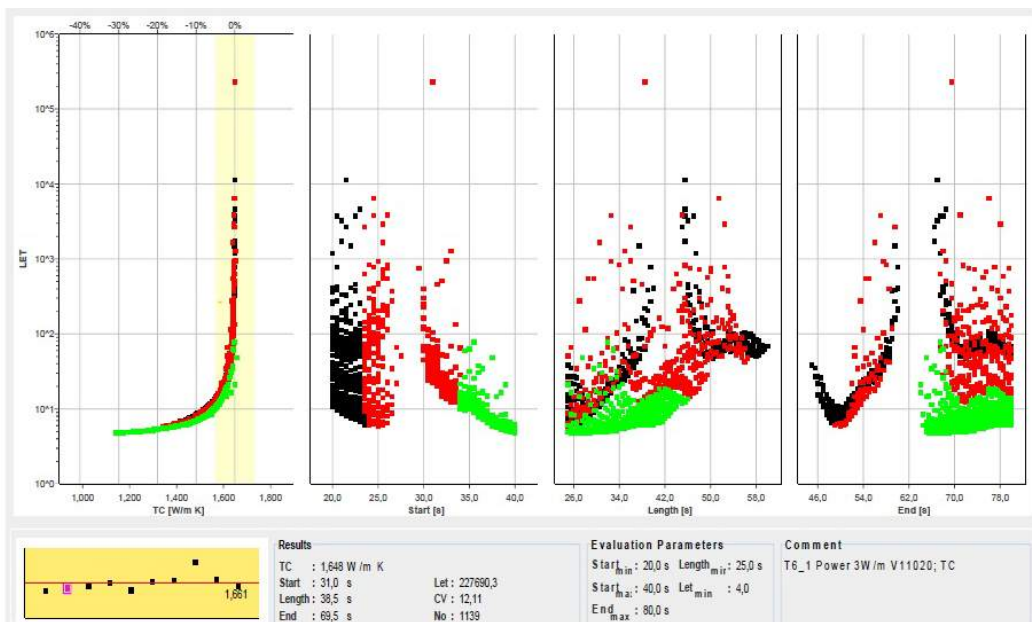
T3_T309



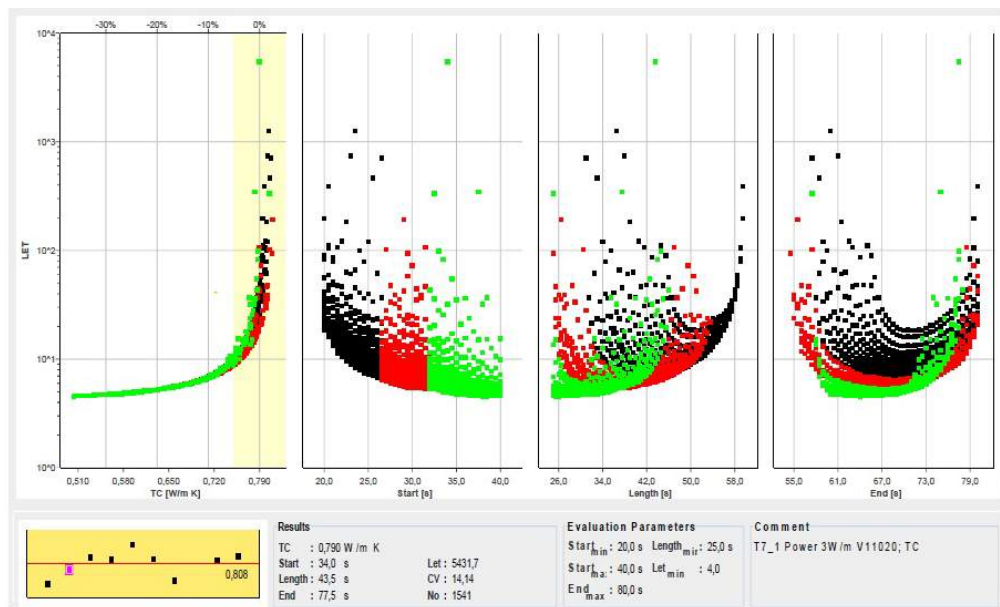
T4_T403



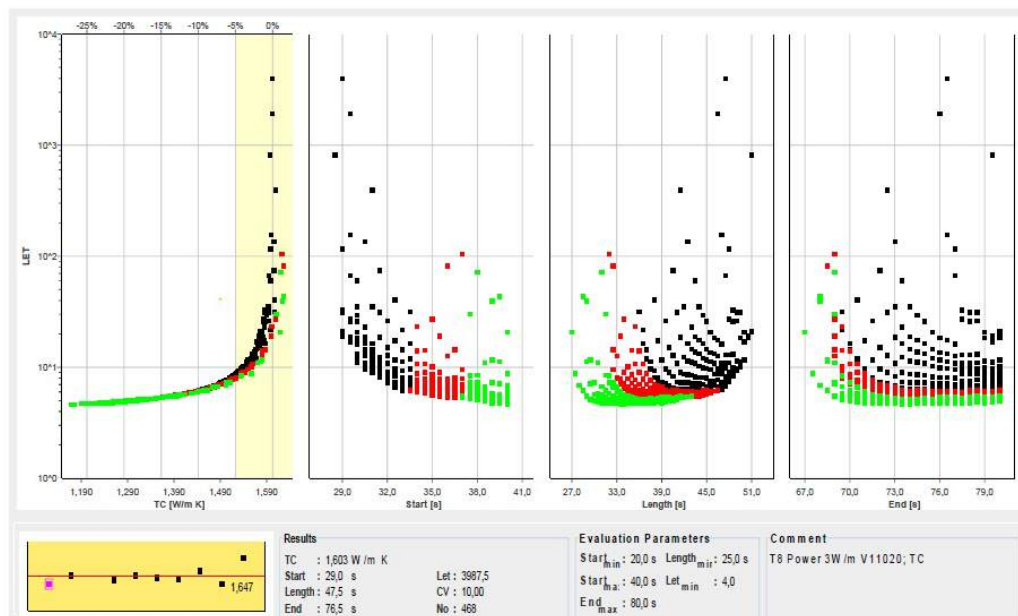
T5_T510



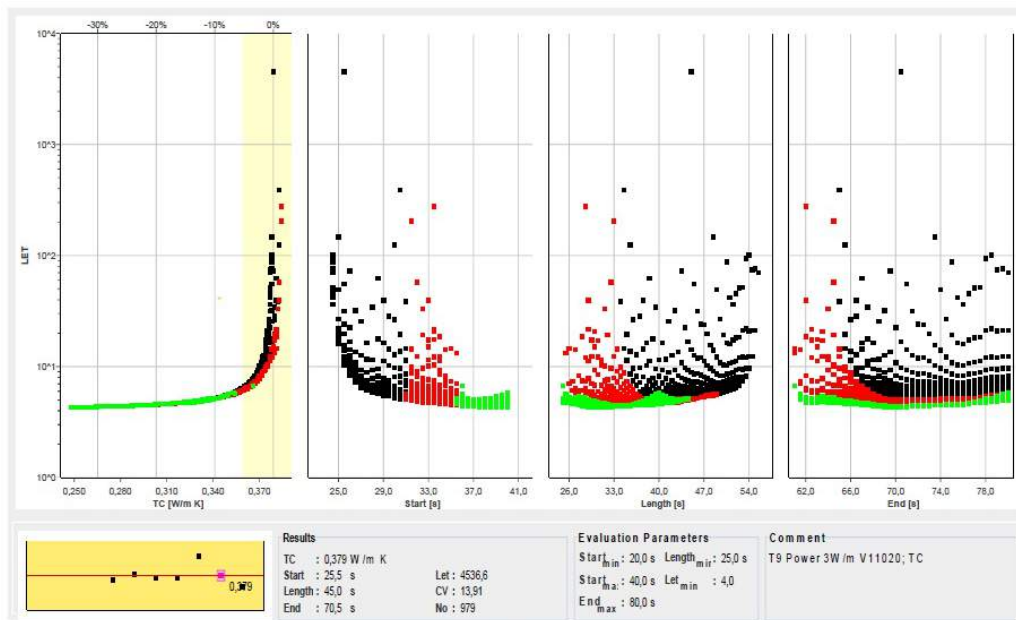
T6_102



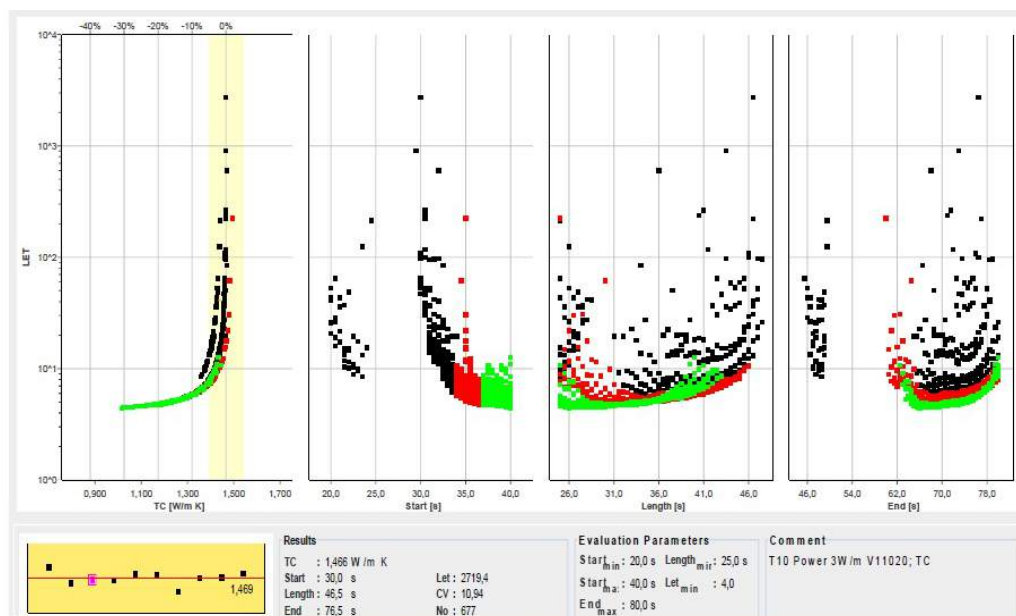
T7_I102



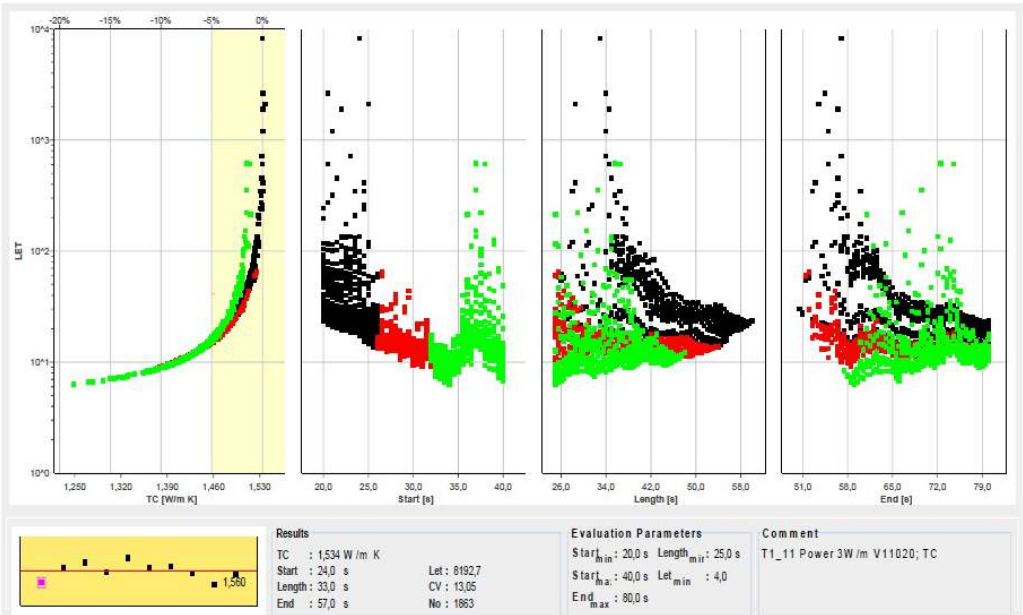
T8_I801



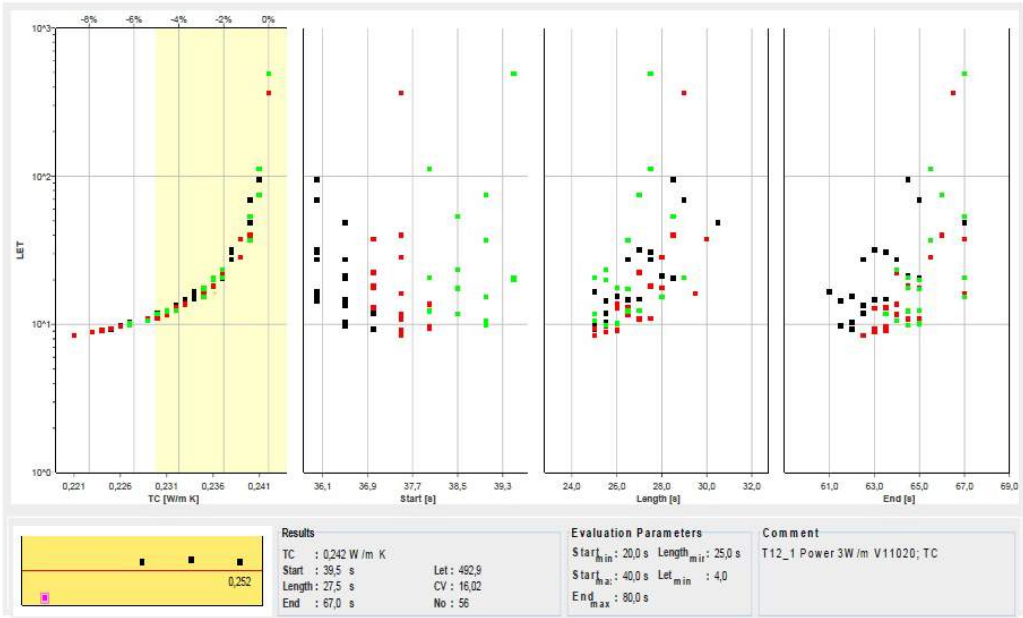
T9_T909



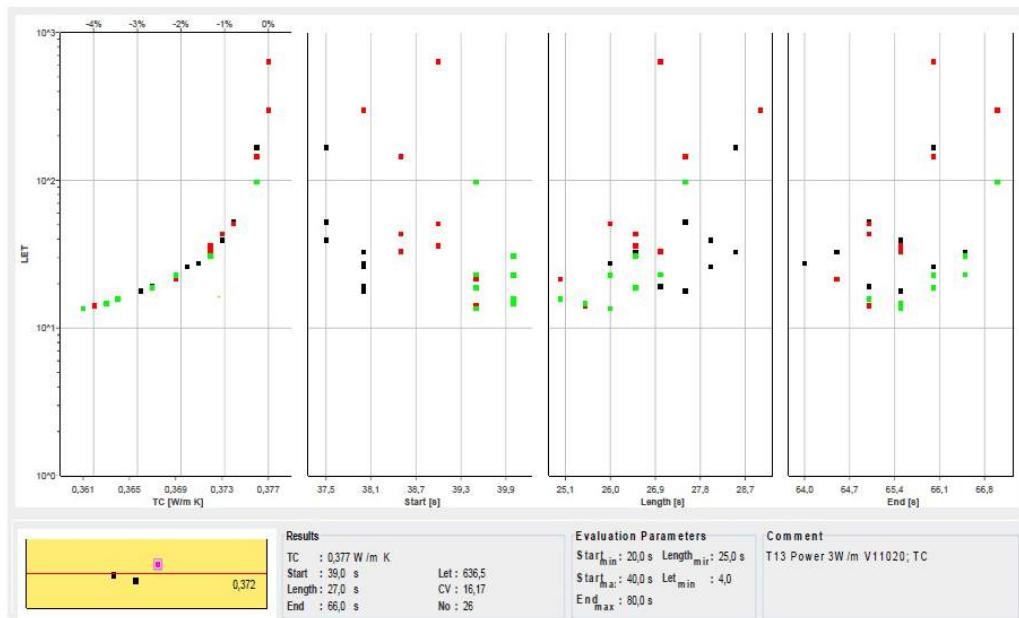
T10_T1003



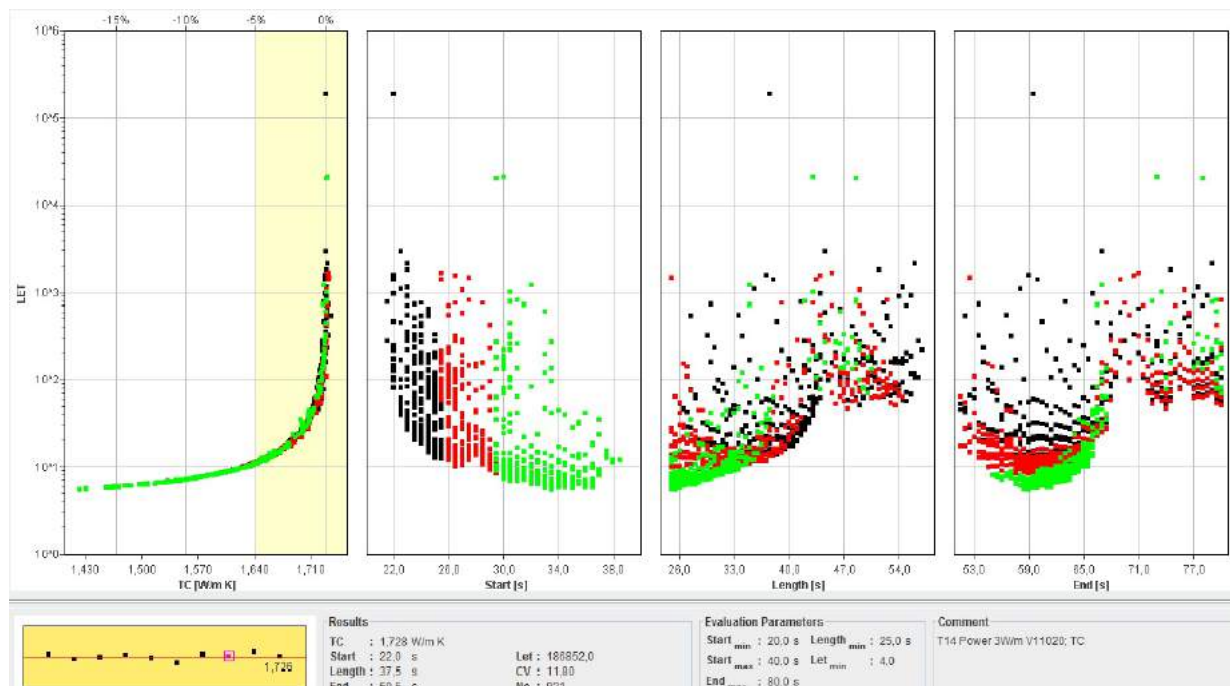
T11_T1_1101



T12_101



T13_1306



T14_1402

11.3. Detailed chemical composition of each fluid sample

Sample	Al (PPB)	As (PPB)	B (PPB)	Ba (PPB)	Br (PPB)	Ca (PPM)	Cd (PPB)	Cl (PPM)	Cr (PPB)	Cs (PPB)	Cu (PPB)	Fe (PPB)	Ga (PPB)	Ge (PPB)	Hg (PPB)	K (PPM)	Li (PPB)	Mg (PPM)	Mn (PPB)	Mo (PPB)	Na (PPM)	Ni (PPB)	P (PPB)	Pb (PPB)	Rb (PPB)	S (PPM)	Sb (PPB)	Sc (PPB)	Se (PPB)	Si (PPB)	Sn (PPB)	Sr (PPB)	Ti (PPB)	Tl (PPB)	V (PPB)	W (PPB)	Zn (PPB)
CHPM 3.1	44	157.7	677	469.67	23	57.39	2.07	3	7.3	70.94	35.4	69	0.22	4.48	65.9	27.28	503.3	3.80	137.78	65.1	17.11	2.5	24	1776.7	121.53	21	146.74	14	1.6	151463	0.15	548.75	25	5.04	1.8	33.27	320.3
CHPM 4.1	21	1.0	62	248.02	427	52.89	139.59	2	1.8	3.68	2.7	<10	<0.05	1.22	<0.1	2.94	8.4	4.29	577.20	0.6	1.53	42.3	<10	1314.2	9.27	36	19.45	<1	1.7	4576	<0.05	844.57	<10	152.06	<0.2	0.19	5894.7
CHPM 4.2	4	0.8	45	228.38	466	47.65	116.90	2	1.7	3.37	1.9	<10	<0.05	0.96	0.1	3.43	10.6	3.42	420.34	0.6	1.83	25.3	<10	1067.2	10.81	31	15.81	<1	1.6	4237	<0.05	660.15	<10	214.55	<0.2	0.07	5041.0
CHPM 4.4	12	9.5	27	219.73	155	21.24	78.93	<1	1.2	1.30	16.0	<10	<0.05	0.32	176.6	1.39	7.5	1.58	265.81	0.5	1.69	7.1	<10	17008.3	4.43	14	65.22	<1	0.6	1740	<0.05	489.79	<10	82.14	<0.2	0.05	5767.9
CHPM 5.1	4	15.6	289	107.44	126	477.12	<0.05	8	1.1	8.58	9.3	<10	<0.05	1.35	0.8	10.82	89.5	26.19	960.09	8.6	8.49	65.0	<10	1.5	80.92	364	91.66	3	1.1	51658	<0.05	414.46	<10	14.58	<0.2	0.23	27.1
CHPM 6.1	6	31.9	231	158.62	5	122.46	<0.05	<1	1.5	5.05	4.4	<10	0.69	3.08	3.5	2.31	6.7	0.30	13.48	50.6	2.37	1.4	<10	10.5	32.54	81	12.57	9	0.7	75451	<0.05	220.27	13	0.06	10.0	28.29	9.6
CHPM 12.1	76	24.0	7105	154.87	220	383.83	0.06	41	7.9	68.69	8.2	<10	<0.05	3.27	<0.1	8.18	309.3	126.02	285.76	3.8	18.80	2.8	<10	19.1	59.66	379	18.75	9	0.8	74144	<0.05	377.31	12	8.53	0.3	1.06	15.6
CHPM 14.2	33	260.0	1552	248.89	121	105.83	0.32	9	1.4	19.82	5.6	64	0.12	42.84	<0.1	17.48	82.6	9.28	257.33	24.2	27.62	6.1	<10	4.3	67.32	75	18.75	9	<0.5	138772	0.19	505.93	24	0.21	7.1	11.80	11.7
CHPM29.1	3741	142.8	411	147.37	24	0.25	<0.05	<1	1.5	13.89	2.9	165	11.38	2.19	0.1	40.33	80.2	0.11	8.70	15.0	28.99	1.6	175	12.6	135.66	27	13.03	2	3.1	112065	0.33	3.66	26	0.10	241.1	12.05	4.3
CHPM32.1	1893	268.2	287	178.20	23	0.52	0.09	<1	0.9	11.80	3.9	23	4.45	0.91	<0.1	21.86	38.4	0.08	17.39	16.4	18.68	0.7	147	100.9	79.95	14	112.50	1	2.6	83401	0.35	5.56	15	0.34	93.4	7.33	18.1
CHPM39.1	1184	17.4	171	28.60	23	4.00	<0.05	<1	6.4	21.55	0.3	<10	5.06	2.20	<0.1	101.52	59.5	0.54	5.65	9.4	34.62	0.6	<10	1.6	341.13	3	3.86	<1	<0.5	88195	0.05	19.80	16	0.49	0.8	17.28	1.4
CHPM40.1	4654	125.7	175	4.75	22	0.58	<0.05	<1	10.8	12.33	2.8	34	16.31	5.63	1.4	18.51	36.8	<0.05	0.52	11.2	158.02	2.3	62	25.1	75.40	12	16.41	<1	0.9	116360	1.47	2.70	20	<0.01	2.3	63.95	2.7
CHPM42.1	611	12.6	144	770.71	9	6.50	<0.05	<1	15.9	64.26	0.4	386	2.26	4.35	<0.1	152.49	139.1	2.94	36.12	7.8	122.47	1.0	46	3.0	557.89	3	4.49	<1	<0.5	121894	0.09	45.80	21	0.23	0.4	24.80	1.1
CHPM43.1	2110	46.3	185	761.83	22	3.04	0.12	<1	12.2	29.10	4.6	131	5.53	5.40	1.0	136.32	53.2	0.38	14.55	7.4	106.56	1.8	95	42.2	321.55	5	11.16	1	0.8	75933	0.90	28.73	15	0.01	0.2	15.70	10.1